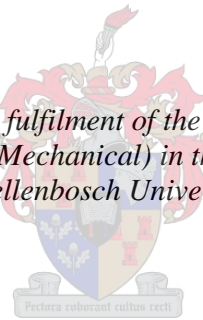


The performance of an axial flow fan in a small scale A-frame test facility

by
Raoul Dimitri Böck

*Thesis presented in partial fulfilment of the requirements for the degree
of Master of Engineering (Mechanical) in the Faculty of Engineering at
Stellenbosch University*



Supervisor: Prof Sybrand J. van der Spuy
Co-supervisor: Dr Danie N.J. Els

December 2017

DECLARATION

By submitting this thesis electronically, I declare that the entirety of the work contained therein is my own, original work, that I am the sole author thereof (save to the extent explicitly otherwise stated), that reproduction and publication thereof by Stellenbosch University will not infringe any third-party rights and that I have not previously in its entirety or in part submitted it for obtaining any qualification.

Date: December 2017

Copyright © 2017 Stellenbosch University

All rights reserved

ABSTRACT

The performance of an axial flow fan in a small scale A-frame test facility

This thesis investigated the performance of the B2 axial flow fan at different operating points and at two fan speeds in an A-frame configuration. For this purpose, a test facility consisting of a forced draft fan configuration discharging into an A-frame plenum chamber (referred to as a modular, scaled air-cooled condenser or MSACC) was designed and manufactured. Using the fan performance curves and experimental results for the heat exchanger model, the operating range of the test facility was determined to be within the peak efficiency range of the B2-fan as tested in the BS 848 test facility. The results from the experiments show that there is correlation between the static pressure, power consumption and static efficiency of the B2-fan in the MSACC and BS848 test facilities.

The inlet velocity and outlet velocities were measured using anemometers. With calibration data obtained using a built forced draft wind tunnel, the outlet volumetric flow rate and static pressure distribution across the MSACC's A-frame. The results also show that there is a maldistribution in the air exit velocity due to the presence of the fan's outlet swirl. The MSACC provides a unique test bench for testing the performance of future air-cooled condenser and axial flow fan designs. Furthermore, it also provides a platform to study installation and environmental factors that influence the aerodynamic and structural performance of an air-cooled condenser fan.

UITTREKSEL

Die werkverrigting van 'n aksiale vloeï waaier in 'n klein-skaal A-raam toetsfasiliteit

Hierdie navorsing, ondersoek die werkverrigting van die B2 aksiale vloeï waaier by verskillende bedryfspunte en twee waaier spoed punte in 'n A-raam opstelling. Vir hierdie doel is 'n toets fasiliteit ontwerp en vervaardig bestaande uit 'n geforseerde deurvloeï waaier opstelling in 'n A-raam konfigurasie (ook genoem 'n modulêr, afgeskaalde lugverkoelde kondensor of MSACC). Deur gebruik te maak van die waaier se werksverrigting krommes en eksperimentele resultate vir die hitteruiler model, is die bedryfsomvang van die toetsfasiliteit bepaal om te werk in beperking van die maksimum benuttingsgraad van die B2-waaier, soos getoets in die BS 848 tipe-A toetsfasiliteit. Die resultate van die eksperimente toon aan dat daar 'n korrelasie is tussen die statiese druk, kragverbruik en benuttingsgraad van die B-waaier in die MSACC, in vergelyking met die waaierkrommes verkry vanaf 'n standaard BS 848 tipe-A waaier toetsfasiliteit.

Die inlaat en uitlaat snelhede was gemeet met behulp van anemometers. Die kalibrasie data was verkry met behulp van 'n geboude druk wind tunnel, om die uitlaat volumetriese stroomsnelheid en statiese druk verspreiding oor die MSACC se A-raam te meet. Die resultate toon ook dat daar 'n wanverdeling is in die snelheid van die lug wat uitgaan, te wyte aan die teenwoordigheid van die waaier se rotasionele uitlaat snelheidskomponent. Die MSACC bied 'n unieke fasiliteit vir die toets van werksverrigtinge van aksiale vloeï waaïers en toekomstige lugverkoelde kondensor ontwerpe. Verder bied dit ook 'n platform om omgewingsfaktore wat 'n invloed het op die aërodinamiese en strukturele werkverrigtinge van 'n lugverkoelde kondensor waaier te bepaal.

ACKNOWLEDGEMENTS

I would like to thank the Lord Jesus Christ, for giving me the will, courage and wisdom to endure. Without Him this project would not have been a success. This thesis has helped to build my character, and I dedicate this thesis to Him alone.

I would also like to thank the following people for their guidance, prayers, assistance and support during the two years:

1. My father, mother and brother
2. Prof S.J. van der Spuy and Dr D.N.J. Els
3. My friends
4. The personnel at the Mechanical and Mechatronic Engineering workshop

TABLE OF CONTENTS

List of Figures	ix
List of Tables	xii
Nomenclature	xiv
Abbreviations	xvi
1. Introduction	1
1.1. Overview	1
1.2. Background	2
1.3. Problem Statement	3
1.4. Scope and Limitations of the Study	3
1.5. Objectives of the Study	4
1.6. Methodology	4
1.7. Significance of this Study and its Implications	4
1.8. Thesis Overview	5
2. Literature review	6
2.1. Introduction	6
2.2. Turbomachines	6
2.2.1. Application of axial flow fans	6
2.2.2. Ventilation system and fan selection	6
2.2.3. Fan specifications	8
2.3. Power Plants	9
2.4. The Air-cooled Condenser	11
2.4.1. Types of forced draft air-cooled condensers	12
2.4.2. ACC performance	13
2.5. Standardisation of Fan Performance Testing	15
2.5.1. Fan performance testing	15
2.5.2. The types of BS 848 standard test arrangements	16
2.5.3. Limitations of ISO 5801 / BS 848 part 1 standard	16
2.6. Performance measurement of ACCs	18
3. Theoretical analysis	19
3.1. Introduction	19
3.2. Air-cooled condenser draft equation	20
3.2.1. Upstream and Downstream Obstacles Affecting the Fan	21
3.2.2. Mean flow incidence angle	21
3.2.3. Inlet pressure loss coefficient	21
3.2.4. Jetting loss coefficients	22
3.2.5. Outlet loss coefficients	23
3.2.6. Heat exchanger pressure loss coefficient	24
3.3. MSACC Theoretical analysis	25
3.3.1. Perforated Plates and Guide Fins	25
3.3.2. Safety Screen	26
4. Design of small scale air-cooled condenser test bench	27
4.1. Introduction	27
4.2. Design Limitations and Requirements	28
4.3. The Design Concepts Considered	29

4.3.1.	Scaled unit	29
4.3.2.	ACC plenum design	29
4.3.3.	Inlet bell mouth	29
4.3.4.	Arrangement of the electric motor	29
4.4.	Technical Review of the MSACC Design	30
4.4.1.	Support structure, platform and A-frame structure floor.....	31
4.4.2.	The bell mouth	31
4.4.3.	Electric motor and stand.....	32
4.4.4.	Fan bearing housing and fan bridge	32
4.4.5.	A-frame plenum	33
4.4.6.	Perforated plate and guide fins.....	34
4.4.7.	Anemometer cross beam bracket	35
4.5.	Manufacturing, Construction and Assembly	35
4.5.1.	Support structure	35
4.5.2.	Bell mouth.....	36
4.5.3.	MSACC A-frame	36
4.5.4.	Plenum sealing	36
4.5.5.	Fan bearing housing	36
4.5.6.	Electric motor stand	37
4.5.7.	Variable speed drive and safety screen	37
4.5.8.	MSACC B2 axial flow fan installation	38
5.	Instrumentation Calibration, MSACC Test setup and MSACC testing procedure	39
5.1.	Introduction	39
5.2.	Measurement Equipment.....	39
5.2.1.	Torque transducer.....	40
5.2.2.	Propeller anemometer calibration	42
5.2.3.	Laser Tachometer, barometer and thermometer.....	45
5.2.4.	Pressure transducers	46
5.2.5.	MSACC AutoTran pressure transducer calibration	47
5.3.	MSACC Test Setup	48
5.3.1.	Data logging equipment	49
5.3.2.	Instrumentation installation.....	50
5.4.	Pre-tests	51
5.4.1.	Determining of the porosity of the perforated plate	51
5.4.2.	Perforated plate porosity test.....	52
5.4.3.	The Anemometer Distance Test.....	55
5.5.	MSACC Test Procedures.....	56
6.	Data Processing, Analysis and Results	58
6.1.	Introduction	58
6.2.	Data Processing	58
6.2.1.	Data averaging and deviation.....	58
6.2.2.	Instrument signal frequency analysis	59
6.3.	Data Calculations.....	60
6.4.	MSACC Operating Point.....	62
6.4.1.	Inlet velocity distribution and anemometer tests.....	63
6.4.2.	Inlet velocity comparison	66
6.4.3.	Outlet velocity distribution.....	67
6.4.4.	Outlet velocity comparison	70

6.4.5.	The effect of adjacent perforated plates	71
6.5.	Volumetric flow rate comparison	72
6.6.	Outlet pressure distribution.....	73
6.7.	MSACC B2-Fan Performance Comparison	74
6.7.1.	Static pressure versus volumetric flow rate.....	74
6.7.2.	Fan power consumption versus volumetric flow rate.....	75
6.7.3.	Fan static efficiency versus volumetric flow rate.....	75
6.8.	Performance measurement.....	76
6.9.	Conclusion	77
7.	Conclusion and Recommendations	78
7.1.	Introduction	78
7.2.	Motivation for the Study.....	78
7.3.	Research Findings.....	78
7.4.	Future Developments.....	79
7.4.1.	Aerodynamics.....	79
7.4.2.	Structural mechanics	79
7.5.	Future MSACC design improvements.....	80
7.5.1.	MSACC electric motor stand	80
7.5.2.	Hub design.....	80
7.5.3.	Setup time reduction.....	80
7.6.	Conclusion	80
8.	References	81
Appendix A: The dimensions of the MSACC		A.1
A.1	Laboratory Layout	A.4
A.2	General Dimensions of MSACC.....	A.4
A.3	B2-fan Axial Flow Fan Specification and Performance	A.5
Appendix B: MSACC Draft equation Calculations.....		B.1
B.1	Air-cooled heat exchanger draft equation	B.1
B.2	MSACC draft equation	B.2
B.3	MSACC parameters	B.3
B.3.1.	The thermo-physical properties of air:	B.3
B.3.2.	Upstream obstacles.....	B.3
B.3.3.	MSACC B2-fan dimensions.....	B.3
B.3.4.	Downstream obstacles.....	B.3
B.4	Determining the MSACC operating conditions	B.4
B.4.1.	heat exchanger supports pressure loss coefficient.....	B.4
B.4.2.	Up- and down-stream pressure loss coefficient.....	B.4
B.4.3.	Contraction loss coefficient.....	B.5
B.4.4.	Outlet loss coefficient.....	B.5
B.4.5.	Heat exchanger pressure loss coefficient	B.5
B.5	MSACC Duty Point Sample Calculations	B.6
Appendix C: Induced draft wind tunnel layout, experiment description and conducted test results		C.1
C.1	Induced wind Tunnel Setup and calculation	C.1
C.2	Air Properties calculations	C.3
C.3	Induced wind tunnel pressure transducers calibration	C.4
C.4	Induced wind tunnel leakage test	C.6

C.5 Perforated plate porosity test.....	C.7
C.6 Induced wind tunnel distance Anemometer calibration.....	C.11
C.7 Forced wind tunnel distance Anemometer calibration.....	C.13
C.8 Chosen Perforated Plate Throttle Test Results.....	C.17
Appendix D: MSACC Test data	D.1
D.1 Inlet velocity distribution	D.1
D.2 Outlet velocity distribution	D.3
D.3 A-frame outlet pressure distribution 660 rpm.....	D.7
D.4 A-frame outlet pressure distribution 750 rpm.....	D.9
D.1 MSACC B2-fan Performance Sample Calculations	D.10

LIST OF FIGURES

Figure 2-1: Characteristic fan curve, system resistance curve and duty point	7
Figure 2-2: Simple ideal Rankine cycle with TS diagram (Cengel & Boles, 2011)	10
Figure 2-3: Types of condensers: (A) Dry natural-draft cooling tower; (B) Dry forced-draft cooling tower; (Powermag, 2016) (C) Wet natural-draft cooling tower; (D) Wet forced-draft cooling tower. (Hamon Group, 2016)	11
Figure 2-4: A-frame (forced draft) and V-frame (induced draft) air cooled condensers.....	11
Figure 2-5: Standard fan installation types (Dwyer, 2012)	16
Figure 3-1: Forced air-cooled condenser	20
Figure 3-2: Section of an array (Adapted from van Aarde & Kröger, 1993)	22
Figure 3-3: General picture of the flow through inclined finned tube bundles (Adapted from van Aarde & Kröger, 1993)	24
Figure 3-4: Safety screen dimension (Kröger, 1998)	26
Figure 4-1: MSACC section view with major component scheme	27
Figure 4-2: MSACC assembled with instruments	27
Figure 4-3: MSACC assembled 3D rendering.....	30
Figure 4-4: MSACC Structure (Left) with floor, walkway grid and railing (Right)	31
Figure 4-5: Electric motor stand 3D model	32
Figure 4-6: Fan bearing housing 3D model at the two positions (without the chain drive).....	33
Figure 4-7: ACC plenum design with perforated plates isometric 3D drawing	34
Figure 4-8: Heat exchanger box housing steel boxes, perforated plate and guide fins sub-assembly isometric drawing.....	35
Figure 4-9: Varispeed 15 kW variable speed drive (left) and the safety screen (right)	37
Figure 4-10: Blade setting angle procedure (left) and B2-fan in the installed position without the hub cover (right)	38
Figure 4-11: MSACC B2-fan in installed position and dimensions.....	38
Figure 5-1: HBM T22-200 torque transducer	40
Figure 5-2: Torque transducer calibration setup.....	41
Figure 5-3: Data and trend line for the torque transducer.....	42
Figure 5-4: Young model 27106T propeller anemometer (Left) and Anemometer calibration with pitot tube test setup in induced wind tunnel (Right).....	43
Figure 5-5: Laser tachometer (left), mercury barometer (middle) and wet- and dry- bulb mercury thermometer (right)	46
Figure 5-6: HBM PD1 (left) and one AutoTran pressure transducer (right)	46
Figure 5-7: Pressure transducer calibration setup.....	47
Figure 5-8: AutoTran Pressure Calibration Curve.....	48
Figure 5-9: The instrument setup for the MSACC	49
Figure 5-10: HBM MX1601B universal amplifier (Hottinger Baldwin Messtechnik, 2016) (Left) and data logging equipment measuring box	50

Figure 5-11: Safety screens (painted yellow) with bell mouth anemometers (Left) and cross beam member with four anemometers mounted across the A-frame's perforated plates(Right).....	51
Figure 5-12: MSACC operation point - Pressure loss prediction ($K_{he} = 22.2882$ and $K_{\theta t} = 35.2920$)	52
Figure 5-13: Perforated test plate with varying holes 73, 57 ,41 ,25 ,17 ,13 (From left to right and top to bottom).....	53
Figure 5-14: Static pressure vs volumetric flow rate for perforated test plates with different porosities.	54
Figure 5-15: Chosen perforated plate throttle test results.....	55
Figure 5-16: MSACC operating point prediction and comparison with aimed heat exchanger	55
Figure 5-17: Four main perforated plate throttle positions (100% open top left, 83.3% open right top, 66.6% left bottom and 50% bottom right)	56
Figure 6-1: Frequency amplitude spectrum of sample data for a 750 rpm data point	60
Figure 6-2: Empirical model for the influence of tip clearance (Wilkinson & van der Spuy, 2015).....	62
Figure 6-3: (750 rpm test) Anemometer placement in bell mouth and influencing components	63
Figure 6-4: (750 rpm) Inlet air speed variation six-anemometer test results.....	64
Figure 6-5: (750 and 660 rpm test) Anemometer placement for in bell mouth and influencing component	65
Figure 6-6: (750 rpm) Inlet air speed variation six-anemometer test	65
Figure 6-7: (660 rpm) six-anemometer test results inlet air speed variation	66
Figure 6-8: Anemometer measuring	68
Figure 6-9: (750 rpm) Outlet air speed variation with throttling (Left side)	68
Figure 6-10: (660 rpm) Outlet air speed variation with throttling (Left side)	69
Figure 6-11: (750 rpm) Anemometer-positioned-averaged outlet air speed variation with throttling (Right side)	69
Figure 6-12: (660 rpm) Anemometer-positioned-averaged outlet air speed variation with throttling (Right side)	70
Figure 6-13: Comparison of the BS 848 and MSACC test facilities of B2-fan static pressure vs volumetric flow rate curve performance	74
Figure 6-14: Comparison of the BS 848 and MSACC test facilities of B2-fan power vs volumetric flow rate curve performance	75
Figure 6-15: Comparison of the BS 848 and MSACC test facilities of B2-fan static efficiency vs volumetric flow rate curve performance (750 rpm).....	75
Figure 6-16: Comparison of the BS 848 and MSACC test facilities of B2-fan static efficiency vs volumetric flow rate curve performance (660 rpm).....	76
Figure 6-17: Predicted and measured results comparison	76
Figure A-1: Laboratory layout before MSACC construction	A.4
Figure A-2: CAD drawing layout front and left view of MSACC design.....	A.5
Figure A-3: B2-axial flow fan BS-848 test results static pressure vs flow rate at 31degrees (Wilkinson & van der Spuy, 2015).....	A.6

Figure A-4: B2-axial flow fan BS-848 test results power vs flow rate at 31degrees (Wilkinson & van der Spuy, 2015).....	A.6
Figure A-5: B2-axial flow fan BS-848 test results static efficiency vs flow rate at 31degrees (Wilkinson & van der Spuy, 2015).....	A.7
Figure B-1: Forced draft air-cooled heat exchanger (Kröger, 1998).....	B.1
Figure B-2: MSACC control volume points (Adapted from Kröger, 1998)	B.2
Figure B-3: Upstream and downstream obstacles loss coefficient (Kröger, 1998)	B.4
Figure B-4: MSACC predicted results for 7 throttle positions.....	B.6
Figure C-1: Atmospheric open loop induced wind tunnel.....	C.1
Figure C-2: Test wind tunnel layout (Kröger, 1998).....	C.1
Figure C-3: Calibration curve for induced wind tunnel pressure transducers	C.5
Figure C-4: Leakage test.....	C.7
Figure C-5: Induced wind tunnel - distance Anemometer calibration test setup	C.11
Figure C-6: Open throttle position distance anemometer measurement for induced wind tunnel	C.13
Figure C-7: Forced wind tunnel.....	C.13
Figure C-8: Forced wind tunnel distance Anemometer calibration setup	C.14
Figure C-9: Open throttle position distance anemometer measurement for forced wind tunnel	C.15
Figure C-10: Throttle position - anemometer velocity voltage vs static pressure	C.15
Figure C-11: Throttle position - anemometer velocity vs static pressure.....	C.16

LIST OF TABLES

Table 5-1: Typical calibration test 1 values for HBM T22 200 torque transducer	41
Table 5-2: Anemometer typical voltage readings for test.....	43
Table 5-3: Wind tunnel typical test result of the anemometer calibration.....	44
Table 5-4: Voltage vs air speed readings of the anemometer calibration.....	45
Table 5-5: Pressure transducer calibration reading (Calibration test 1)	47
Table 5-6: AutoTran pressure transducer calibration constants	48
Table 5-7: Example 8.1.3 parameters	52
Table 5-8: Perforated test plate with varying holes' porosity and calculated pressure loss coefficient.....	53
Table 5-9: Chosen perforated plate throttle - pressure loss coefficient results.....	54
Table 6-1: (4 and 6 anemometer) Inlet volumetric flow rate comparison	67
Table 6-2: Typical outlet anemometer velocity readings for 750 rpm at 100% throttle.....	71
Table 6-3: Typical outlet anemometer velocity readings for 660 rpm at 100% throttle.....	71
Table 6-4: Throttle exit anemometer influence test.....	72
Table 6-5: Inlet and outlet volumetric flow rate comparison 750 rpm.....	72
Table 6-6: Inlet and outlet volumetric flow rate comparison 660 rpm.....	73
Table 6-7: A-frame static pressure distribution at 100% throttle (750 rpm)	73
Table A-1: B2-fan specifications as tested in BS 848 test facility (Wilkinson & van der Spuy, 2015)	A.5
Table B-1: Up- and down-stream pressure loss coefficients	B.5
Table B-2: Outlet pressure loss coefficient.....	B.5
Table B-3: Total heat exchanger pressure loss coefficient	B.6
Table C-1: Pressure transducer calibration values.....	C.5
Table C-2: Pressure transducer calibration curve values.....	C.5
Table C-3: Leakage test results (test 2)	C.6
Table C-4: 9 holes (35 mm diameter) Induced wind tunnel test results	C.7
Table C-5: 13 holes (35 mm diameter) Induced wind tunnel test results	C.8
Table C-6: 17 holes (35 mm diameter) Induced wind tunnel test results	C.8
Table C-7: 25 holes (35 mm diameter) Induced wind tunnel test results	C.9
Table C-8: 33 holes (35 mm diameter) Induced wind tunnel test results	C.9
Table C-9: 41 holes (35 mm diameter) Induced wind tunnel test results	C.9
Table C-10: 49 holes (35 mm diameter) Induced wind tunnel test results	C.10
Table C-11: 57 holes (35 mm diameter) Induced wind tunnel test results	C.10
Table C-12: 65 holes (35 mm diameter) Induced wind tunnel test results	C.10
Table C-13: 73holes (35 mm diameter) Induced wind tunnel test results	C.11
Table C-14: Induced wind tunnel - Pressure data readings and calculated results (200 mm data point at open throttle position).....	C.12
Table C-15: Induced wind tunnel - Anemometer distance voltage readings (open throttle position).....	C.12
Table C-16: Outlet perforated plate anemometer velocity to volumetric flow rate trend-curve conversion constants.....	C.16

Table C-17: Outlet perforated plate anemometer velocity to static pressure trend-curve conversion constants	C.17
Table C-18: 100% throttle (Right) and 91.7% throttle (Left).....	C.17
Table C-19: 83.3% throttle (Right) and 75% throttle (Left).....	C.18
Table C-20: 66% throttle (Right) and 58.3% throttle (Left).....	C.18
Table C-21: 50% throttle	C.18
Table D-1: 660 rpm at 50% throttle.....	D.1
Table D-2: 750 rpm at 50% throttle.....	D.1
Table D-3: 660 rpm at 58.3% throttle.....	D.1
Table D-4: 660 rpm at 66% throttle.....	D.2
Table D-5: 750 rpm at 66% throttle.....	D.2
Table D-6: 660 rpm at 75% throttle.....	D.2
Table D-7: 660 rpm at 83.3% throttle.....	D.2
Table D-8: 750 rpm at 83.3% throttle.....	D.2
Table D-9: 660 rpm at 91.6% throttle.....	D.2
Table D-10: 750 rpm at 100% throttle.....	D.3
Table D-11: 660 rpm at 100% throttle.....	D.3
Table D-12: Typical Outlet velocity readings - 660 rpm at 50% throttle.....	D.3
Table D-13: Typical Outlet velocity readings - 750 rpm at 50% throttle.....	D.4
Table D-14: Typical Outlet velocity readings - 660 rpm at 58.3% throttle.....	D.4
Table D-15: Typical Outlet velocity readings - 660 rpm at 66% throttle.....	D.4
Table D-16: Typical Outlet velocity readings - 750 rpm at 66% throttle.....	D.4
Table D-17: Typical Outlet velocity readings - 660 rpm at 75% throttle.....	D.5
Table D-18: Typical Outlet velocity readings - 660 rpm at 83.3% throttle.....	D.5
Table D-19: Typical Outlet velocity readings - 750 rpm at 83.3% throttle.....	D.5
Table D-20: Typical Outlet velocity readings - 660 rpm at 91.6% throttle.....	D.5
Table D-21: Typical Outlet velocity readings - 660 rpm at 100% throttle.....	D.6
Table D-22: Typical Outlet velocity readings - 750 rpm at 100% throttle.....	D.6
Table D-23: Exit A-frame distribution of static pressure - typical readings (Throttle 50% - 75% -at 660 rpm)	D.7
Table D-24: Exit A-frame distribution of static pressure - typical readings (Throttle 83% - 100% -at 660 rpm)	D.8
Table D-25: Exit A-frame distribution of static pressure - typical readings (750 rpm).....	D.9
Table D-26: Experimental readings for 660 rpm.....	D.10
Table D-27: Experimental readings for 750 rpm.....	D.11
Table D-28: Normalised 660 rpm B2-fan results	D.11
Table D-29: Normalised 750 rpm B2-fan results	D.12

NOMENCLATURE

Symbol	Description	Units
A	Area	[m ²]
d	Diameter	[m]
g	Gravitational constant	[m ² /s]
h	Head loss	[m]
K	Loss coefficient	[-]
\dot{m}	Air mass flow rate	[kg/s]
n	Number of data points or sections	[-]
p	Pressure	[Pa]
P	Power	[W]
Q	Flow rate	[m ³ /s]
R	Radial distance from centre of the hub	[m]
v	Air speed	[m/s]
\dot{V}	Air volumetric flow rate	[m ³ /s]
V	Velocity	[m/s]
T	Torque	[Nm]
X_i	One data value in volts	[V]
\bar{X}	One data value in volts	[V]
x	Distance	[m]
z	Height	[m]
β	Porosity	[-]
η	Efficiency	[-]
μ	Viscosity of air	[N s/m ²]
ρ	Density of air	[kg/m ³]
σ	Area ratio	[-]

Subscripts

<i>a</i>	Air
<i>an</i>	anemometer
<i>app</i>	Apparent
<i>b</i>	Bell mouth
<i>c</i>	Contraction / Fan casing cross sectional
<i>do</i>	Downstream
<i>e</i>	Exit
<i>ex</i>	Expansion
<i>F</i>	Fan
<i>fr</i>	Frontal
<i>h</i>	Hub
<i>he</i>	Heat exchanger
<i>i</i>	Inlet
<i>j</i>	System component
<i>l</i>	loss
<i>m</i>	Mean

<i>o</i>	Outlet
<i>ob</i>	Obstacles
<i>ss</i>	Safety screen
<i>ts</i>	structural support
<i>r</i>	Reference
<i>s</i>	static
ST	Steam
<i>t</i>	Total
<i>up</i>	Upstream
<i>w</i>	walkway
θ	Semi-apex angle

ABBREVIATIONS

ACC	Air-cooled condenser
BS	British standard
FEM	Finite element analysis
HEB	Heat exchanger bundle
HVAC	Heating ventilation and air conditioning
ISO	International standards organisation
MSACC	Modular scaled air-cooled condenser

1. INTRODUCTION

1.1. Overview

Electricity is considered to be the catalyst for development and growth in a country as it drives economic development, social upliftment and the Gross National Product (GNP). According to Kraft & Kraft, (1978), Asafu-Adjaye (2000) and Bakirtas, et al. (2012), there is evidence of a direct link between the United States of America GNP and energy consumption. They stated that, “the experience of developed countries shows that the electricity sector played a crucial role in their economic development not only as a key input in their industrial development, but also as a key factor in improving the quality of life of their people”.

The development of a country’s electrical grid and power station output is required to improve the energy access for its population, which is sustained by economic and industrial growth. Power utility companies such as NamPower, Eskom, Botswana Power Corporation and Copperbelt Energy Corporation are at the centre of the expansion of electricity supply. The demand for electricity strains the power delivery of existing power plants; hence emphasis is being placed on improving the efficiency and understanding the functions of various aspects of such plants. According to Southern African Power Pool (SAPP), the installed capacity of Southern African in 2010 is about 52 GW, 72% of which is based on coal-fuelled power generation, 18% on hydro power generation, and the remainder on oil and nuclear power generation. The South African system is dominant in the SAPP, accounting for 80% of the capacity in the region (Miketa & Merven, 2013).

Most of South Africa’s power is generated from coal-fired plants situated in semi-arid regions close to the coal fields. In these regions, choosing the source of cooling for these power plants has become an important and progressively complex issue. This is the result of limited water and financial resources, and legislative restrictions concerning noise and environmental impact (Augustyn, 2013). In addition, these regulatory frameworks call for improved quality of power supply, efficient and effective operation of infrastructure and the capitalisation of existing resources. To achieve this goal, it is important to understand the functioning and operation of each individual component in a power station.

According to Putman and Jaresch (2002), globally there has been a growing and competing demand for water for both domestic and industrial use over the past 30 years. This resulted in an increased interest in the use of air as a cooling medium instead of water. The first applications used for the air-cooled condensing of exhaust steam from steam turbines were air-cooled heat exchangers or air-cooled condensers (ACCs). ACCs are designed for the utility industry and evolved into configurations that recognised special needs for condensing large volumes of low-

pressure vapour and the removal of non-condensables, such as oil, in cooling tower systems. ACCs made it possible to build a power plant in locations with scarce water resources, which is often the case when a power plant is constructed at its fuel source.

SPX Cooling Technologies Inc. (2015) cites the following reasons (apart from water scarcity) for the selection of dry cooling systems:

- Governmental environment policies limiting the temperature increase in rivers and at sea.
- Water-use regulations in the region set by community and government.
- Reduced maintenance and expected operational lifetime of the power plant.
- Fuel and land flexibility in the selection of the power plant.
- Construction lead time.

Although the targets for energy demand reduction do not specifically mention the energy efficiency of fans, the parasitic loads mentioned include auxiliary equipment such as heating, ventilation and air-conditioning (HVAC) systems and fans. As reported by ISO 13348, worldwide fan power usage is estimated to be twenty percent of all generated power (Blake, 2013). Thus, if the efficiency of fans could be improved, it might well contribute to production, economic growth and development of a country.

1.2. Background

Air-cooled condensers are used in power plants to discharge heat when converting the working fluid from low-pressure steam to condensed water. It functions by transferring energy from the saturated steam coming from the power plant turbines to a heat sink, which is air. Major constraints for not considering the use of water are factors related to its availability and economic implications related to the treatment, storage and disposal thereof. In the Southern African context, considering the scarcity of water, restrictive government regulations and environmental concerns limit the use of water. Therefore, ACCs are more commonly used.

The performance of the ACCs is influenced by the ambient air conditions. As stated by Le Roux (2010) the dissipation of heat in an ACC is dependent on the dry-bulb temperature, wind speed, direction of wind and other atmospheric conditions. These conditions may result in off-design operation of the ACC fan and the heat exchanger. As the cooling capacity is reduced, the power generation capacity of the power plant reduces (Thiart, 1991).

An interview was conducted with Langenhoven (2016), the head engineering supervisor at van Eck power station located in Namibia. He points out dynamic interaction between the steam turbines and ACCs. He pointed out that hot air

recirculation, crosswinds, ACC's heat exchanger fouling and high dry-bulb temperature increases the turbine back pressure and produces a reduction of the steam turbine power output and this leads to an underperforming cooling system and requires lower the power output setting of the power station. One major function of the ACC is to produce a vacuum from the condensation of steam. Thus, requires the ACC systems to be monitored in conjunction with the other subsystems of the PowerStation. Furthermore, the electrical motors that drive the fans in the ACC are also responsible for parasitic power consumption of the power station, which must also be controlled to increase the powers station's power output.

Bruneau (1994) developed a rotor-only ducted axial flow fan, called the B2-fan. The B2-fan was specifically designed for use in an ACC. Due to problems related to reverse flow in the hub area of existing fans and the effect of distorted inlet airflow on fan performance, an issue highlighted by Venter (1990), a free vortex design was chosen for the B2-fan. The B2-fan was tested in the BS 848 test facility by Bruneau (1994) and subsequently Wilkinson and Van der Spuy (2015). The same B2-fan was used in this research.

This research is a study of the performance of an axial flow fan in the newly constructed A-frame forced draft modular scaled air-cooled condenser (MSACC) facility at the University of Stellenbosch. The fan's performance curves are obtained from an existing British Standard (BS) 848 Type-A fan tests facility. The design and construction of the MSACC forms an important component of this research. The MSACC is used to validate the assumptions made when specifying the operating point of the axial flow fan and the effect of the system on the fan.

1.3. Problem Statement

The performance results obtained from a standard fan test facility (like the existing BS 848 Type-A test facility at Stellenbosch University) are often not sufficient to predict the performance of an installed forced draft ACC fan. Hence the need to design and construct a modular scaled A-frame forced draft air-cooled condenser (MSACC) facility in order to test the installed performance of the B2 axial flow fan at different operating points.

1.4. Scope and Limitations of the Study

The focus of the study was limited to the construction of a MSACC facility at Stellenbosch University and testing the performance of the B2-fan installed in the MSACC. This study investigated the installed fan's performance at different duty points in terms of airflow rate, pressure, and static efficiency. To control the operating point of the fan, perforated plates with guide fins were installed in the MSACC facility. The results were compared to the predicted operating data for the same fan, based on performance curves obtained from the BS 848 Type-A test facility. Further design limitations are stated in Chapter 4.

1.5. Objectives of the Study

The primary objective of this study was to compare the performance of the B2-fan, installed in the MSACC, to the performance predicted for the same fan, based on the fan curves obtained from the BS 848 Type-A fan test facility. To achieve this, the following secondary objectives were set:

1. Design, manufacture and construct the MSACC facility.
2. Perform theoretical calculations and wind tunnel tests to confirm the pressure loss characteristics of the guide fins and perforated plates.
3. Install the existing B2 axial flow fan and measuring instrumentation in the MSACC.
4. Calibrate anemometers with perforated plate outlet flow rate and pressure.
5. Measure the static pressure, inlet and outlet air speed, torque and shaft speed in the MSACC and interpret data.
6. Compare the results obtained from the MSACC facility to the fan performance curves obtained from the BS-848 Type-A test facility.

1.6. Methodology

Both quantitative and qualitative methods were considered for carrying out this investigation. The qualitative component of the investigation required a literature review, interviews with experts in the industry and the interpretation of findings. The quantitative part of the investigation considered data that was collected from the two test facilities, which was compared and interpreted for deviations, trends and similarities (Leedy, 2005).

Preliminary and calibration tests were run to ascertain compatibility, reliability and validity and to identify the limitations of the measurements being recorded. In addition to recording the measurements to characterise the performance of the axial flow fan, the captured data was processed and analysed for comparison with theoretical calculations. The primary goal of analysing the data was to compare the results for similarities, differences, correlations and trends observed between the two test facilities.

1.7. Significance of this Study and its Implications

It is expected that this research will have a significant impact on how ACC fans are used in future. It will investigate the effect of the entire ventilation system on the performance of an axial flow fan. In addition, this research will also contribute towards the debate on whether standard testing protocols are sufficient for predicting installed ACC fan performance (Meyer, 2000); (Cory, 2012); (Putman & Jaresch, 2002). The design and construction of the facility also allows for the testing of other types of fans.

In addition, this study will facilitate further research and development in the field of axial flow fans and their performance in ACCs. The facility can also be used to investigate the aerodynamic characteristics of heat exchangers and plenum design. Additional investigations could be launched to address the inefficiencies of fans in an ACC, which might result in the reduction of parasitic power consumed by axial flow fans in power stations. This would have a direct impact on the efficiency of power stations and would ensure increased availability of electricity for consumption.

1.8. Thesis Overview

This report is organised into eight chapters and four appendices.

Chapter 1 introduces the research project, which focuses on the background, problem statement, scope, limitations, objectives, methodology and significance of the study. In Chapter 2 pertinent literature related to axial flow fans, types of Air-cooled condensers, their performance in a BS 848 Type-A test facility and the reason for constructing the MSACC facility, is reviewed. The chapter also identifies discrepancies and inadequacies found in the BS 848 in the reviewed literature.

Chapter 3 provides the theoretical background calculations for defining the operating point of the axial flow fan of an ACC. In Chapter 4, the design and technical review of the MSACC is discussed. In the same chapter, the manufacturing, construction and assembly of the MSACC is also outlined, followed by an examination of the testing procedure of the MSACC in Chapter 5.

Chapter 6 compares the results of the MSACC to the BS 848 Type-A test facility, after, which conclusions and recommendations are presented in Chapter 7.

Appendix A contains the layout of the laboratory and general dimensions the MSACC, results of the B2-fan tested in BS848 test facility at the University of Stellenbosch.

Appendix B expresses the operating point calculations of the MSACC draft. This Appendix chapter reviews the assumptions and example of the calculations performed to obtain the MSACC draft equation and estimates the operating points of B2-fan in the MSACC using experimental data.

Appendix C includes the test results obtained at the Induced and Forced wind tunnels. It also includes test results of the induced wind tunnel leakage test, anemometer distance tests and the perforated plate pressure loss characteristics.

Appendix D comprises the MSACC test data and MSACC B2-fan Performance Sample Calculations

2. LITERATURE REVIEW

2.1. Introduction

This chapter highlights literature reviewed on axial flow fans, their performance, applications, and limitations. The study was limited to axial flow fans and their performance and application in a forced draft ACC. The forced and induced draft designs of ACCs are discussed, providing advantages and disadvantages of their use. The chapter discusses the BS 848 Standard, which is used to evaluate the performance of axial flow fans. The limitations of the fan test standards and problems experienced in an ACC are emphasised.

2.2. Turbomachines

Forced draft ACCs are mechanically operated heat exchangers, which make use of dynamic pumps to drive the air improving the heat exchanger's heat rejecting performance. Cengel and Cimbala (2010), Dixon (1978), Wallis (1983) describe a fan as a dynamic pump, which is a type of turbomachine. Turbomachines are mechanical devices that transform mechanical energy into kinetic energy, or vice versa. Dynamic pumps are devices that transmit energy to continuously moving fluids with a dynamic motion. A fan operates by creating a pressure differential within a control volume. Fluids move in respect to this pressure differential from a high pressure to a low-pressure region.

2.2.1. Application of axial flow fans

Axial flow fans have many industrial applications and are mainly used to produce air draft through heat exchangers. Such fans are categorised into two types: open or ducted. The open type application would typically be a household electric floor fan (Cengel & Cimbala, 2010). The ducted arrangement is mainly used in the cooling of electronic equipment such as personal computers or servers, air conditioning and ventilation systems or in the ACC of a power station (Cory, 2012).

2.2.2. Ventilation system and fan selection

A fan system is defined as a ventilation system, where air is pumped through a ducted channel and components that resist the flow. A ventilation system's hydraulic losses are composed of the following: expansion, contraction, bends, entrance and exit losses (Mann, 2006). The pressure losses are expressed in terms of a loss coefficient K_l . From this, the pressure loss may be defined as:

$$P_{a_l} = K_l * \rho_a * v_a^2 / 2 \text{ [Pa]} \quad (2.1)$$

When all the loss coefficients of the ventilation system are available, the total pressure loss of the ventilation system is expressed as:

$$P_{aT} = \sum_{j=1}^n K_{l,j} * \rho_a * \frac{v_{aj}^2}{2} [Pa] \quad (2.2)$$

The equation above demonstrates that the pressure loss of the ventilation system increases with the square of the flow rate. Plotting the total pressure loss as a function of the flow rate is defined as the system or demand curve, an example of this is given in Figure 2-1. A characteristic fan curve is a graphical representation of the relationship between volumetric flow rate and hydraulic losses in a ventilation system (Mann, 2006). The intersection point of demand and fan pressure curve is known as the operating point (Cory, 2012), this is the static pressure and volumetric point at, which the fan can operate within the particular installed ventilation system. The operating point is designed to take in account the most efficient point of fan. Influencing the system's loss coefficients will change the operating point and will result in an inefficient operating system.

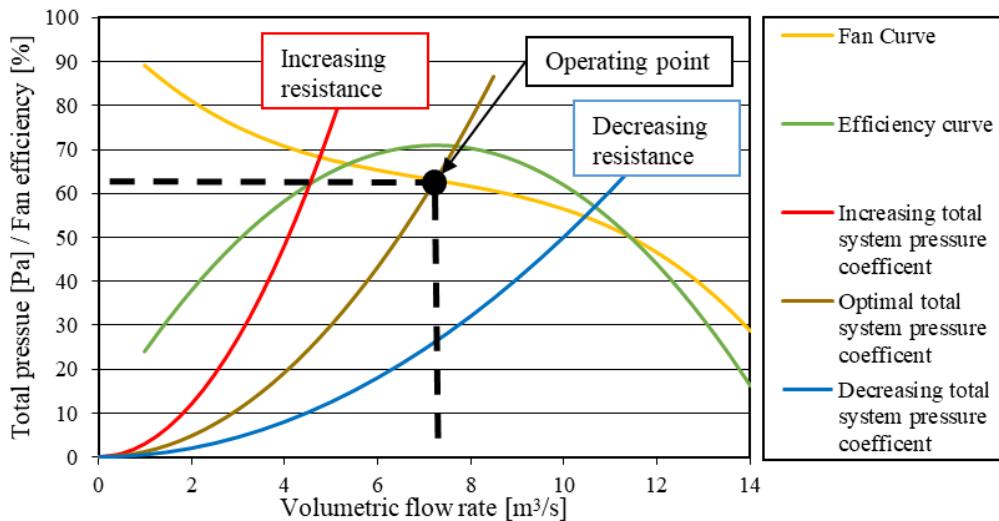


Figure 2-1: Characteristic fan curve, system resistance curve and duty point

Indeed, fan selection is an important aspect of HVAC systems, such as air conditioner systems and mechanical draft condensers, and is determined by matching the fan's performance curve to the total system flow resistance (Kröger, 1998). The fan's performance is determined by a standardised fan test (Louw, 2011). The internal flow resistance is determined either empirically or experimentally.

Fan selection is based on matching an ideal fan characteristic curve to the resistance or pressure drop of the components in the system. Fans are usually selected from an existing range of models and sizes, rather than designed specifically for a particular application. The selection is based on the calculated airflow and pressure requirements of a system (Lawrence Berkeley National Laboratory, 2003). The system resistance is determined from OEM published data for the drag forces acting

on different bodies immersed in a flow field, or from the characteristics of certain components of the duct. Due to the large scale of air-cooled condensers, the total pressure loss of each component in the system is determined empirically.

Space and structural constraints may have a significant impact on fan selection. In addition to dimensional constraints for the available space for the fan itself, issues such as maintenance access, foundation and structural support requirements should be considered. Investigations in the pumping requirements for the fan ventilation systems indicated that a system resistance curve is required to characterise and understand the impact of the fan's operating point (Cengel and Cimbala (2010), Cory (2012), Vemco Inc. (2016) and White (2003)). Variable drive characteristics, energy consumption and efficiency requirements are based on the system's resistance curve. The above-referenced authors state that the following aspects aids understanding of the said curve:

- A system's resistance curve is defined as a unique curve for each system. A system's resistance curve is the relationship between the volumetric flow rate (units of \dot{V} in $[m^3/s]$) and the total resistance the system offers to flow, which is called the pressure loss (units in Pascals)
- With a fan installed, the operating point is determined at the point where the fan performance curve and the system resistance curve intersect. The system resistance curve is independent of the fan performance curve.

The fan curve is regarded as an independent parameter and is not influenced by the installed system. The performance of the axial flow fan is matched to the required airflow and system pressure loss.

2.2.3. Fan specifications

Determining the specifications for the performance requirements of the fan is an essential design activity; the designer must pay careful attention to the commercial and technical aspects that affect the choice of fan. Focusing on the technical requirements, Blake (2013) and Lownie (2008) point to the primary specifications that influence the choice of fan:

1. Establish the operating range of the fan for the given system. The duty point will deviate throughout the lifetime of the equipment and allowance must be made for future off-duty operation. Thus, the operating point must be described for a duty envelope.
2. Installation configurations that influence the behaviour of the fan (parallel or serial; directly mounted or inlet guide vanes; fan bridges or struts).

3. Environmental operating conditions such as corrosion, adverse winds, erosion, blade loading, fatigue, noise:
 - a. As highlighted by the Lawrence Berkeley National Laboratory (2003) temperature range can determine the fan type and material selection. In high-temperature environments, many materials lose their mechanical strength.
 - b. Fouling effects and anticipated future capacity expansion, encourage the tendency to increase the specified size of a fan/motor assembly (Lawrence Berkeley National Laboratory, 2003).
 - c. High acoustic levels promote worker fatigue and hearing loss. The noise generated by a fan depends on fan type, airflow rate and pressure duty (Lawrence Berkeley National Laboratory, 2003).
4. Performance testing of fans:
 - a. Which standard fan performance test will be used?
 - b. How does the test standard affect the outcome of the fan's performance tests?

Due to the characteristics of an axial flow fan, a low-pressure differential, but a high flow rate is ideal for ACC application (Improving heat transfer coefficient of heat exchanger). The Lawrence Berkeley National Laboratory (2003) states other key advantages of axial flow fans are their compactness, low cost and their light weight compared to centrifugal blowers.

2.3. Power Plants

In most coal-fired power stations, the Rankine cycle is utilized to generate electricity. In Figure 2-2, an ideal Rankine cycle along with a TS-diagram is shown. Water is the most common working fluid and is heated to become high-pressure and -temperature steam. Following the figure points below, at state one, the pump is supplied by saturated liquid from the condenser and pumps the liquid to a high pressure to state two. The liquid is super-heated between states two and three by the boiler. It is this superheated steam drives the turbine at state three and four, producing electricity (Muiyser, et al., 2014). The working fluid leaves the turbine as saturated steam (state four). Between the final states, the steam at a constant pressure is condensed in a condenser. Make-up water is required due to leakage at the many pipe seals and joints in the power station. This is usually added before the condenser to reduce the temperature of the saturated steam entering the condenser (Langenhoven, 2016).

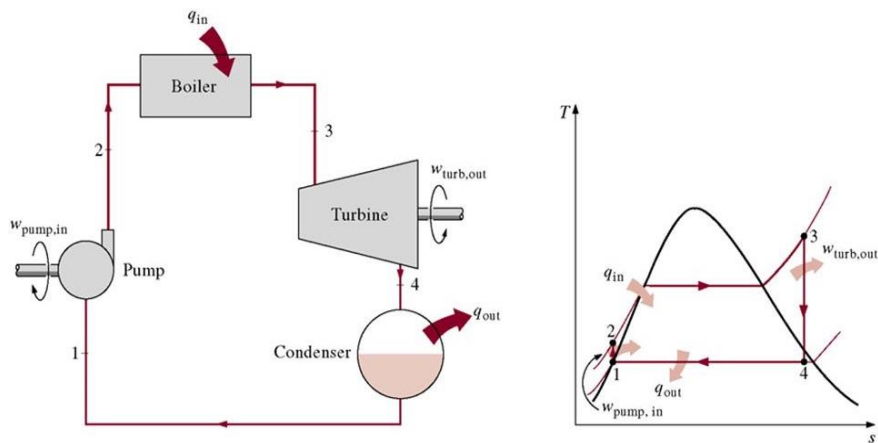


Figure 2-2: Simple ideal Rankine cycle with TS diagram (Cengel & Boles, 2011)

The amount of cooling required (during the condensing state, four to one) by the power plant is dictated by its size, thermal efficiency, environmental restrictions and is not limited by the type of fuel used. According to Cengel & Boles (2011), thermal efficiency is the fraction of the net work to total heat input and it is a measure of the performance of the power plant. The type of condenser is determined by both governmental regulations and capital limitations, which are imposed at the concept design phase of the power plant. The main purpose of the condenser is to condense the exhaust saturated steam from the turbine for reuse in the cycle, removing dissolved non-condensable gases from the condensate, conserving the condensate for re-use and to maximize turbine efficiency by operating at the lowest possible pressure (high vacuum).

The two distinctive cooling methods are known as dry or wet -cooling (Bredell, 2005). The dry-cooling requires air as a medium of cooling, while wet cooling makes use of water as the heat sink to cool the fluid. The two categories of dry cooled heat exchangers are based on the method used to produce a draft through the heat exchanger bundle (HEB): natural and mechanical draft. A natural draft cooling tower makes use of the difference in densities (buoyancy effects) between the cool ambient air and heated air to induce airflow over the heat exchanger. A mechanical draft cooling tower makes use of a mechanical device, such as an axial flow fan to produce airflow through the HEB (Meyer, 2000). Figure 2-3 shows different wet and dry methods (wet and dry, natural and forced draft) used in power stations.

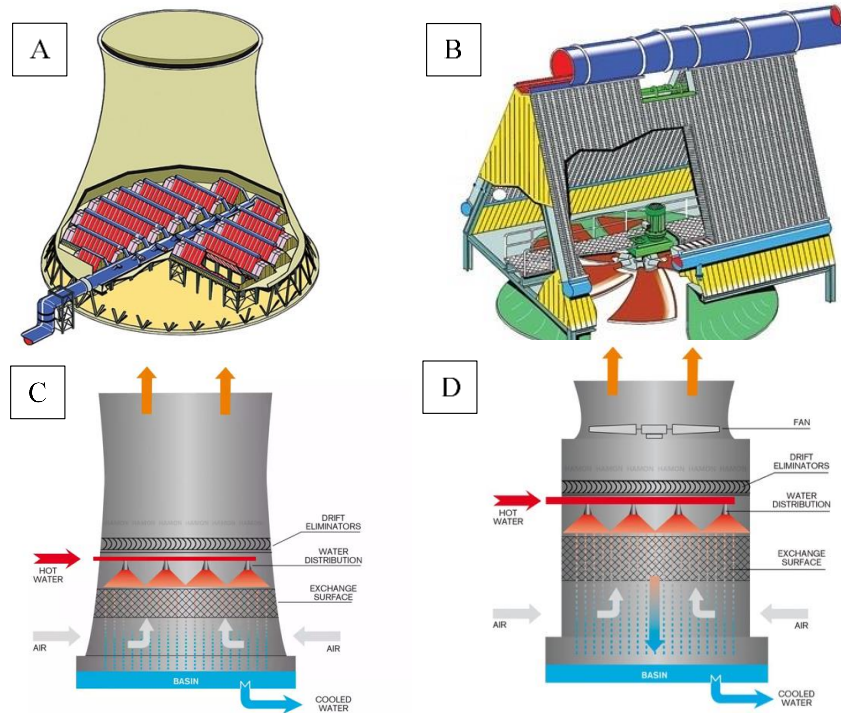


Figure 2-3: Types of condensers: (A) Dry natural-draft cooling tower; (B) Dry forced-draft cooling tower; (Powermag, 2016) (C) Wet natural-draft cooling tower; (D) Wet forced-draft cooling tower. (Hamon Group, 2016)

2.4. The Air-cooled Condenser

A forced and induced draft ACC unit typically consists of one or more axial flow fans, paired with a condenser unit arranged in a V or A -frame arrangement as illustrated in Figure 2-4, below.

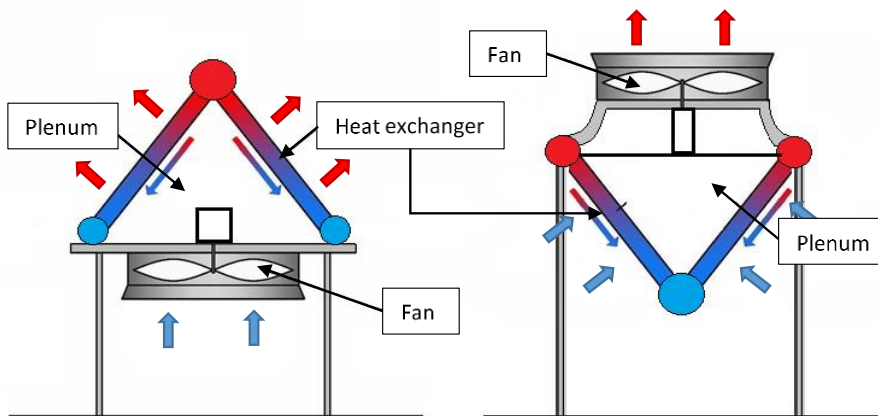


Figure 2-4: A-frame (forced draft) and V-frame (induced draft) air cooled condensers

The condenser unit and its accessories impose an energy loss on the system, which drives the energy consumption of the fan-unit. Therefore, the complete system is designed to maximise the heat transfer rate of the condenser unit and to minimise maintenance cost and the unit's energy consumption (Melo, et al., 2006). Kröger, (1998) clarifies that the heat transfer rate of the condenser unit is a function of the temperature and flow rate of the working fluid, the surface area of the fins and air properties flowing through the condenser unit.

In an ACC, the heat exchanger is used to condense the steam coming from the turbine. Heat is transferred into the environment through the finned tubes. These finned tubes are grouped together in units known as HEB. The plenum is described as the cavity between the axial flow fan and the heat exchanger. It allows the transition of air between the fan and the HEB and houses the electrical motor, reduction gearbox and the maintenance walkway (Meyer, 2000).

The main contributor to ACC's efficiency is the difference in temperature between the condensed fluid and the high-pressure steam. If the ambient temperature is very high or if there are non-condensables accumulating in the condenser, the heat transfer rate decreases and the turbine outlet pressure increases, lowering the turbine and power plant efficiency. The lower the temperature of the condensed fluid entering the boiler house, the more efficient the power station becomes. The heat transfer rate of the HEB is a function of the temperature and volumetric flow rate of the two fluids (working fluid and the ambient air). Further research in ACC and axial flow fan design can improve the volumetric flow rate and air velocity distribution in the plenum and heat exchanger (Augustyn, 2013) (Singh, 2013). Venter (1990) indicates that the HEB can be installed vertically, horizontally or at an angle. When installing the HEBs in an A-frame arrangement, the plot size of land required for the ACC is reduced and the number of HEBs increased, thereby effectively increasing the size of the surface area available for heat rejection. The A-frame arrangement is the arrangement most commonly used in direct dry cooled power stations.

2.4.1. Types of forced draft air-cooled condensers

The forced draft design is based on the use of fans producing the required airflow (draft equation), as explained by Kröger (1998). While natural draft designs have the disadvantages of high capital costs and a low aesthetic appearance, the running costs are low. On the other hand, the forced draft design has a lower capital investment, but its running costs are higher and, as Venter (1990) points out, the latter is more easily influenced by ambient conditions.

There are two types of mechanical draft ACCs configurations namely: induced and forced draft. As indicated in Figure 2-4, the fan is located downstream of the HEB in the induced draft design and creates a low-pressure zone in the plenum. However, in the forced draft design, the fan is located upstream of the HEB, creating a high-pressure zone within the plenum (Bredell, 2005) (Meyer, 2000).

Venter (1990) highlights another distinction: the forced draft systems are recognised by having an internal plenum pressure that is above atmospheric pressure. The opposite is true for an induced draft, where the pressure in the plenum is below atmospheric pressure. The advantages of the forced configuration, in contrast to the induced draft configuration, are as follows:

- Forced draft configuration requires less power to pump air (Le Roux, 2010).
- Since the fan is situated on top of the heat exchanger, the induced draft configuration requires more material to support the fan at the top of the heat exchanger and the fan experiences more thermal load (Meyer, 2000).
- The forced draft configuration has lower exit kinetic energy loss to the environment and in contrast to induced draft configuration, there is no exit swirl velocity (Meyer, 2000).
- As shown in Figure 2-4, the fan is placed downstream of the heat exchanger in the induced configuration. The materials used to construct the fan and its structural support components must therefore withstand the air temperatures that exit the HEB (Louw, 2011).
- The induced draft configuration requires a fan with a larger diameter to produce the same mass flow rate as the forced draft configuration (Meyer, 2000).

The disadvantages of the forced draft configuration are:

- The performance of the forced draft heat exchanger deteriorates due to hot plume recirculation. The ingested airflow has a higher dry-bulb temperature and decreases the effectiveness of the heat transfer process and results in partial condensation of steam (Kröger, 1998). Thus, it is required that the power plant must reduce its power setting (Langenhoven, 2016).
- Low air velocity at the exit of the HEB, coupled with adverse wind conditions, may cause plume recirculation, reducing the heat transfer rate of the ACC (Meyer, 2000).

2.4.2. ACC performance

ACCs used in power stations are constructed in an array format. According to van der Spuy et al. (2010) these arrangements are highly susceptible to windy conditions, which impact on the performance of the fans. The drop in performance is due to distorted inlet airflow conditions. In the ACC unit, the fan is horizontally orientated and the air entering underneath is required to change its direction rapidly in order to flow through the fan. Under windy conditions, this change in airflow direction produces flow separation at the bell mouth, leading to distortion of the fan inlet flow. The distorted inflow conditions lead to a reduction in volumetric flow

rate through the fan, leading to an underperforming ACC. As reported by Van der Spuy et al. (2010) and Venter (1990), the fans which are affected by these distorted inlet flow conditions are located at the outer perimeter of the ACC array.

It is noted that the axial flow fans in the centre of the array experience off-axis inflow. This is due to fans influencing each other (van der Spuy, et al., 2010). Therefore, it should be considered that different factors may affect the behaviour of the inflow into the fan array, as listed below:

1. Obstruction or proximity of solid surfaces and the height of the floor underneath the constructed ACC may inhibit the flow of air into the fan (Thiart, 1991).
2. Proximity of other fans also play a role in the reduction of airflow through the fans (Thiart, 1991).
3. Crosswinds have a significant influence on the performance of the axial flow fans in the ACC and affect the airflow rate through the fan. They distort the flow of air into the latter and cause regions of recirculation (van der Spuy, et al., 2010; Le Roux, 2010; Muiyser, et al., 2014).

Another interesting factor is related to contaminant build up on fan blades and heat exchanger. Contaminant build-up on fan blades may cause a reduction in airflow, fan blade surface degradation and fan power imbalance. Build-up problems are promoted by a shallow blade angle with surfaces that allow contaminants to collect. This was confirmed during an interview with Langenhoven (2016) at the Van Eck power station, where he pointed out that contamination by the gearbox oil and dust increases the fouling on the ACC fan blades and heat exchanger.

Furthermore, Putman and Jaresch (2002) indicates that the forced draft design enables condensate draining and collection and also ensures that there are no dead zones in the heat transfer surface. A high level of operating stability during load transients is experienced, while freezing is eliminated even with ambient temperatures as low as $-50\text{ }^{\circ}\text{C}$.

In view of the low thermal conductivity, density and heat capacity of air, finned tubes and fans are required. The larger surface area required to obtain a given heat removal rate (the area increases with an increase in the design ambient air temperature) also means that the footprint of air-cooled condensers is larger than their water-cooled equivalents. Another problem observed by Kröger (1998) and Putman and Jaresch (2002) is that the noise created by the large number of fans may introduce its own environmental problem. This high level of noise produced, reduces the widespread use of air-cooled condenser to a rural environment.

Meyer (2000), studying horizontal air-cooled heat exchangers which is typically used in the petrochemical industry, emphasised the need to understand the impact of plenum design and aerodynamic behaviour, which might improve air cooled heat

exchangers effectiveness and efficiency. His findings obtained on a scale test bench correlate with the characteristics seen in the industry. Meyer (2000) and Kröger (1998) added that the current method for specifying the fan does not take the entire installed system into account. They, however, suggested that the fan should be tested in the installed position to enable the investigator to choose the most suitable fan and arrangement.

Three research groups Beiler and Kröger (1996), Zhang and Yang (2015) and Rabas (1987) studied the maldistribution of exit airflow of an ACC. They found that the maldistribution influences the downstream tube rows in a multi-row HEB. The downstream tube rows experience a reduction in heat transfer performance and increased thermal loading characteristics. It affects the temperature profile between the HEB's tubes and causes the downstream rows to be gradually less effective. The present analysis was used by the researchers to evaluate the performance of the individual tube rows and ultimately the entire bundle. 'It is found that maldistribution occurring in well-designed air-cooled heat exchangers reduces the thermal performance by only a few percent' (Beiler & Kröger, 1996).

Due to the advantages of the forced "A" frame draft design and the widespread use of this configuration in industry, this research focused on the forced draft design

2.5. Standardisation of Fan Performance Testing

The performance of a fan is assessed experimentally per a fan standard. The most common industrial standard for axial flow fans is the British Standards (BS) Organisation's 848 standard, also known as ISO 5801. The fan test facilities at the University of Stellenbosch, was constructed according to the BS 848 Type-A standard.

2.5.1. Fan performance testing

According to Blake (2013), performance testing of fans is vital for the following reasons:

- 1 It provides a benchmark against which future changes in performance can be assessed.
- 2 Describing the performance of a particular fan with the aim of comparing it to other fans in its class.
- 3 Establish whether the manufacturer's claims related to performance are factual.
- 4 During maintenance, it provides a method for fault finding, overhauling or analysing the ventilation system in which the fan is installed.

Lownie (2008) argues that the fan's performance is influenced by the installed system and matching the individual performances of the fan and the system total

pressure loss (Making use of the draft equation) does not guarantee the calculated operating point. Presuming that the manufacturer's geometric tolerances are adhered to when constructing the fan, the set performance target tolerances in the given test facility and test parameters as well as assumptions will be achieved. Lownie (2008) further suggests that the fan's performance will not necessarily be maintained in the installed system. The designer needs to account for installation effects, additional aerodynamic system ducting deficiencies, operating stability sensitivities and manufactured geometrical variations, all of which influence the fan's duty point.

2.5.2. The types of BS 848 standard test arrangements

The BS 848 part 1 standard is specifically able to relate fan performance characteristics to ducted connections. The BS848 test standard test allows for comparative verification, analysis and independent reproduction between different test facilities and fans. Four standard fan installation types are recognised by the BS 848 standards part 1, as indicated in Figure 2-5 below:

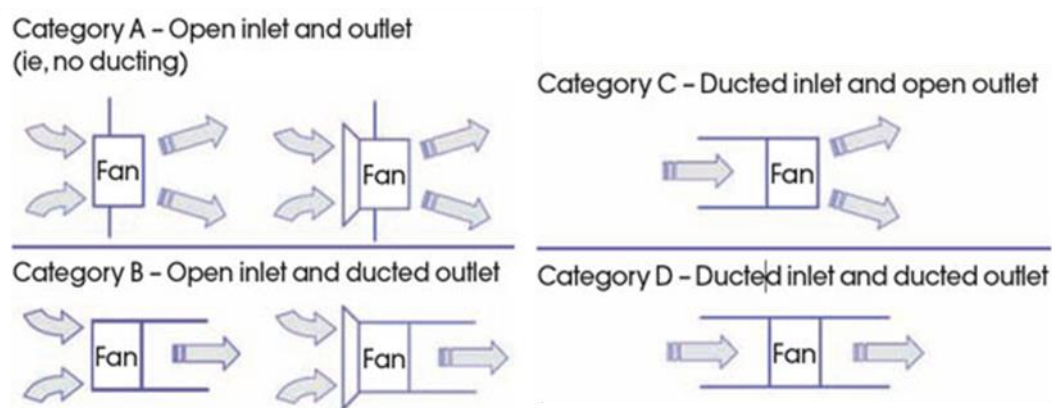


Figure 2-5: Standard fan installation types (Dwyer, 2012)

The installation types provide flexibility in the methods of determining fan flow rates. The test types a provides a method to test different types of fan setup or installation conditions. The installation types also make use of flow straightener in Type-B and -D, this is designed to dissipate any swirl energy present in the air flow.

2.5.3. Limitations of ISO 5801 / BS 848 part 1 standard

According to Meyer (2000), Lownie (2008), Putman and Jaresch, (2002) and Cory, (2012), standard test configurations represent the ideal case of a real system and the performance figures obtained are limited only to that test setup. The test setup cannot depict all the configurations in which the fan can be installed; they serve rather as a general guideline that correlates to the fan's eventual application. They predict that the fan performance is affected by the additions made at the inlet and outlet of a test cell. Meyer (2000) further reasons that the conditions under which

the performance characteristics of an ACC fan are experimentally obtained are an inaccurate depiction of the actual fan's installed performance.

Meyer (2000) highlights that two of the standard setup types (A and C) are without flow straighteners and the static and total pressure rise definitions of the two installation groups (A and C vs B and D) are therefore not compatible with each other. He argues that the use of the different installation types was motivated by the desire to secure a simple method to measure the flow field's intricate pressure and velocity distributions. Furthermore, the applications of fans are directly affected by the test standard and the conditions thereof. Meyer (2000) points out that the draft design and the HEB have a significant impact on the choice of fan. Therefore, there was a need to produce a test bench to provide data on the effect that the system has on the fan's performance. This test bench also served as a platform on which different fan configurations, draft designs and different HEB designs could be tested.

Lownie (2008) drew attention to the point that descriptive testing standards are required because the performance of the fan, internal ducting and flow system elements are dependent on:

- The method of measurement.
- The physical installation conditions.
- The standards used and the assumptions made in acquiring the results.

ISO 5802 was issued to overcome the limitations of ISO 5801 and provides a comprehensive variety of in-situ tests to match the installed conditions. These adaptations are designed to produce installed conditions in the test bench. ISO 5802 also distinguishes between fan adjustment devices such as the variable pitch arrangement and variable speed drive. The fan's operating points are determined by running the fan at various volumetric flow rates. The most probable operating point is determined by the intersection of the system resistance curve and the fan test curve. As this is not possible in every installation, ISO suggests that additional modifications are required for the test facility of the manufacturer to produce the same installed conditions required by the purchaser. These arguments are supported by Blake (2013), Meyer (2000) and Lownie (2008). Kröger (1998) also recommends that if the fan system geometry deviates considerably from one of the standard installations, performance tests should be conducted on the system or a model thereof.

The current test bench facility at the University of Stellenbosch was constructed conforming to the ISO 5801 / BS 848 Type-A standard, but is not equipped to test all the influencing parameters of the axial flow fan. Owing to these limitations, an investigation into the design, development and construction of a small-scale ACC was necessitated.

2.6. Performance measurement of ACCs

The MSACC test setup followed a similar approach that of the mentioned researchers below:

Venter (1990) measured the air velocity distribution in full scale ACC unit. Vane anemometers measuring directly downstream of the fan rotor, directly downstream of the fan inlet safety grid (directly in front of the fan rotor) and at the outlet of the A-frame. Static pressure difference between the fan inlet and outlet were measured; the probes were attached to a rotating beam at the fan inlet.

Mortensen's (2011) research centred on the influence of high windy conditions on ACC efficiency. This required the improvement in the existing ACC design with outlet wind guides to improve air flow to the HEBs. The researcher measured steam-flow and -temperature, turbine backpressure, fan speed and A-frame air speed. The research concluded with an improvement in heat transfer coefficient of 5% at high wind conditions and 1% at low wind speeds.

Muiyser, et al.'s (2014) research focused on the measurement of inlet air flow velocity (using ultrasonic and propeller anemometers downstream of the fan safety grid) and fan blade and gearbox loading of a single fan located on the perimeter of a power plant's large-scale ACC unit. The researcher determined that windy conditions causes cross-flow at the fan inlet and affects the air flow into the fan. Fan blade loading is dependent on the relative angle at which the flow approaches and leaves the fan blade, which is influenced by the air volumetric flow rate through the fan and the inflow conditions. He also concluded that fan blade loading amplitudes are affected by the inlet air flow distribution and if the inlet air flow is not uniform, the aerodynamic forces applied on the fan will vary depending on the blade's rotational position. This fluctuation in blade loading then causes the fan blade to vibrate.

3. THEORETICAL ANALYSIS

3.1. Introduction

As explained in the literature study, an ACC can be modelled as a ventilation system, because the system consists of a fan with inlet and outlet resistance losses. In this chapter, a theoretical analysis that focuses on the performance predictions of the B2-fan in the MSACC is presented. Using experiments, various researchers determined the influence of each component's pressure loss coefficient in the A-frame by changing its geometrical characteristics.

In Meyer and Kröger (2001) and Mohandes, et al. (1984) experimental results demonstrate that the inlet airflow losses are independent of the average air velocity through the heat exchanger. For a set of particular heat exchangers, their findings indicated a disproportionate relationship between inlet airflow losses and the orientation of the heat exchanger finned tubes (semi-apex value).

Furthermore, van Aarde and Kröger (1993) modelled the isothermal flow losses through an array of A-frame finned tube heat exchangers. They produced correlations that describe these losses, which were derived from small scale-model tests conducted on different V-bundle configurations, where each simulated a section of a typical A-frame array. They found that the downstream flow losses behind a V-bundle section were significantly influenced by the semi-apex angle, the process steam duct diameter and the distance between the A-frames.

This provided the foundation on which the mathematical model used in this research is based. However, it should be noted that each ACC layout differs and its performance characteristics are limited to each individual geometrical setup. The losses through a section of array consists of the sum of inlet losses ($K_{i\theta}$), frictional losses (K_f), exit losses through the bundle (K_e), jetting losses (K_{dj}), and outlet kinetic losses (K_o) (van Aarde & Kröger, 1993) and are discussed to understand the total loss coefficients of an ACC's heat exchanger in context. This chapter defines the MSACC system as a mathematical model in terms of the B2-fan's airflow rate and pressure rise, and pressure loss coefficients of the following components: guide fins, perforated plates, plenum, fan bridge and safety screen.

3.2. Air-cooled condenser draft equation

To determine the operating point for the MSACC, the draft equation must be satisfied. The system pressure losses of an ACC are described by referring to Figure 3-1 below:

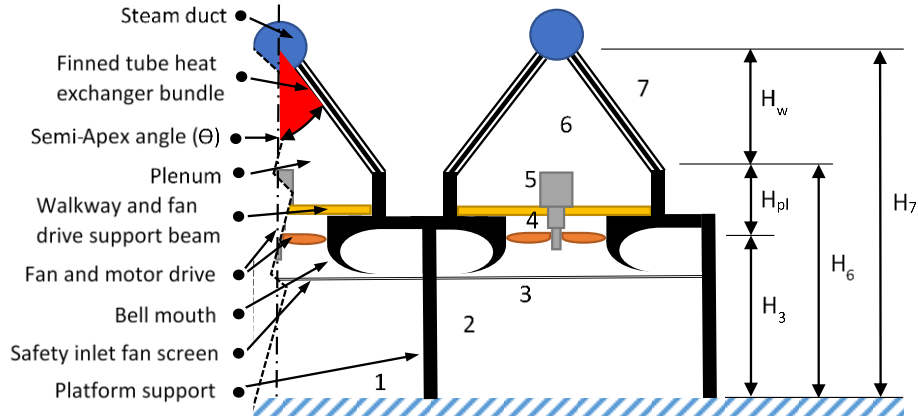


Figure 3-1: Forced air-cooled condenser

Equation 3.1 expresses all the pressure loss coefficients of a forced draft air-cooled condenser. The platform support pressure loss coefficient is given by term K_{ts} , the pressure loss coefficient of the bell mouth is presented by K_{Fsi} . The other obstacles located before the fan are grouped into the upstream pressure loss coefficient K_{up} . The fan static pressure and the fan kinetic velocity distribution factor is termed ΔP_{Fs} and α_{eF} respectively. The plenum can contribute to the increase in static pressure and the plenum recovery coefficient K_{pl} takes this into account. The downstream loss coefficient (K_{do}) takes into account the pressure loss due to internal A-frame obstacles like the fan bridge. The loss coefficient across the heat exchanger is defined by K_{he} and α_{e6} is the kinetic energy factor ($\alpha_{e6} \approx \alpha_{e7}$). A_c and A_{fr} represent the bell mouth casing area ($A_3 = A_4$) and total frontal area of the heat exchanger, respectively. The draft equation is shown below:

$$\begin{aligned}
 P_{a_1} - P_{a_7} = & \left(\frac{K_{ts}}{2\rho_{a_1}} \left(\frac{m_a}{A_2} \right)^2 \right) + \left(\frac{K_{Fsi}}{2\rho_{a_3}} \left(\frac{m_a}{A_c} \right)^2 \right) + \left(\frac{K_{up}}{2\rho_{a_3}} \left(\frac{m_a}{A_3} \right)^2 \right) \\
 & - \left[\Delta P_{Fs} + \frac{\alpha_{eF}}{2\rho_{a_3}} \left(\frac{m_a}{A_c} \right)^2 \right] + \left(\frac{K_{pl}}{2\rho_{a_4}} \left(\frac{m_a}{A_c} \right)^2 \right) + \left(\frac{K_{do}}{2\rho_{a_3}} \left(\frac{m_a}{A_4} \right)^2 \right) \\
 & + \left(\frac{K_{he}}{2\rho_{a_{56}}} \left(\frac{m_a}{A_{fr}} \right)^2 \right) + \left(\frac{\alpha_{e6}}{2\rho_{a_6}} \left(\frac{m_a}{A_{fr}} \right)^2 \right)
 \end{aligned} \quad (3.1)$$

3.2.1. Upstream and Downstream Obstacles Affecting the Fan

The safety screen and fan bridge are two obstacles that, respectively, are upstream and downstream of the fan. It was predicted that these two objects might present a pressure drop in the air stream. The loss coefficients are a function of the obstacles' projected area, A_{ob} , and the distance x from the axial flow fan. The upstream (and downstream) fan loss coefficient is expressed as:

$$K_{up} = \frac{2 \Delta p_{up}}{\rho v^2} = \frac{2 \rho \Delta p_{up}}{(m_a/A_e)^2} = f\left(\frac{x}{d_c}, \frac{A_{ob}}{A_c}\right) \quad (3.2)$$

Where $A_e = A_c - A_h$ and A_c is the casing cross-sectional area and A_h is the hub cross sectional area. The values of the loss coefficients are discussed in Appendix B.

3.2.2. Mean flow incidence angle

Kröger (1998) highlighted that due to the flow distortion that occur downstream of the bundle, the actual mean flow incidence angle will not be uniform along the bundle face and is generally smaller than the semi-apex angle (θ) as shown in Equation (3.3). The semi-apex angle is defined as half of the angle that is between the HEBs on top of the A-frame, this is depicted by the red angle in Figure 3-1. For a typical A-frame semi-apex of 30° , the mean flow incidence is found to be:

$$\theta_m = 0.0019 \theta^2 + 0.9133 \theta - 3.1558 = 25.953^\circ \quad (3.3)$$

3.2.3. Inlet pressure loss coefficient

(Mohandes, et al., 1984) conducted an experimental study of total pressure loss coefficient for inclined resistances (which included finned tubed heat exchangers and perforated plates). He found that entrance losses are affected by the incidence angle. The total pressure loss coefficient, due to oblique flow, is given by the following equation:

$$K_{i\theta} = \left(K_c^{0.5} + \frac{1}{\sin \theta_m} - 1 \right)^2 \quad (3.4)$$

For parallel plate or fins tubes, the viscous component of pressure loss is unaltered when the bundle is at an incidence. It the entrance inertial loss which is affected by the incidence (Kröger, 1998)

$$K_{hei\theta} = \left[\left(\frac{1}{\sin \theta_m} - 1 \right) \left(\left\{ \frac{1}{\sin \theta_m} - 1 \right\} + 2 K_c^{0.5} \right) \right] + K_{he} \quad (3.5)$$

According to (van Aarde & Kröger, 1993), the entrance contraction loss coefficient (K_{ci}) is based on the free-stream velocity, for plate fins it defined as:

$$K_{ci} = \frac{K_c}{\sigma_{21}^2} = \left(1 - \frac{1}{\sigma_c}\right)^2 / \sigma_{21}^2 \quad (3.6)$$

Where term σ_{21} is the area ratio between the open area and the total area of the fins and the contraction area ratio (σ_c) is different for parallel plates are defined by the following equation:

$$\sigma_c = 0.6144517 + 0.04566493 \sigma_{21} - 0.336651 \sigma_{21}^2 + 0.4082743 \sigma_{21}^3 + 2.672041 \sigma_{21}^4 - 5.9634169 \sigma_{21}^5 + 3.558944 \sigma_{21}^6 \quad (3.7)$$

3.2.4. Jetting loss coefficients

Van Aarde & Kröger (1993) investigated isothermal flow losses through an array of A-frame air cooled condenser, and derived pressure loss coefficients from a small-scale test-bench. The scale test results were compared to a full-scale air-cooled heat exchanger to find the influence of the semi-apex angle, steam duct diameter and the distances between the A-frames. The following figure shows a section of array of A-frames which layout is typical of an Air-cooled condenser setup at a power station. This is included in the thesis for completeness.

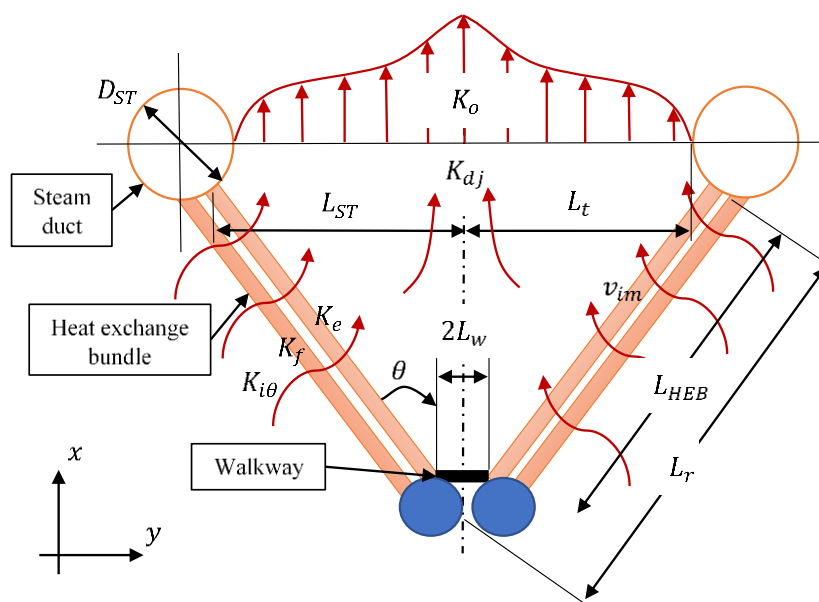


Figure 3-2: Section of an array (Adapted from van Aarde & Kröger, 1993)

The dimension of the a-frame heat exchanger is defined by the following terms: L_{HEB} , length of the HEB L_r , reference length of the HEB, L_w , length of the

walkway, L_{ST} , length to process stream duct length, D_{ST} , diameter of steam duct, L_t , total length of A-frame including steam duct.

The jetting losses occur due to the acceleration of the air flow past the steam header and is equated as:

$$K_{dj} = \left(\left[\left\{ \frac{(-2.89188 * L_w)}{L_{HEB}} + \left(2.93291 * \left(\frac{L_w}{L_{HEB}} \right)^2 \right) \right\} * \frac{L_{HEB}}{L_{ST}} * \frac{L_t}{L_{ST}} * \left(\frac{28}{\theta} \right)^{0.4} \right] + \left[\frac{L_{HEB}}{L_r} * \left(\frac{L_{ST}}{L_t} * \exp(2.36987 + (0.058601 * \theta) - (0.00338797 * \theta^2)) \right)^{0.5} \right] \right)^2 \quad (3.8)$$

where θ is in degrees. The jetting pressure losses are however not relevant to the MSACC test setup.

3.2.5. Outlet loss coefficients

The outlet losses arise when the air flow exits the HEB and expands. This is defined by van Aarde and Kröger as:

$$K_o = \left[\left(\frac{L_{ST}}{L_t} \right)^3 * \left\{ \left(-2.89188 * \left(\frac{L_w}{L_{HEB}} \right) \right) + \left(2.93291 * \left(\frac{L_w}{L_{HEB}} \right)^2 \right) \right\} + 1.9874 - \left(3.02783 * \left(\frac{D_{ST}}{2 * L_t} \right) \right) + \left(2.0187 * \left(\frac{D_{ST}}{(2 * L_T)^2} \right) \right) \right] * \left(\frac{L_b}{L_{ST}} \right)^2 \quad (3.9)$$

Equations (3.8) and (3.9) are valid only for the following conditions:

1. $K_{he} \geq 30$, $20^\circ \leq \theta \leq 35^\circ$,
2. $0 \leq D_{ST}/2L_t \leq 0.17886$
3. $0 \leq L_w/L_{HEB} \leq 0.17886$

The MSACC does not represent a complete ACC array but rather a single A-frame as shown in the figure below:

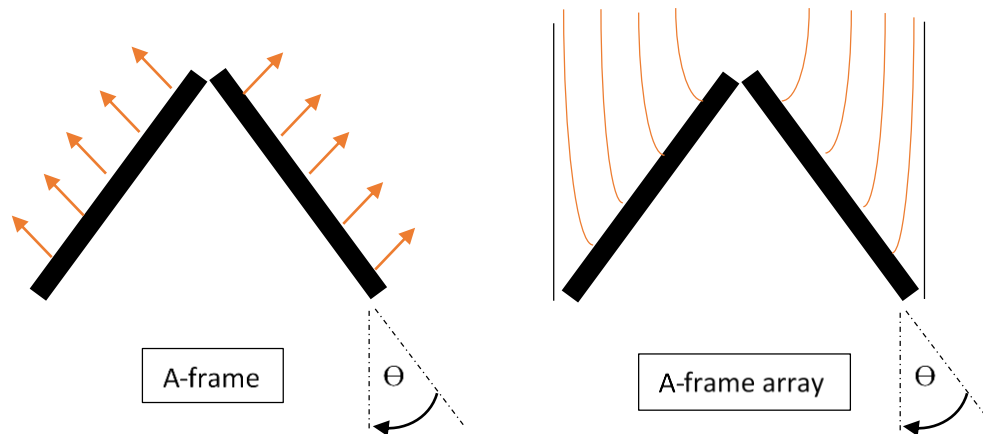


Figure 3-3: General picture of the flow through inclined finned tube bundles
(Adapted from van Aarde & Kröger, 1993)

The figure above shows the general flow pattern through two finned tube bundles of an A-frame and A-frame array. The MSACC conforms to the A-frame setup (Left) and therefore, the above equation is simplified to:

$$K_o = \left(\frac{A_{fr}}{A_{open}} \right)^2 \quad (3.10)$$

Where A_{open} , is the effective open area at the outlet of the A-frame.

3.2.6. Heat exchanger pressure loss coefficient

The total air flow losses through a section of HEBs is the sum of the inlet loss ($K_{i\theta}$), frictional loss (K_f), exit loss through the bundle (K_e), jetting loss (K_{dj}) and outlet losses (K_o) in the downstream (van Aarde & Kröger, 1993). The equation (3.11) below expresses this total loss coefficient as:

$$K_{\theta t} = K_{hei\theta} + K_f + K_e + K_{dj} + K_o \quad (3.11)$$

Note that the equation above is conservative at low air velocities through a HEB.

For Non-isothermal flow, the above equation simplifies to (Kröger, 1998):

$$\begin{aligned}
 K_{\theta t} = & K_{he} + \left[\left(\frac{2}{\sigma_{min}^2} \right) * \left(\frac{p_6 - p_7}{p_6 + p_7} \right) \right] \\
 & + \left[\left(\frac{2 * p_7}{p_6 + p_7} \right) * \left(\frac{1}{\sin(\theta_m)} - 1 \right) \right. \\
 & * \left. \left\{ \left(\frac{1}{\sin(\theta_m)} - 1 \right) + (2 * K_{ci}^{0.5}) \right\} \right] \\
 & + \left[(K_{dj} + K_o) * 2 * \left(\frac{p_6}{p_6 + p_7} \right) \right]
 \end{aligned} \tag{3.12}$$

3.3. MSACC Theoretical analysis

3.3.1. Perforated Plates and Guide Fins

In order to control the airflow rate in the MSACC, it was decided to use perforated plates in array format to throttle the airflow. In the plenum of a large-scale ACC, a HEB has fins, which direct the airflow past the steam tubes. In the MSACC, guide fins are used to provide the same function. This setup was used to model the heat exchanger aerodynamic behaviour and provide a method for controlling the operational duty point of the MSACC. Various types of guide fin and perforated plate arrangements were experimented with, in a wind tunnel, to determine their characteristics and to decide on the optimum geometrical layout.

Perforated plates are categorised by the size of their holes and their gross area. These geometrical characteristics are described by the porosity of a perforated plate, which is defined as:

$$\beta = \frac{\text{Area of holes}}{\text{Total area}} = \frac{A_h}{A_a} \tag{3.13}$$

For perforated plates and grids with straight (non-bevelled) orifices with relative thin walls ($\frac{t}{d_h} = 0$ to 0.015), the pressure loss coefficient is defined as (Weber, et al., 2000):

$$K_s = \frac{(0.707 (1 - \beta)^{0.5} + (1 - \beta))^2}{\beta^2} \tag{3.14}$$

3.3.2. Safety Screen

Due to safety requirements, safety screen was required to cover the fan and moving components. The screen in front of the fan increased the inlet pressure loss coefficient and had to be accounted for. The following figure shows the general dimensions of a wire mesh (safety screen):

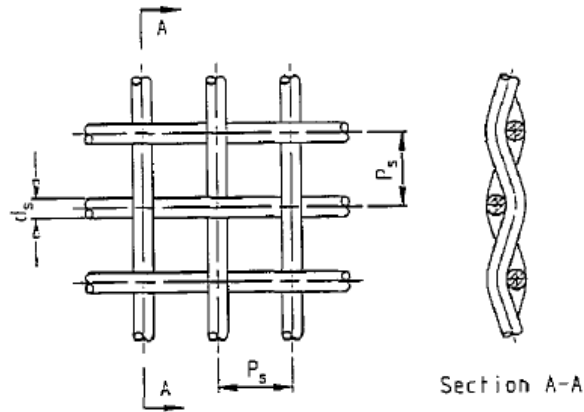


Figure 3-4: Safety screen dimension (Kröger, 1998)

In contrast to the perforated plates, safety screen is not just categorised by its hole's size and gross area, but it is also described by its wire thickness and distance between them. Using the dimensions shown in Figure 3-4 and redefining equation (3.13), the porosity of the safety screen wire mesh is defined as:

$$\beta_{ss} = \frac{\text{Area of holes}}{\text{total area}} = \left(\frac{1 - d_s}{P_s} \right)^2 \quad (3.15)$$

Due to the small size of the wire of the safety screen, the pressure loss coefficient is defined as:

$$K_{ss} = \frac{1 - \beta}{\beta^2} \quad (3.16)$$

In summary, the predictions made in this chapter impacted the design of perforated plate and fins' and were compared to the experimental results obtained from the MSACC. These comparisons are made in Appendix B.

4. DESIGN OF SMALL SCALE AIR-COOLED CONDENSER TEST BENCH

4.1. Introduction

This chapter outlines the design of the MSACC that was built at the University of Stellenbosch. To this end, the design limitations, requirements, concepts and technical review are addressed. Most of the individual components of the MSACC were laser cut before milling or turning to the exact dimensions. The component level's description of the MSACC is detailed below in Figure 4-1:

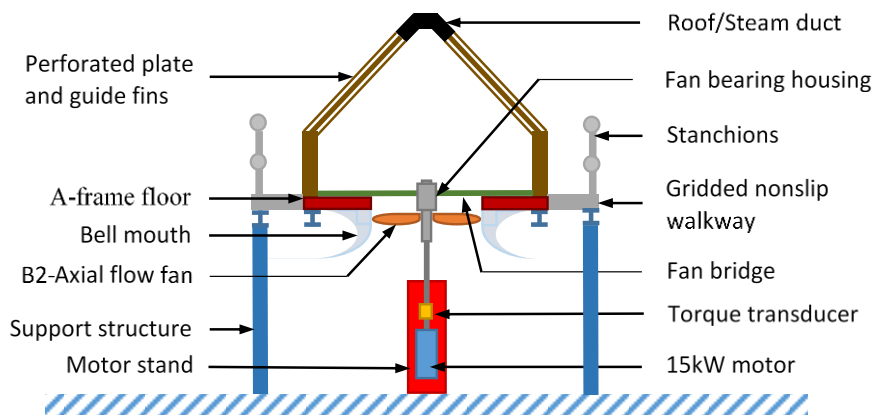


Figure 4-1: MSACC section view with major component scheme

The final complete MSACC as viewed at the ground floor and from the first floor of the laboratory is shown in Figure 4-2 below:

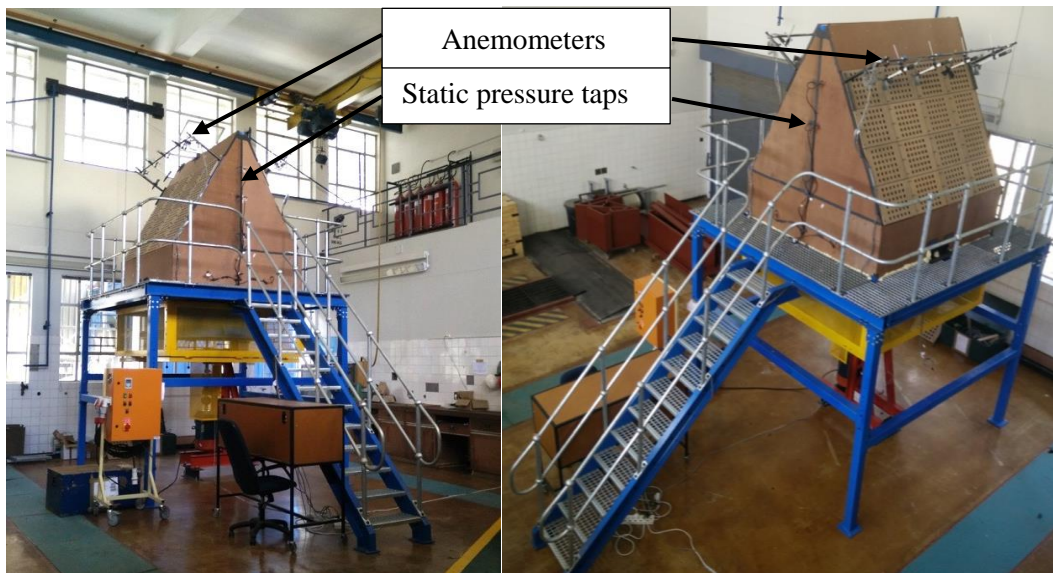


Figure 4-2: MSACC assembled with instruments

4.2. Design Limitations and Requirements

The following limitations were considered during the design phase of the MSACC:

- The facility was constructed inside an existing laboratory with limited floor space and height available. The entire MSACC had to be constructed in the thermal fluid laboratory with a height restriction of 5.2 meters from the floor to hook of the crane.
- An existing reconditioned three phase electrical motor was used; rated at 15 kW, 36A.
- The design of the MSACC had to accommodate the axial flow fans from the existing BS 848 Type-A test facility.
- The design was amended to accommodate donated material for the construction of the MSACC in order to reduce cost of the entire project.
- The horizontal distance between the vertical stands of the structure could not exceed 3,5 meters due to the limited space between the two service trenches.
- For safety reasons, no welding could be performed in the thermal fluid laboratory, owing to gas pipes located in the trenches which feed fuel to the combustion laboratory.

The following are the requirements that needed to be considered during the design phase of the MSACC:

- The existing B2 axial flow fan with a hub diameter of 1542 mm had to be used to facilitate direct correlation between the two test facilities.
- The design required minimal flow distortion at the bell mouth inlet.
- The configuration was required to conform to the forced draft design.
- Due to the size and weight of the motor, it could not be accommodated on top of the fan walkway bridge.
- The apex angle of the MSACC's A-frame was required to be sixty degrees.

The axial flow fan used in this research was the B2-fan, which is a concept rotor-only axial flow fan developed at the University of Stellenbosch by Bruneau (1994). The fan employs a free vortex design and the NASA LS GAW 2 aerofoil profile. In a free vortex design, the air flow swirl velocity component varies inversely with the radius and produces a highly-twisted fan blade. The performance characteristics of the B2-fan were experimentally obtained from Wilkinson and van der Spuy (2015). Appendix A shows the fan specifications and performance curves.

4.3. The Design Concepts Considered

Considerations were given to the following aspects during the design of the MSACC. A detailed discussion of the design of the MSACC is presented in subsequent sections.

4.3.1. Scaled unit

The advantages of a small-scale ACC test facility are as follows:

- It would be easier to manufacture the individual components at the available facilities.
- New measurement and manufacturing techniques can be trialled and tested.
- The height is lower than a full-scale ACC, which reduces associated risk.
- Influence of individual parameters can be measured.
- Lower capital outlay.
- Isolation of influencing parameters.
- The modular design facilitates the ability to add, remove and adjust components.

4.3.2. ACC plenum design

The three types of plenum designs were considered: the forced and induced draft and variable angle A-frame designs. The forced draft A-frame design was selected based on its widespread use in industry.

4.3.3. Inlet bell mouth

Two methods were considered for manufacturing the bell mouth for the MSACC, i.e. computer numerically controlled (CNC) manufacturing and fibreglass moulding. The inlet bell mouth was manufactured from fibreglass because of the associated cost benefits.

4.3.4. Arrangement of the electric motor

The following concept options were considered for the arrangement of the fan and electric motor:

- Motor-to-fan belt drive – This is the simplest and inexpensive option, does not require concentrically aligned shafts and requires minimal maintenance.
- Split-shaft drive – The motor is mounted below, and is independent from, the fan bridge. A shaft coupler can be used to join the electric motor and fan shaft (which is attached to the fan bridge). This is not the most economical concept

as it requires multiple shaft bearing housings. The individual shafts require alignment relative to each other and with the bell mouth centre.

- Geared design – The electric motor can be mounted horizontally on the MSACC platform and the output shaft will be directed downwards into the bell mouth using a bevel gearbox. The advantage of this concept is that it is possible to alter the speed and torque of the motor through the gearbox. However, the high manufacturing cost of the gearbox should be considered.
- Direct drive - This arrangement has a direct connection between the motor and the fan without any reduction. The motor can be mounted on the fan bridge.

The split-shaft drive design was selected, to make use of the available re-conditioned motor, which was deemed too heavy to be installed on the bridge in a direct-drive system. The split-shaft was also required in order to mount the torque transducer, to measure the applied torque and to calculate the fan power. The motor was installed in a vertical position, in a specially designed motor stand. The split shaft arrangement required a fan bearing housing to be designed and installed underneath the fan bridge. The fan bearing housing accommodates the fan bearings and a mechanism for the vertical displacement of the two shafts to accommodate changing of the fan rotor.

4.4. Technical Review of the MSACC Design

The following sub-section describes the technical review of individual components that were designed for the MSACC. The complete assembled model of the entire MSACC is depicted in Figure 4-3. The sub-assemblies that constitute the MSACC are the A-frame support structure (seen in navy blue), bell mouth (light blue), electric motor stand (red), fan bearing housing (within the A-frame) and A-frame plenum:

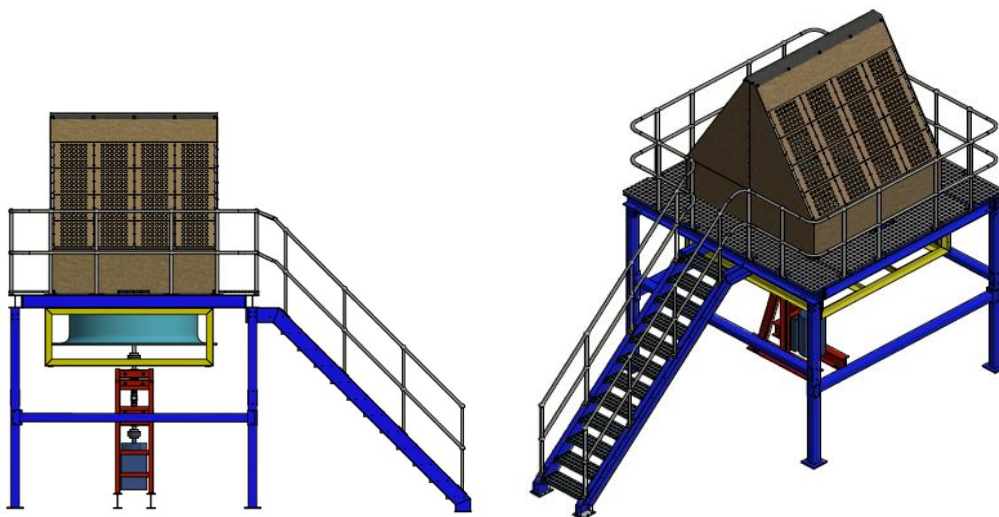


Figure 4-3: MSACC assembled 3D rendering

4.4.1. Support structure, platform and A-frame structure floor

The MSACC structure exceeded 2 m in height to accommodate the bell mouth and designated laboratory space, which required safety hand railings be mounted around the structure and stanchions according to the South African Bureau of Standards (SANS 10400-M, SANS10160-2). The steel floor, that attaches the bell mouth to the structure, was designed in eight sections with flanges. The purpose of the flanges is to increase rigidity, reducing the required thickness of the steel floor, and is used to bolt the individual sections together. A 500 mm wide steel walkway grid around the plenum was designed to serve as access to the heat exchanger of the A-frame. A staircase that conforms to the safety standard was incorporated into the design to provide access to the structure. The support structure and platform sub-assembly is shown in Appendix A. The support structure of the MSACC is depicted in Figure 4-4 below:

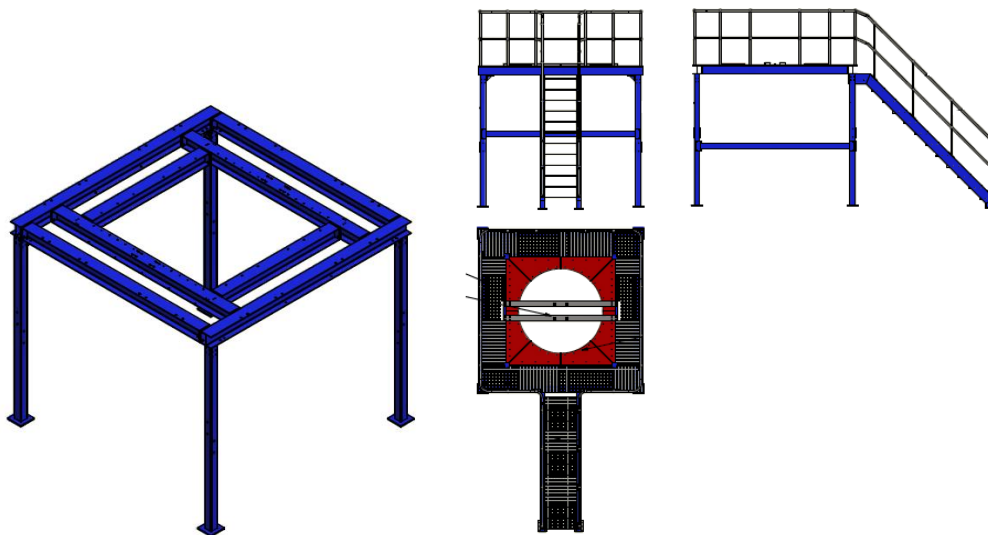


Figure 4-4: MSACC Structure (Left) with floor, walkway grid and railing (Right)

4.4.2. The bell mouth

The bell mouth design was required to accommodate the existing B2-fan. To compare to the B2-fan's performance in the BS 848 test facility, the MSACC's bell mouth geometry had to be identical to that of the test facility to provide similar inlet conditions. (A mould of the existing BS 848 test facility's bell mouth was made and used to produce the new bell mouth.) The bell mouth has a height of 700 mm and inner diameter of 1.542 m. The minimum height of the bell mouth measured from the floor is equal to the diameter of the axial flow fan, to allow adequate inlet airflow. This resulted in a design platform height of 2.4 meters. For this height, which exceeds 2 meters, the South African Bureau of Standards (SANS 10400-M, SANS10160-2) require that safety hand railings be mounted around the structure. It has a split design for ease of transportation and installation. Stiffening flanges

were built into the design to reduce the weight and improve rigidity and mounting flanges were incorporated behind the bell mouth to provide an area where it could be secured to the steel floor. Furthermore, due to the high velocity of the moving components, safety screens were designed to be fitted around the bell mouth and electric motor stand.

4.4.3. Electric motor and stand

An electric motor was obtained from the Department of Mechanical and Mechatronic Engineering. In order to use the electric motor as per design, the bearings had to be changed to allow the motor to operate vertically rated instead of in its original horizontally designed position. The electric motor's power was greater than the fan power required to run the fan and the device is also inefficient compared to modern lightweight electrical motors. The required power for the fan was between 5.3-5.7 kW. For the selected operating range, the electric motor is rated at 15 kW and maximum speed of 965 rpm. The electric motor stand design is shown below:

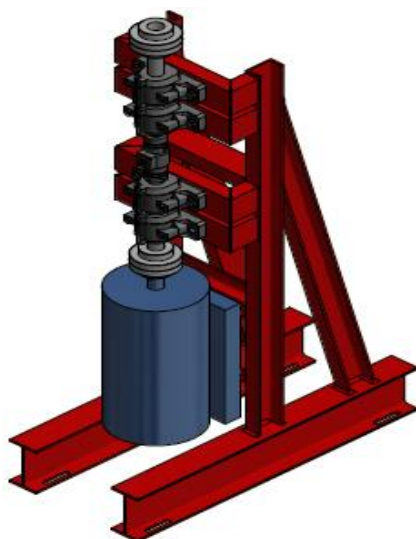


Figure 4-5: Electric motor stand 3D model

4.4.4. Fan bearing housing and fan bridge

The fan bearing housing was designed to house the bearings that support the fan shaft and is mounted on the fan bridge. Angular contact bearings were used and arranged back to back to support the weight of the fan shaft and the fan. The central housing contained the bearings and fan shaft. It ensured the alignment of the fan shaft and the transfer of the weight to the vertical housings that flank the bearing housing. An illustration of the final fan bearing housing design is provided in Figure 4-6 below:

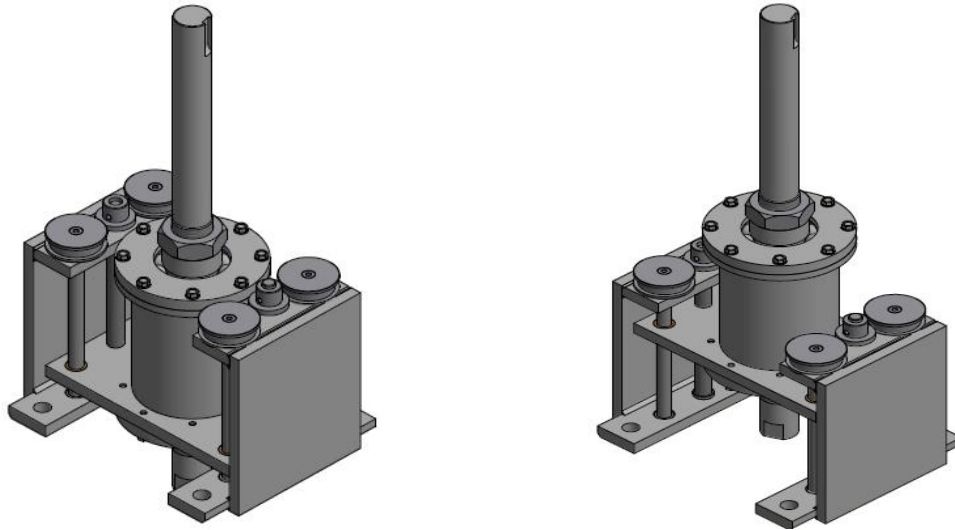


Figure 4-6: Fan bearing housing 3D model at the two positions (without the chain drive)

In addition, the fan bearing housing is designed to allow the separation of the fan shaft from the electric motor stand's end shaft. The two positions of the fan bearing housing facilitated removal and replacement of test fans. As portrayed in Figure 4-6, the central housing can move linearly up and down to allow the removal and replacement of the axial fan. The two outboard mounting flanges have smooth rods that guide the bearing housing linearly. The linear movement is facilitated by two power screws to lift and lower the central fan bearing housing. Brass bushings hold the power screws to the load bearing flanges and provide a journal bearing for the power screws. Smooth rods with brass bushings flank both sides of the two power screws to ensure that the bearing housing operates linearly. The two power screws are kept synchronised with a chain driven system. The chain and power screw setup was used for the removal and replacement of the axial flow fan, when required.

4.4.5. A-frame plenum

The A-frame plenum was designed and built on a scale of 1:6, equivalent to a full-scale ACC that can accommodate an axial fan of 9 meters in diameter. At the top of the legs of the structure, brackets were attached through which the A-frame could be bolted to the platform, providing a convenient method for assembling and replacing the A-frame. Square tubing was used to produce a steel frame on which the air resistance devices could be mounted. These devices were made of air guide fins and perforated plates, to direct and throttle the airflow. These two items resembled the fins and tubes of the condenser's heat exchanger by directing and throttling the airflow, respectively. The design of the A-frame plenum is shown in Figure 4-7, below.

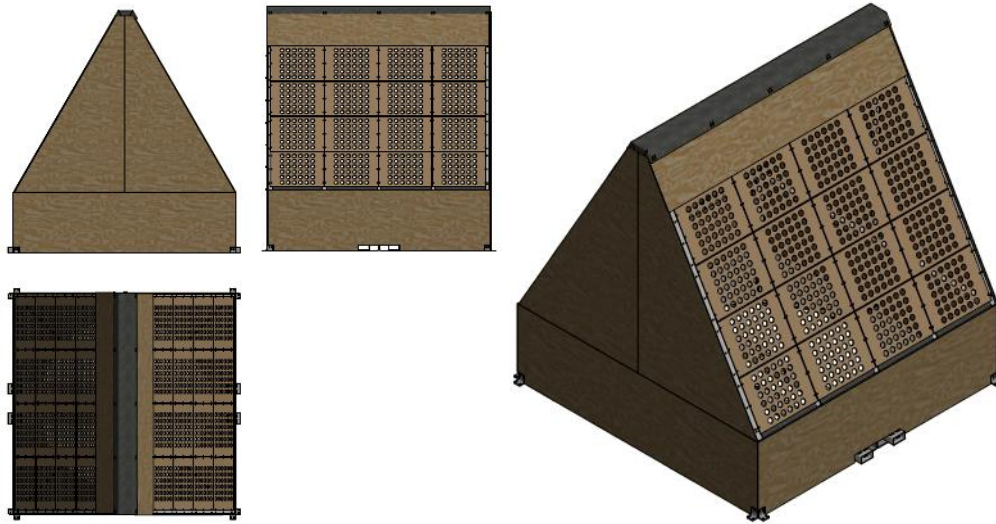


Figure 4-7: ACC plenum design with perforated plates isometric 3D drawing

As shown in Figure 4-7, the box section located below the A-frame is 0.5 meters high. The purpose of this box section was to ease accessibility to the A-frame's heat exchanger and reduce the variations in airflow distribution across the heat exchanger. The increased height also provides space for future alterations such as mounting a lighter motor for a direct drive system, or fitting fan exit guide vanes and longer fins for the heat exchanger.

4.4.6. Perforated plate and guide fins

The duty point is set by throttling the airflow with the use of the perforated plates. The guide fins are there to direct the airflow and produce an inlet pressure loss. The perforated plates and fins unit is shown displayed in Figure 4-8. It is housed in a steel plate box section (called a heat exchanger box), which is given end flanges to prevent the fins from falling through the A-frame. The perforated plate acts as the lid of the heat exchanger box and with the aid of weather tape was used to hold the fins in position. Using calculations presented in Chapter 3, the dimensions of the perforated plate and fin design were determined mathematically and confirmed experimentally.

The design of the heat exchanger box unit, which housed the perforated plate and guide fins, is illustrated in Figure 4-8 below:

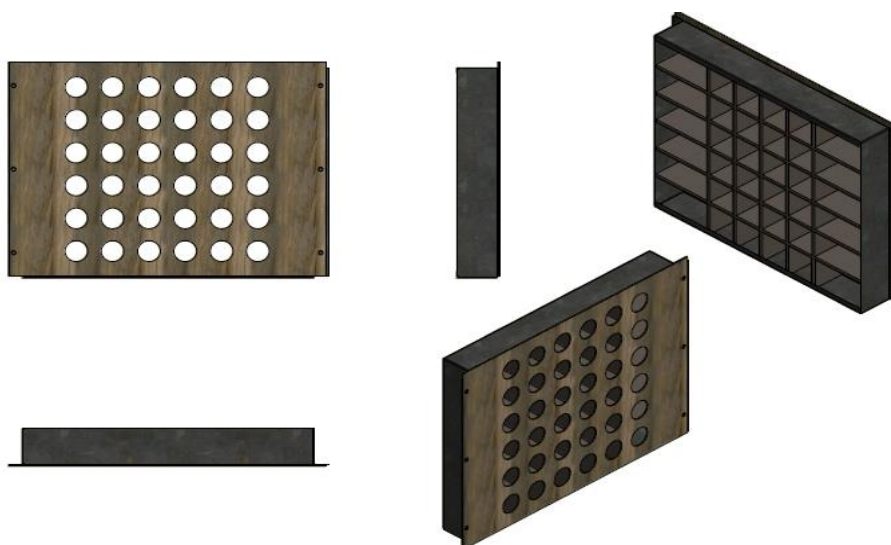


Figure 4-8: Heat exchanger box housing steel boxes, perforated plate and guide fins sub-assembly isometric drawing

4.4.7. Anemometer cross beam bracket

To provide a secure fixture for attaching the anemometers outside the A-frame downstream of the perforated plate, two cross beam brackets had to be designed. The design incorporated an adjustable height using a telescopic tube with a range of 750 mm from the perforated plate. This was to study the effects of anemometer distance from the perforated plates. The anemometer attachment points were designed to be adjustable for alignment with the perforated plates. Thus, the design made use of a retort and boss head clamps. The final built anemometer cross beam bracket is depicted in the final complete built MSACC instrumental setup in Figure 5-9.

4.5. Manufacturing, Construction and Assembly

4.5.1. Support structure

The support structure consists of the following components: the ladder sloped at 45 degrees, safety railings, I-beam platform, walking grid mesh and A-frame floor. The structure was constructed to be 3 x 3 meters wide and 5.2 meters high to fit into the allocated area. The support structure was attached to the building's floor by chemical bolts. L-brackets were constructed and used to join of the structural components.

4.5.2. Bell mouth

The bell mouth was mounted at the bottom of the A-frame steel floor. During the assembly phase, the two halves of the bell mouth were bolted together and the centre was determined using the circle-chord rule.

4.5.3. MSACC A-frame

The A-frame was constructed from square steel tube sections and bolted together using laser cut and CNC bent brackets. This frame was bolted onto the I-beam platform. The framework was dressed over with wooden panels and the heat exchanger boxes. The guide fins were placed in front of the perforated plate to direct the airflow. They were individually held in position with steel box sections as discussed in Chapter 4.4.6.

4.5.4. Plenum sealing

During the construction of the A-frame plenum, rubber-foam weather tape was used between the wooden boards and A-frame steel structure to provide an airtight seal. The volume in the plenum provided space to work within the A-frame. Furthermore, polyurethane expanding foam was used where it was impossible to provide an adequate seal with the weather tape. As the data in Chapter 5 indicates, there was minimal air leakage in the plenum.

4.5.5. Fan bearing housing

The fan bearing housing was constructed in stages with the outboard mounting flanges constructed first; thereafter, the bearing housing, followed by the fan shaft. The bearings and brass bushing of the housing's linear lifting system were press fitted using a hydraulic press. The bearings permitted the axial load to be transferred from the fan shaft to the housing itself.

The four pulleys were made from Vesconite, to withstand the wear of the chain rubbing against it. Two flanges were constructed on both sides of the pulley to keep the chain from disengaging from the sprocket. The entire pulley was machined to the exact dimensions to keep the chain tension. A sprocket was mounted on the power screws using a grub screw locked at the side of the sprocket. Grub screws were used to prevent the smooth rod from sliding out of the brass bushing, when lifting and lowering the bearing housing. A M17 nut was welded to both sprockets in order to attach a ratchet tool to manually drive the chain system. To make assembly easier, the chain was fitted with a half link, which allowed for the splitting of the chain loop in one chain length piece. After assembly, the entire chain system, power screw and guide rods were lubricated with a copper-slip component to ensure frictionless operation.

4.5.6. Electric motor stand

The four Plummer blocks, with the greased bearings and two shafts situated between the electric motor and the fan, were installed on the motor stand. Using a crane, the electric motor was positioned onto the electric motor stand, which was then fixed to the building floor underneath the centre of the bell mouth using chemical bolts. Thereafter, the two spider-flex shaft couplers and torque transducer with its shaft couplers were installed.

At the final assembly stage, shaft alignment was achieved using a dial gauge, a three-axis level and an electronic angle measurement tool. Final assembly was performed in three stages: Firstly, the electric motor stand and its three shafts were aligned. Then the bell mouth and fan bearing housing was aligned and thereafter, the fan bearing housing and the electric motor stand were aligned.

4.5.7. Variable speed drive and safety screen

The no-load operational speed of the allocated GEC-Alsthom 3-phase 6-pole motor is rated to be 965 rpm. A variable speed drive (VSD) was required to reduce the speed of the electrical motor to the fan's optimal working speed of 750 rpm. The VSD controls and governs the electric motor's output torque and speed, by varying the motor's input frequency and voltage.

The selected 15 kW 32 Ampere Varispeed VSD is in a mild steel enclosure. It houses the display unit, potentiometer, control circuit board and emergency switches. An in-line filter was also specified in the VSD to reduce the input power fluctuations to the electric motor; thus, it was possible to achieve a steady motor speed during experiments. All cables to and from the power socket, VSD and electric motor were installed. A photograph of the VSD and its housing is provided below in Figure 4-9:



Figure 4-9: Varispeed 15 kW variable speed drive (left) and the safety screen (right)

The two safety screens fixtures (painted yellow) were manufactured and installed around the electric motor stand and the bell mouth. They provided a safeguard against accessing the components of the electric motor stand and the fan during its operation. The safety screen around the bell mouth ensured the mesh would intercept the individual pieces that in case of fan blade failure.

4.5.8. MSACC B2 axial flow fan installation

To ensure that the blade setting angle of the B2-fan blades corresponded to that of the test results obtained from the fan test facility, the blade setting angle was measured. Using a measurement table, the B2-fan angle setting tool and electronic angle measurement tool, each blade's angle was adjusted to 31 degrees as shown in Figure 4-10, below. Finally, the B2-fan was installed on the fan bearing housing shaft with a taper lock bush.

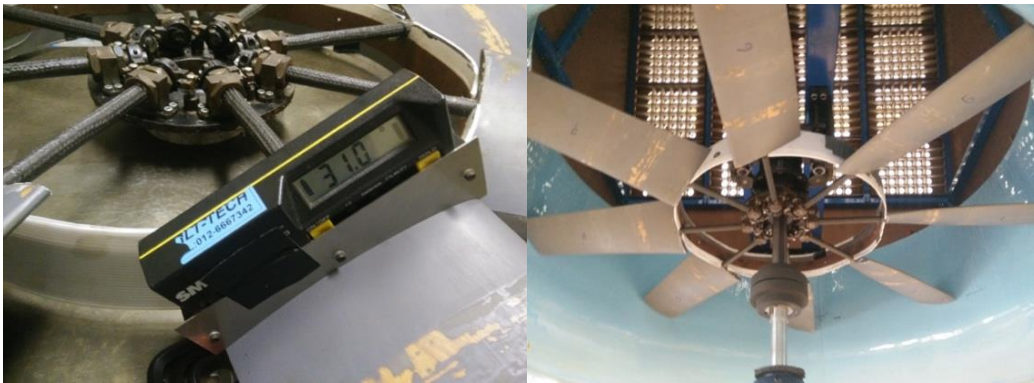


Figure 4-10: Blade setting angle procedure (left) and B2-fan in the installed position without the hub cover (right)

Before the fan installation in the bell mouth, the fan bearing housing was aligned with the bell mouth and the fan tip clearance was set with the fan mounted in position. Thereafter, a dial-gauge and a three-axis laser level was used to align all three shafts and the electric motor. Figure 4-11 shows the B2-fan axial position in the bell mouth and tip clearance. The figure also portrays the bell mouth casing and height dimensions. This is the same conditions that were used for the fan performance experiments.

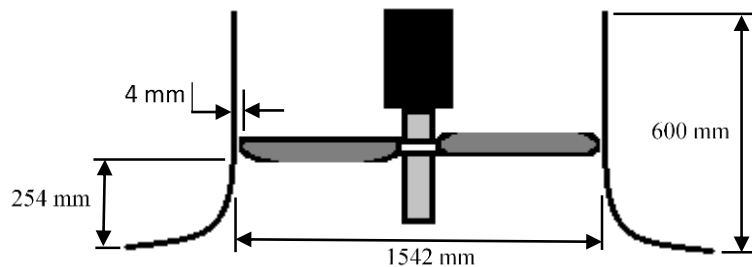


Figure 4-11: MSACC B2-fan in installed position and dimensions

5. INSTRUMENTATION CALIBRATION, MSACC TEST SETUP AND MSACC TESTING PROCEDURE

5.1. Introduction

This chapter underlines the test instrumentation calibration, pre-tests, data capturing software and test procedure executed on the MSACC to determine the performance of the B2-fan. Each component was calibrated in a laboratory before commissioning to confirm the measurement system's capabilities and functionality. The calibration tests were performed to eliminate possible malfunctions and provide an opportunity for the researcher to familiarise himself with the system. This ensured the reliability and validity of measurements obtained from the instruments.

5.2. Measurement Equipment

Various types of instrumentation were used in the induced draft wind tunnel, anemometer distance test setup and MSACC test facilities. The induced wind tunnel instrumentation used during anemometer calibration and perforated and guide fins tests are as follows:

1. Three HBM PD1 inductive differential pressure transducers.
2. Pitot static tube (static and dynamic pressure of air stream).
3. Mercury barometer to measure atmospheric pressure.
4. Mercury thermometer to measure the dry- and wet- bulb air temperature.

The forced wind tunnel and MSACC instrumentation used during the testing are listed below:

1. HBM T22 200 Torque transducer.
2. Five AutoTran differential pressure transducers.
3. Twelve/fourteen anemometers to measure the air speed at the inlet and outlet. Test1 (750 rpm) used four anemometer and test 2 (750 rpm and 660 rpm) used six anemometers in front of the fan inside the bell mouth and four anemometers on each side of the A-frame.
4. Laser tachometer.
5. Mercury barometer to measure atmospheric pressure.
6. Mercury thermometer to measure the dry- and wet- bulb air temperature.

Forced wind tunnel anemometer and perforated plate calibration test made use of the following instrumentation:

1. Two AutoTran pressure transducers.
2. A single Anemometer (Anemometer J)
3. Mercury barometer to measure atmospheric pressure.
4. Mercury thermometer to measure the dry- and wet- bulb air temperature

Although *CATMAN* contains pre-set sensor calibration data it was still necessary to calibrate all sensors used in the test setup. Calibration of the pressure and torque was carried out before each set of tests to ensure accuracy and repeatability.

5.2.1. Torque transducer

The HBM T22-200 torque transducer and its couplings as illustrated in Figure 5-1 were used. Hence, it was required that the design be adapted to accommodate this torque transducer and couplings' dimensions.



Figure 5-1: HBM T22-200 torque transducer

The HBM T22 200 torque transducer was installed to measure the torque produced by the electric motor as previously shown in Chapter 4. It has a nominal rating of 200 Nm at 5 Volts. However, it was found that the power supplied by the QuantumX 1610B was insufficient to operate the transducer; thus, a separate 24V power supply was used. The torque transducer output signal is measured as a voltage source and has a sensitivity tolerance of 0.2% with an accuracy class of 0.5. It utilises contactless transmission to measure signals. Shaft couplings used were flexible and removed the cyclic loading on the torque transducer. (Hottinger Baldwin Messtechnik, 2016). The T22 200 torque transducer calibration setup is depicted in Figure 5-2.

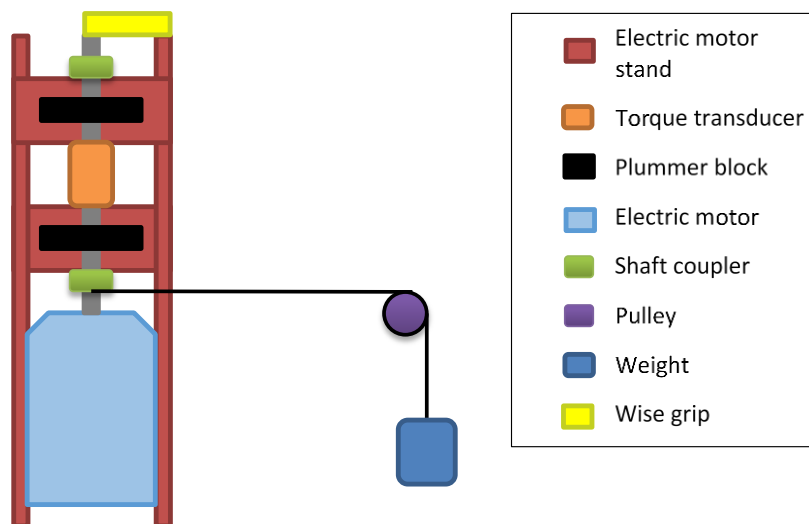


Figure 5-2: Torque transducer calibration setup

Typical results obtained during the calibration of the torque transducer are shown in Table 5-1. Before calibration of the torque transducer, the fan shaft and the electric motor shaft were disconnected by lifting the shaft couplers. The shaft coupler (which has a diameter of 150mm) of the electric motor was used as a moment arm to produce torque for calibration. The gravitational constant at the University of Stellenbosch is $9.808 \text{ m}^3/\text{s}$, and was used accordingly. A pulley system and weights were used to apply the torque and the shaft was clamped at the top with a “vice-grip”.

Table 5-1: Typical calibration test 1 values for HBM T22 200 torque transducer

Reading	Mass	Torque	Voltage
Units	[kg]	[Nm]	[V]
1	4.987	3.668	0.085
2	9.983	7.343	0.148
3	14.985	11.023	0.231
4	19.729	14.513	0.302
5	24.724	18.187	0.413
6	27.773	20.430	0.482
7	37.780	27.790	0.690
8	47.769	35.139	0.744
9	57.507	42.302	0.984
10	67.514	49.663	1.162
11	77.497	57.007	1.340
12	87.558	64.408	1.504
13	97.467	71.697	1.663

The tabulated results are displayed graphically in Figure 5-3 below.

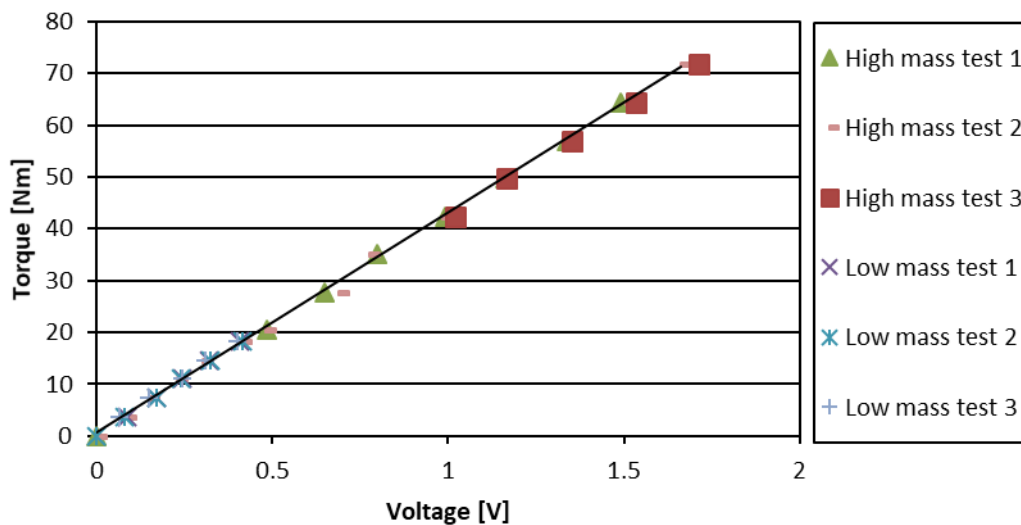


Figure 5-3: Data and trend line for the torque transducer

The Figure 5-3 illustrates the values of all the torque transducer's calibration tests. It shows the linear relationship between the torque and voltage for the T22 200 torque transducer. The figure shows a linear relationship between voltage and the applied torque. Using a trend-line, an average linear relationship between torque and voltage for all the tests is described by the following equation:

$$T = (\text{Slope} \cdot V) + \text{intercept} \quad (5.1)$$

V is the voltage reading of the instrument. For the calibrated torque transducer, the slope and intercept is 42.470 and 0.650 respectively.

5.2.2. Propeller anemometer calibration

Thirteen Young Model 27106 propeller anemometers were used to measure the airflow velocity at inlet and outlet positions of the MSACC. Van Aarde & Kröger, (1993), Muiyser (2012) and Zapke (1997) likewise made use of propeller anemometers to measure the inlet and exit air velocity of an ACC unit. The propeller-type anemometer consists of a propeller attached to a tachogenerator that generates a voltage output based on the rotational speed of the propeller. The inlet position was installed beneath the B2-fan in the MSACC's bell mouth; the outlet position is located at the centre of the perforated plates, using the cross-beam member on the A-frame. The Young Model 27106T is shown Figure 5-4.

Muiyser (2012) proved that the propeller anemometers measure the airflow that is parallel to their axis; thus, it was not necessary to calibrate the anemometers with respect to the airflow angle. Calibration of all anemometers was necessary to

establish that the voltage to air speed follows a linear relationship. The test setup of the anemometers in the induced wind tunnel is shown in Figure 5-4 below:

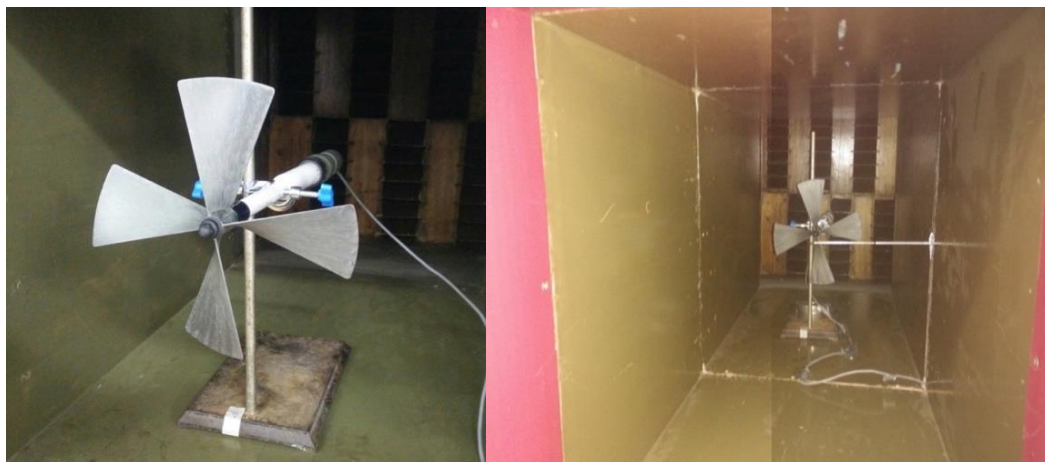


Figure 5-4: Young model 27106T propeller anemometer (Left) and Anemometer calibration with pitot tube test setup in induced wind tunnel (Right)

The pitot tube was used to measure total and static pressure of the air stream to determine the true air velocity in front of the anemometer (as shown by right-side image in Figure 5-4). It was placed 100 mm directly in front of the anemometer's propeller shaft. The calibration curves for all the anemometers were calculated by using the air property calculations as given in Appendix C for the induced wind tunnel and the voltage readings as given in Table 5-2. Two calibration tests were conducted for all anemometers. Two types of anemometer propellers were used: expanded polystyrene and carbon fibre propeller. The expanded foam propeller is denoted by anemometers G, H and N in the table below. The anemometer voltage results of the first calibration test are given in the table below:

Table 5-2: Anemometer typical voltage readings for test

Data point/ anemometer	Unit	Point 4	Point 5	Point 6	Point 7	Point 8	Point 9	Point 10
Motor speed	Hz	20	25	30	40	35	45	49
A	V	0.133	0.184	0.233	0.281	0.327	0.375	0.418
B	V	0.139	0.188	0.237	0.285	0.338	0.385	0.434
C	V	0.135	0.183	0.231	0.281	0.334	0.380	0.428
D	V	0.141	0.189	0.235	0.277	0.328	0.377	0.426
E	V	0.138	0.185	0.230	0.279	0.330	0.374	0.424
F	V	0.140	0.194	0.264	0.262	0.339	0.385	0.430
G	V	0.143	0.184	0.233	0.285	0.327	0.380	0.438
H	V	0.140	0.189	0.240	0.288	0.335	0.399	0.427
I	V	0.138	0.186	0.226	0.281	0.331	0.375	0.416

J	V	0.144	0.193	0.235	0.285	0.331	0.385	0.433
K	V	0.159	0.209	0.277	0.322	0.380	0.443	0.501
L	V	0.159	0.209	0.277	0.322	0.380	0.443	0.501
M	V	0.159	0.210	0.276	0.338	0.395	0.457	0.512
N	V	0.136	0.196	0.251	0.315	0.383	0.432	0.499

The table below shows the induced wind tunnel and pitot tubes test results, with the included air properties.

Table 5-3: Wind tunnel typical test result of the anemometer calibration

Data point	T_w	T_d	P_{atm}	Specific humidity (ω_1)	Pitot tube Δp_d	Air density ρ_a	Air volumetric flow rate	Pitot tube Air velocity V_a
Unit	[°C]	[°C]	[kPa]	$\left[\frac{\text{kg H}_2\text{O}}{\text{kg dry air}} \right]$	[Pa]	$\left[\frac{\text{kg}}{\text{m}^3} \right]$	[m ³ /s]	[m/s]
4	20	26	1002.200	0.013	6.258	1.143	3.228	3.309
5	20	26	1002.200	0.013	9.824	1.143	4.055	4.145
6	20	26	1002.200	0.013	14.314	1.143	4.869	5.004
7	20	26	1002.200	0.013	19.490	1.143	5.623	5.839
8	20	26	1002.200	0.013	25.552	1.143	6.453	6.685
9	20	26	1002.200	0.013	32.410	1.143	7.274	7.529
10	20	26	1002.200	0.013	38.293	1.143	7.930	8.184

Using the pitot tube's average velocity readings and dividing these by the anemometer's RMS voltage output for three different speeds of the wind tunnel's electric motor, the calibration relationship can be determined. The relationship of the output voltage and air speed as given by the OEM is portrayed by Equation (5.2):

$$V_m = A_c V_{an} \text{ [m/s]} \quad (5.2)$$

In the Equation (5.2), V_m is the air flow velocity measured in m/s, V_{an} is the anemometer output voltage in mV and the "calibration constrain" is given by term A_c . The OEM calibration constant is given as 0.018. The sixteen anemometers' calibration value and percentage error from the OEM's calibration value are recorded in Table 5-4 below:

Table 5-4: Voltage vs air speed readings of the anemometer calibration

Anemometer	Test 1 Slope	Test 2 Slope	Test reading Difference	Average	OEM error
Unit	[m/s / V]	[m/s / V]	[-]	[m/s / V]	[-]
A	17.871	17.821	0.050	17.846	0.855%
B	17.270	17.271	0.000	17.270	4.053%
C	17.579	17.578	0.001	17.579	2.340%
D	17.501	17.502	0.001	17.502	2.769%
E	17.645	17.645	0.000	17.645	1.973%
F	17.603	17.588	0.015	17.596	2.246%
G	17.645	17.645	0.000	17.645	0.027%
H	17.106	17.106	0.000	17.106	3.026%
I	18.164	18.165	0.001	18.164	-0.913%
J	16.810	16.756	0.054	16.783	6.762%
K	15.303	15.303	0.000	15.303	-
L	15.778	15.778	0.000	15.778	-
M	14.890	14.889	0.001	14.890	-
N	16.043	16.042	0.000	16.043	-

Due to the variances between the anemometers, the individual calibration constants were used during the Pre-tests and MSACC tests.

5.2.3. Laser Tachometer, barometer and thermometer

The rotational speed of the fan was measured using a laser tachometer positioned adjacent to the fan shaft. The laser tachometer used to measure the fan speed is shown in Figure 5-5 (left). The tachometer was set to measure the speed of the shaft of the MSACC's electric motor in rpm. An aluminium reflective adhesive tape was placed on the shaft to provide a reflective surface for the laser to measure the rotational speed (tachometer measures the amount of reflections for a given time frame). For every test run, the speed of the shaft was measured. The tachometer was calibrated and certified by an accredited institution.



Figure 5-5: Laser tachometer (left), mercury barometer (middle) and wet- and dry-bulb mercury thermometer (right)

A mercury barometer and wet- and dry-bulb mercury thermometer (shown in the figure above - middle and right respectively) were used to measure the ambient air conditions at both test facilities. The barometer was accurate to 0.005 mmHg and thermometer was accurate to 0.5 °C. From the reading of these instruments, the specific weight of water vapour in the air and air density can be calculated. The calculations are given in Appendix C.

5.2.4. Pressure transducers

Two sets of pressure transducers were used, as displayed in Figure 5-6: The four HBM PD1 inductive differential pressure transducers were used at the induced draft wind tunnel and five AutoTran pressure differential transducers were used at the MSACC and the forced wind tunnel setups. The pressure transducers each had two pressure reading ports (positive and negative pressure). Thus, it was possible to take a differential reading. Both types are inductive differential transducers with a range of ± 900 Pa. The calibration data for the inductive differential transducers has been discussed in Appendix C, after the induced wind tunnel layout and calculations.



Figure 5-6: HBM PD1 (left) and one AutoTran pressure transducer (right)

Before each of the pressure transducer calibration tests, a leakage test was executed on the pressure tubes that are connected to the transducers to ensure an accurate pressure reading. Multiple calibrations were performed at different time periods yielding almost no difference in the calibration curves.

5.2.5. MSACC AutoTran pressure transducer calibration

The five AutoTran pressure transducers were secured to a stainless-steel box and were kept in the data collecting station at the MSACC setup. The pressure transducer calibration setup is displayed below in Figure 5-7:

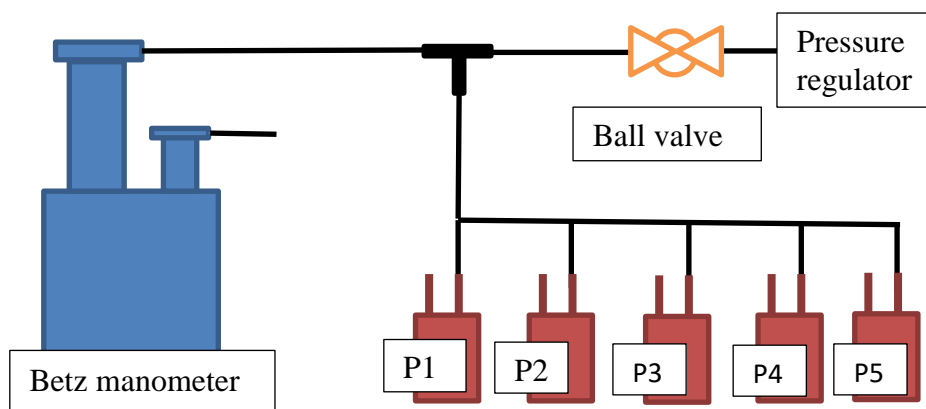


Figure 5-7: Pressure transducer calibration setup

The Betz manometer used for both calibration test displayed its readings in Pascal. The voltage readings of the five pressure transducers was recorded for each pressure point. The table below shows the results of the readings of the manometer and the transducers.

Table 5-5: Pressure transducer calibration reading (Calibration test 1)

Reading	Betz Manometer reading	Pressure transducer 1	Pressure Reading 2	Pressure Reading 3	Pressure Reading 4	Pressure Reading 5
Units	[Pa]	[V]	[V]	[V]	[V]	[V]
1	0	0	0	0	0	0
2	24	0.204374	0.206589	0.209501	0.203462	0.201346
3	51	0.436563	0.442739	0.442976	0.435867	0.432008
4	94	0.811152	0.823341	0.816308	0.811048	0.804803
5	154	1.328407	1.348636	1.333227	1.330551	1.320187

6	194	1.693961	1.717153	1.697244	1.695993	1.683271
7	237	2.074535	2.10076	2.073397	2.077676	2.063128
8	298	2.619725	2.653003	2.620459	2.628487	2.607696
9	386	3.412669	3.454294	3.410813	3.427234	3.400325
10	447	3.960561	4.009439	3.961488	3.980479	3.948983
11	609.3	5.439798	5.502928	5.441383	5.472791	5.432145
12	680	6.06676	6.13734	6.071462	6.106785	6.061234
13	744	6.644256	6.711761	6.650647	6.689714	6.63921

The average results of the three calibration tests is shown graphically in Figure 5-8:

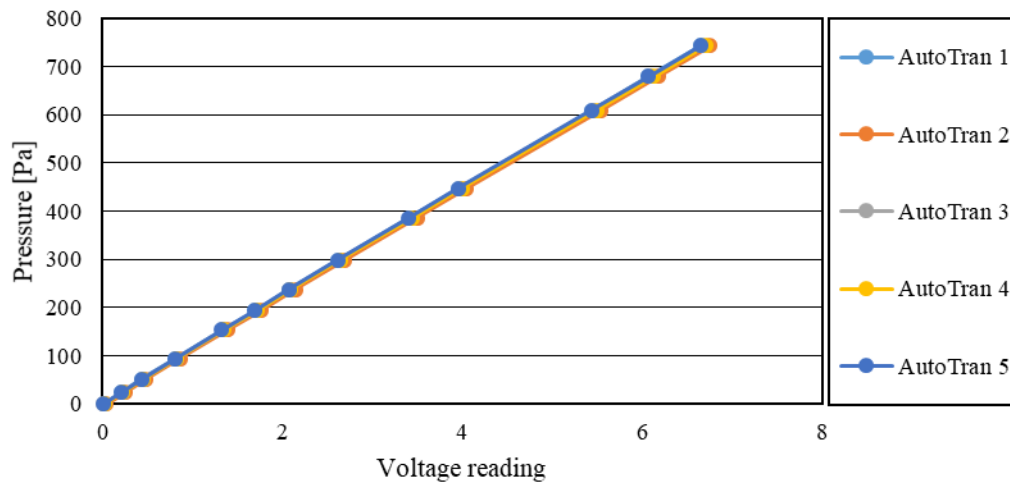


Figure 5-8: AutoTran Pressure Calibration Curve

The figure depicts a linear relationship between the voltage reading and pressure applied to the transducer, which indicates a linear relationship between and is described by Equation (5.1) and the table below:

Table 5-6: AutoTran pressure transducer calibration constants

AutoTran transducer /Calibration constants	AT1	AT2	AT3	AT4	AT5
Intercept	4.532	3.885	4.073	5.010	5.138
Slope	111.209	109.938	111.324	110.498	111.366

5.3. MSACC Test Setup

The instrument setup and placement of the static pressure measurement placement of the MSACC is depicted in Figure 5-9 below. The pressure points were not measure across the A-frame, but rather at the static pressure taps were employed on the front wall of the A-frame as seen in Figure 4-2.

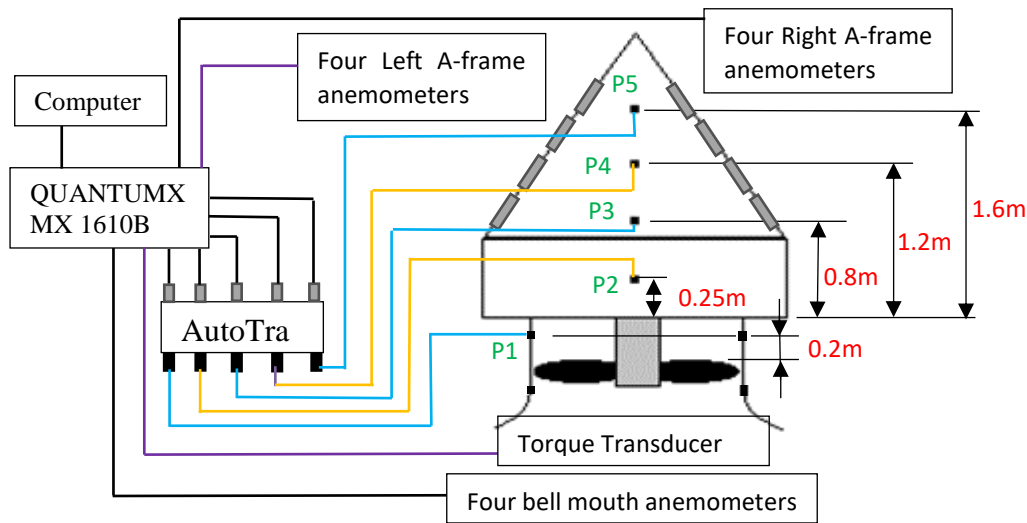


Figure 5-9: The instrument setup for the MSACC

The test setup made use of the following equipment:

- Data logging computer.
- HBM QuantumX 1610B.
- Five AutoTra pressure transducers.
- Fourteen anemometers (Four (test 1) or six (test 2) in the bell mouth, four on the right side and four on left side of the A-frame).
- One HBM T22-200 torque transducer.

5.3.1. Data logging equipment

A QuantumX MX1610B shown in Figure 5-10 (left side) was used to record voltage readings of the instrumentation used. Of the 16 channels of the HBM QuantumX 1610B, fourteen channels were allocated for the anemometers, one for the torque transducer and one for the pressure transducer (measuring P1 – fan static pressure). Four pressure taps were drilled and glued around the bell mouth's circumference (200 mm downstream of from the fan's centre plane). As indicated in the figure, four static pressure points (P2-P5) was selected to measure the static variation inside the plenum. For the A-frame plenum pressure tests the A-frame's right-side (eastern-side) anemometers were replaced with the other four pressure transducers. All wiring was shielded to reduced external interference. The pressure tubes leading from the MSACC pressure points were connected to the AutoTra Pressure transducers.



Figure 5-10: HBM MX1601B universal amplifier (Hottinger Baldwin Messtechnik, 2016) (Left) and data logging equipment measuring box

The safety procedures of the laboratory require that all exit doors be kept open in the event of a fire, which necessitated that a measuring box to be used to house the computer and data logging equipment. Safety screen around rotating equipment was required by laboratory safety standard. All wiring and static pressure tubes were directed into the measurement box and connected to the transducers and data logging equipment. The equipment was commissioned and tested for compatibility to ensure communication between the hardware and software.

The manufacturer's recommended software for the HBM Quantum MX1610B to measure and record the data is CATMAN Easy, which is the interface between the computer and the data logger. The MX1501B's channels is electrically isolated and can be read as either voltage or current. Furthermore, each channel's measuring frequency and filter can be set separately. To eliminate channel measurement characteristic influences, the same channel was used for the calibration and the tests.

All channels are initialised before readings were taken. The CATMAN™ Easy software provides a real-time output for all channels, which are presented graphically. The graphics provide a convenient indicator to ascertain whether the system has reached a steady state condition at a given operating point. All data were recorded and stored in real-time and the voltage-time reading was taken and postprocessing calculations were performed using a written MATLAB™ code and Microsoft Excel™ spreadsheets.

5.3.2. Instrumentation installation

The inlet anemometers were installed with steel rods and retort clamps in the MSACC bell mouth entrance using the yellow safety screen as a mounting platform. This arrangement is displayed in Figure 5-11 (Left), below. The safety screens are permanently kept on during all tests.

The two cross beam brackets were manufactured according to the design specifications and installed on either side of the A-frame. The eight anemometers

were fixed to the two cross beam brackets with the retort and boss head clamps. The distances for the anemometer and the perforate plates were determined in the wind tunnel; the results are shown in Chapter 5.4.3. The distance test data indicated that the optimum position of each anemometer is to be set at 200 mm from the centre of the perforated plates. The anemometers and the cross-beam brackets are displayed in Figure 5-11 (Right).



Figure 5-11: Safety screens (painted yellow) with bell mouth anemometers (Left) and cross beam member with four anemometers mounted across the A-frame's perforated plates(Right)

5.4. Pre-tests

Three tests were conducted to establish the geometry of the heat exchanger model (guide fins and perforated plate) of the MSACC. All results and sample calculations are shown in Appendix B. The number of fins and of holes in the perforated plate presented a manufacturing and assembly challenge. Thus, a pre-test was required to determine the most effective and viable option.

5.4.1. Determining of the porosity of the perforated plate

In the book of Kröger (1998), in example 8.1.3, the loss coefficient for a specific finned tube heat exchanger is given as:

$$K_{he} = 4177.08481 Ry^{-0,4392383} \quad (5.3)$$

Where Ry is called the characteristic flow parameter and is defined as:

$$Ry = m_a / (\mu_a * n_b * A_{fr} * (n_{tb1} / n_{tb2})) \quad (5.4)$$

The air-cooled condenser used in example 8.1.3 in Kröger (1998) made use of the following parameters and conditions:

Table 5-7: Example 8.1.3 parameters

T	μ_a	A_{fr}	n_b	n_{b1}	n_{b2}
[K]	[mPa]	[m²]	[-]	[-]	[-]
304.886	1.869E-05	27.55	8	57	58

The pressure loss coefficient calculation for of the heat exchanger resulted in a value of $K_{he} = 22.2882$ and a total heat exchanger loss coefficient of $K_{\theta t} = 35.2920$. The total heat exchanger loss coefficient takes in account the inlet and exit pressure coefficients. This pressure loss value will satisfy the equations. Using the draft equation and calculations as given in Appendix B, Figure 5-12 indicates the predicted operational curve of the B2-fan in MSACC with $K_{\theta t} = 35.2920$. The figure also shows the BS848 experimental B2-fan curves. The intersecting points of the predicted operational curve equation and the static pressure curves is the operating points of the MSACC.

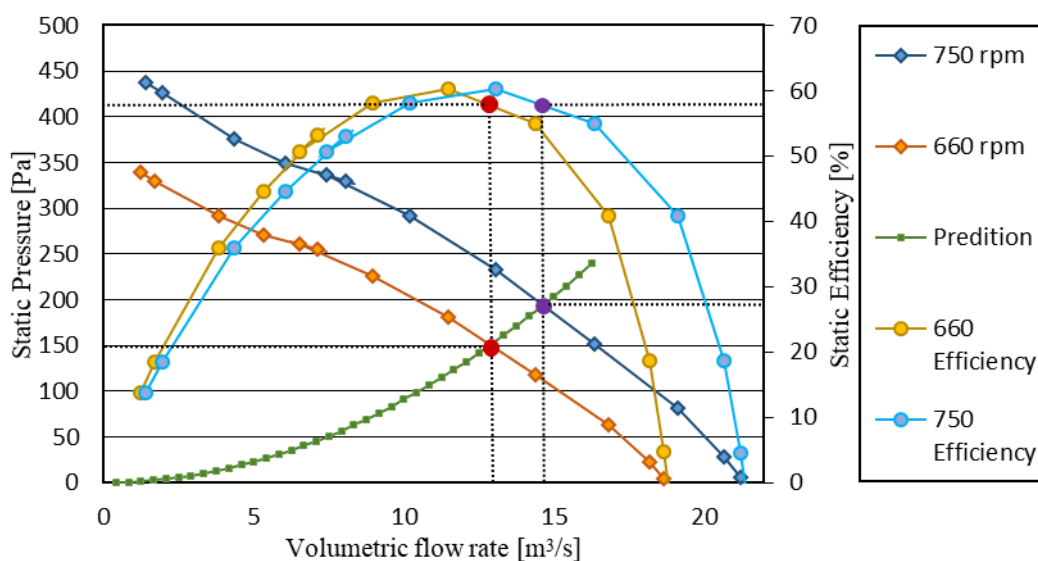


Figure 5-12: MSACC operation point - Pressure loss prediction ($K_{he} = 22.2882$ and $K_{\theta t} = 35.2920$)

5.4.2. Perforated plate porosity test

The static pressure drop vs volumetric flow rate test determined the impact of porosity on the loss coefficient of the perforated plates. Using a perforated plate with varying hole quantities were tested to determine the perforated plate porosity and guide fins combination achieve close to the pressure loss coefficient of 22.288.

The figure below shows six samples of perforated plates tested to determine the perforated plate to pressure loss characteristics.

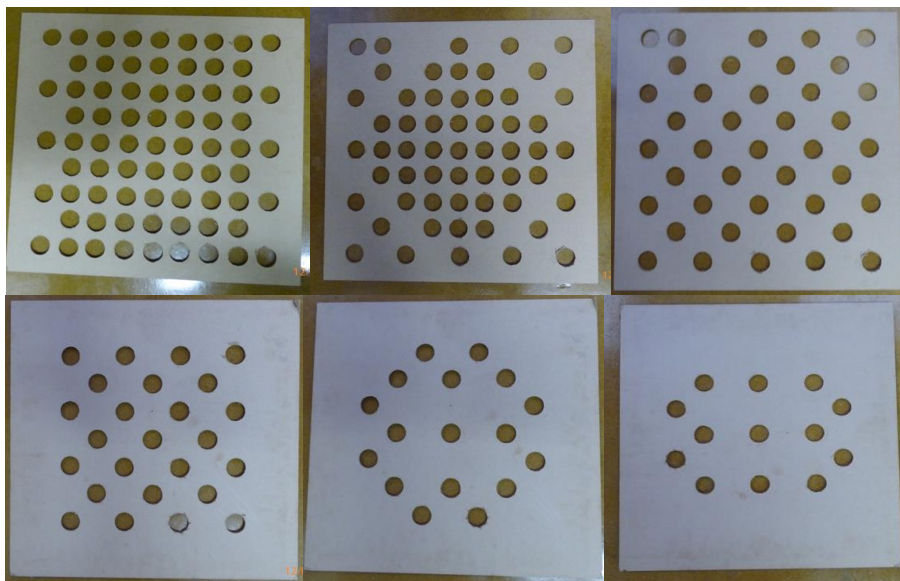


Figure 5-13: Perforated test plate with varying holes 73, 57, 41, 25, 17, 13 (From left to right and top to bottom)

The pressure coefficient of test perforate plates was calculated by using equation (2.1). The average velocity through the perforate was determined by dividing the measured volumetric flow rate by the induced wind tunnel's test area (0.235 m^2). Each individual test conducted, made use of 11 data points to determine the pressure loss coefficients. Table 5-8 shows the average pressure loss coefficient for the tested perforated plates.

Table 5-8: Perforated test plate with varying holes' porosity and calculated pressure loss coefficient

Open holes	Open area	Porosity	Pressure loss coefficient
Units	[m²]	[-]	[-]
9	0.0087	3.680%	563.696
13	0.0125	5.320%	550.221
17	0.0164	6.960%	178.086
25	0.0241	10.240%	81.990
33	0.0317	13.510%	45.652
41	0.0394	16.790%	29.025
49	0.0471	20.060%	20.747
57	0.0548	23.340%	15.087
65	0.0625	26.610%	11.353
73	0.0702	29.890%	10.030

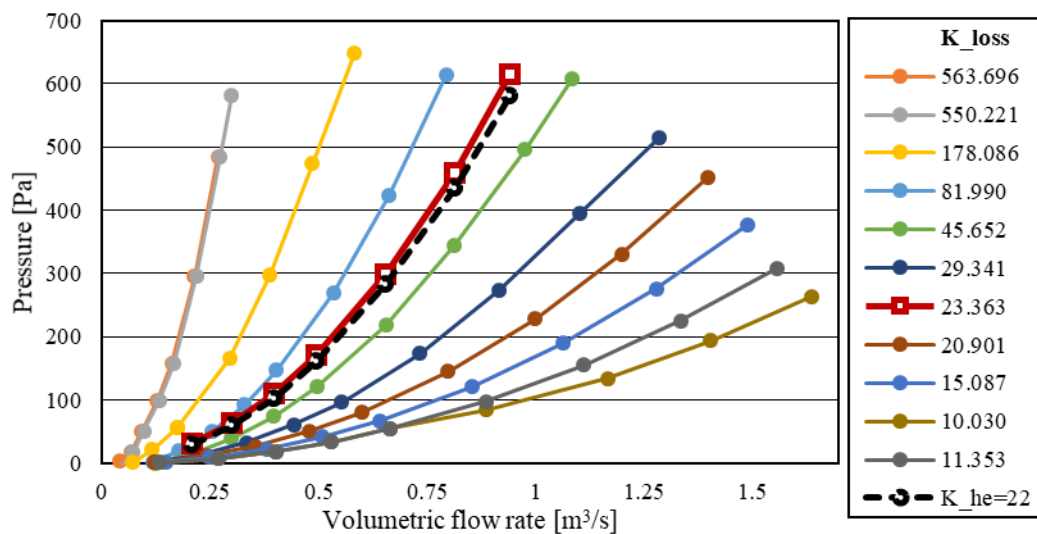


Figure 5-14: Static pressure vs volumetric flow rate for perforated test plates with different porosities.

The MSACC perforated plate that was eventually selected has a porosity of 23.992% as depicted in Figure 5-14, with a frontal area of $0.34 \times 0.43 \text{ m}$ and 36 holes with an average diameter of 34.7 mm . Choosing the 36-hole plate meant that guide fins of 5 rows and columns can be placed in front of the perforated plate to act as the fins of a heat exchanger.

To vary the operating point of the MSACC, holes of the perforated plate are closed off to increase the heat exchanger pressure loss coefficient. These typical throttle test results for selected perforated are given in Appendix C. Seven operating points were chosen, with four main operating points being: 100%, 83.3%, 66.6% and 50%, and three minor intermediate operating points of: 91.6%, 75% and 58.3%. The table below shows the calculated heat exchanger/finned-perforated plate pressure loss coefficients with the indicated open hole quantity.

Table 5-9: Chosen perforated plate throttle - pressure loss coefficient results

Parameters	Units							
Open holes	[-]	36	33	30	27	24	21	18
Throttle	[-]	100%	91.6%	83.3%	75%	66.6%	58.3%	50%
Open area	[m^2]	0.240	0.220	0.200	0.180	0.160	0.140	0.120
$\overline{K_{he}}$	[-]	23.478	28.494	36.402	46.3780	59.532	78.339	114.449

The perforated plate typical throttle test results are given graphically in the figure below:

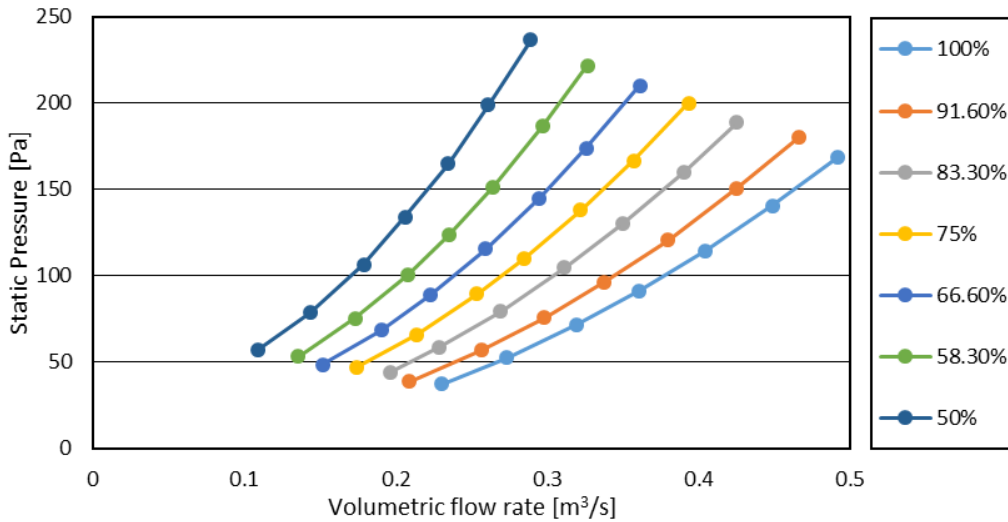


Figure 5-15: Chosen perforated plate throttle test results

Appendix D explains in detail the steps that were followed to predict the MSACC performance using the ACC draft equations. The following figure illustrates the prediction by using the above table’s heat exchanger pressure loss coefficient at the various throttle states in the draft equation to produce the following results below:

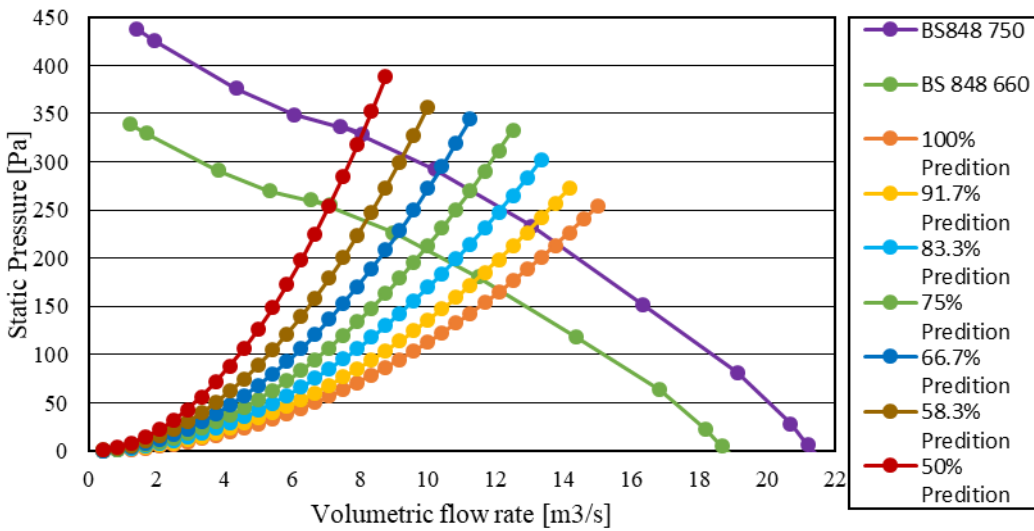


Figure 5-16: MSACC operating point prediction and comparison with aimed heat exchanger

5.4.3. The Anemometer Distance Test

Appendix C.6 and C.7 describe the test setups used to determine the distance at which the anemometers can be placed from the perforated plate in the MSACC test setup. This was critical to determine the MSACC A-frame outlet velocity distribution, outlet volumetric flow rate and the pressure dispersal across the A-

frame's perforated plates. The anemometer's velocity readings were used to correlate the data and not the voltage readings, as each anemometer's calibration curve differs from the other. Using the voltage reading would require to calibrate each individual anemometer with the perforated plate distance test. (The air velocity is the only reading that each anemometer is calibrated to).

5.5. MSACC Test Procedures

As pointed out earlier, the MSACC facility is located indoors, which reduced the effect of changing weather conditions.

A summary of the test procedure is as follows:

1. Firstly, the atmospheric pressure and temperature at the location of the MSACC was recorded before each test and setup change. Le Roux (2010) found that variations in density influence fan test results. Thus, testing had to be completed rapidly and ambient temperature was measured both before and after the test. The average of the two readings constitutes the operating temperature and pressure of the test.
2. The operating point is controlled by the porosity of the perforated plates. To change an operating point, the outlet area is reduced by blocking off some of the holes. This results in an increase in loss coefficient for the entire A-frame perforated plate. Four operating points are chosen for this test. The four perforated plate throttle positions are shown in the Figure 5-17.

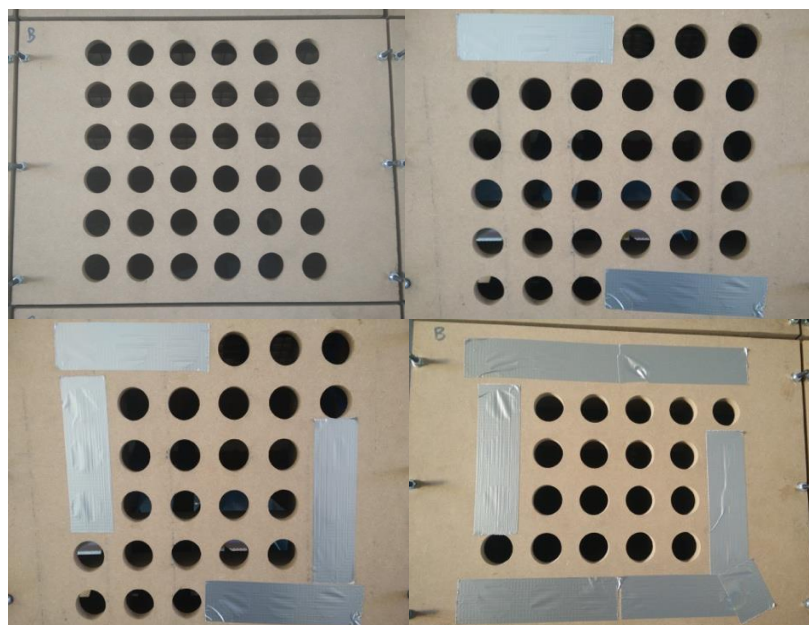


Figure 5-17: Four main perforated plate throttle positions (100% open top left, 83.3% open right top, 66.6% left bottom and 50% bottom right)

3. The anemometers' positions were set, using the fixture that secures the four anemometers across four perforated plates on each side of the A-frame. For each operating point, the anemometers had to be moved four times to measure the exit air velocity of all thirty-two perforated plates.
4. In the CATMAN™ software, the readings of all the anemometers, torque and pressure transducers were initialised to zero and these real-time readings of the non-operational state were recorded before each test run.
5. After the anemometers' position was set, the speed of the electric motor was steadily and slowly increased to the designed operational speed of the fan (750 rpm), using the VSD. For the 750 rpm data points, the VSD was set at 38.3 Hz, which constituted a shaft speed of 752 rpm and for the 660 rpm data points, the VSD was set at 34.1 Hz, which constituted an approximate shaft speed of 666-668 rpm. This was measured with a laser tachometer to confirm fan actual speed.
6. During real-time recording, CATMAN™ Easy Software enabled the researcher to identify when the flow had reached a steady state condition. It usually took less than half a minute to establish such a condition. All readings were taken for 2 minutes for each anemometer's position.
7. The speed of the electric motor was slowly reduced until it had stopped. Thereafter, the anemometers' positions were changed and steps 4-7 were repeated until all outlet air speeds were recorded. This was also repeated for each of the four perforated plate throttle positions.

Sample calculations illustrating the processing of all the recorded values are shown in Appendix C and D.

6. DATA PROCESSING, ANALYSIS AND RESULTS

6.1. Introduction

This chapter describes the processing and analysis of data captured from tests executed in the MSACC and compares the results with those obtained on the BS-848 Type-A fan test facility. To ensure the validity and accuracy of data, signal analysis was performed on raw voltage data of the instruments recorded at the MSACC. Thus, calculations were performed to convert the data into the units of measurement applicable to each instrument, in accordance with the calibration data obtained in Chapter 5.2. Using the data obtained, the operating points of the installed B2-fan in the MSACC were determined. Further calculations were carried out to scale performance values of the B2-axial flow fan for comparison between the two test facilities.

6.2. Data Processing

The tests were carried out in the MSACC, as described in Section 5.5, to determine the inlet and outlet air speed, torque, fan static pressure, static pressures in the A-frame plenum, ambient temperature and atmospheric pressure. Data averaging and deviation were calculated to describe the voltage reading's variation and establish the mean values measured by the transducers. Furthermore, signal processing was performed to determine the influence of external factors.

6.2.1. Data averaging and deviation

Eight individual tests were executed producing 244 individual test datasets (each with 16 channels of data) to establish the reliability of the data. The real-time voltage data was processed to establish the standard and relative deviation and the root mean square (RMS) value. These results were used to determine the variation of the signal from its mean value to ensure accuracy of the data.

The standard deviation is given as:

$$\sigma = \sqrt{\frac{1}{n} \sum_{i=1}^n (X_i - \bar{X})^2} \quad (6.1)$$

In the equation above, n is the size of the data population, X_i the specific value of the data point and \bar{X} the arithmetic mean value of the population. The relative standard deviation is described as:

$$RSD = \frac{\sigma}{\bar{X}} 100 \quad (6.2)$$

Using the equations above, it was found that the standard deviation for each anemometer measurement reading fluctuated between a minimum of $\sigma = 0,0076$ V and a maximum $\sigma = 0,0304$ V. Additionally, relative standard deviations ranged mostly between 1 and 4% with just two above 5%.

The RMS value of a data set is determined by the following equation:

$$RMS = \sqrt{\frac{1}{n} \sum_{i=1}^n (x_i)^2} \quad (6.3)$$

Correction factors were subtracted from the RMS real-time data, which were the RMS zero or non-operational data readings that were recorded before and after the test into account. The measurement procedure commences by firstly acquiring a zero reading for each transducer: this is outlined in the MSACC test procedures. The zero reading was used to calibrate each transducer to a non-operational state and was subtracted from the operational values after the data analysis was completed.

6.2.2. Instrument signal frequency analysis

All instrument measurements consist of two components: the instrument's signal and noise. Instrument noise is inherent in all electronic devices and is influenced by environmental factors and the design of the instrument itself. It limits the ability of the instrument to detect signals and is present in all of them; it can only be minimised (Ray, 1988). Equation(6.4) describes the signal to noise ratio (SNR) as the relationship between the magnitude of noise to magnitude of signal (standard deviation):

$$SNR_p = \left(\frac{RMS\ signal}{RMS\ noise} \right)^2 = \left(\frac{RMS}{\sigma} \right)^2 \quad (6.4)$$

The value of noise from the environment may often be reduced by shielding, grounding, and minimising wire lengths. The SNR of a signal can be enhanced by either hardware or software techniques. To establish and understand the environmental influences on the signal, a frequency spectrum analysis was performed. A Fast Fourier Transform (FFT) allows discrimination against specific frequencies because the FFT converts a time domain signal to a frequency domain one. Figure 6-1 displays the maximum amplitude spectrum for all 16 channels of the first test run sample of the MSACC.

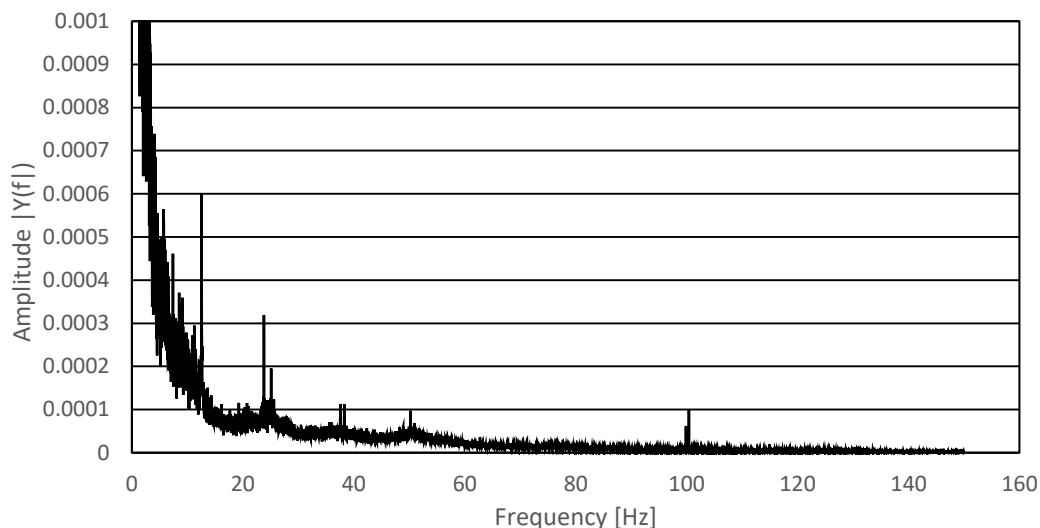


Figure 6-1: Frequency amplitude spectrum of sample data for a 750 rpm data point

The spectrum indicates that there are few environmental influences and no significant interferences caused by the power grid (50 Hz), fan's operational frequency (78.53 Hz) and the VSD's operational frequency (38.3 Hz). The influence of other frequencies can be considered as very low - they are all below an amplitude of 0.001, as the instruments are accurate to mV. An electronic filter attenuates a signal's frequencies and to remove signal noise (Ray, 1988). Therefore, a low-pass filter (removes high frequencies) was not required to reduce the environmental noise during post-processing. However, due to the large amplitude of the low frequency, a high pass filter was required. This is contributed by the anemometers and the torque transducer, observed when looking at the frequency amplitude spectrum in isolation.

6.3. Data Calculations

After the data processing was completed, the data was converted from volts to the specific transducer's units, using the calibration curves for each instrument as stipulated in Section 5.2

Pressure measurements were made relative to atmospheric pressure. There are two ways of measuring pressure in fluid flow: static and stagnation pressure. Static pressure is measured by pressure taps perpendicular to the airflow and dynamic pressure represents the pressure rise, relative to the static pressure when the fluid is brought to a stop isentropically. Stagnation pressure is measured by pressure tap pointed directly into the air stream (it is the sum of the static and dynamic pressures). The fan static pressure was measured with static pressure taps mounted downstream of the fan. (Cengel & Cimbala, 2010) The location of the pressure taps can be seen in Figure 5-9.

The inlet volumetric flow rate was determined by using the data from the six anemometers positioned in the bell mouth in front of the B2-fan. This is compared to the outlet volumetric flow rate in Table 6-5. Volumetric flow rate through the bell mouth was determined using Equation (6.5).

In the equation below, the particular anemometer's velocity reading is given as V_i , while the cross-sectional area of the bell mouth is denoted as A_b and number of anemometers are given by j .

$$\dot{v}_{in} = \sum_{i=1}^j \frac{(A_c - A_h) V_i}{j} \left[\frac{m^3}{s} \right] \quad (6.5)$$

Fan power consumption is calculated using Equation (6.6), where, T_i is the measured torque and rpm is the rotational speed of the shaft.

$$P_{f_i} = \left(\frac{2 \pi T_i rpm_i}{60} \right) [W] \quad (6.6)$$

To consider the power losses due to bearings and couplings, the no-load torque and speed readings were used to calculate the no-load power consumed. This was calculated as described in Equation (6.7):

$$P_{f_{no-load}} = \left(\frac{2 \pi T_{no-load} rpm_{no-load}}{60} \right) [W] \quad (6.7)$$

The final step in the calculation procedure was to normalise the results to the same rotational speed, diameter and density of the BS 848 Type-A facility results by using the following fan law equations:

To normalise fan power, the following equation was used:

$$P'_f = P_f \left(\frac{n'}{n} \right)^3 \left(\frac{d'}{d} \right)^5 \left(\frac{\rho'}{\rho} \right) [W] \quad (6.8)$$

Where $n' = 750 \text{ rpm}$ and $\rho' = 1.2 \frac{kg}{m^3}$

To normalise volumetric flow rate, the following equation was utilised:

$$\dot{v}'_f = \dot{v}_f \left(\frac{n'}{n} \right) \left(\frac{d'}{d} \right)^3 \left[\frac{m^3}{s} \right] \quad (6.9)$$

To normalise fan static pressure, the following equation was used:

$$p_{sf} = p'_{sf} \left(\frac{n'}{n} \right)^2 \left(\frac{d'}{d} \right)^2 \left(\frac{\rho'}{\rho} \right) [Pa] \quad (6.10)$$

From the normalised values, the fan's static efficiency is calculated as defined in Equation (6.11):

$$\eta_{sfi} = \frac{p_{sf} \dot{V}}{P_{fi} - P_{fno-load}} \quad (6.11)$$

Wilkinson and van der Spuy (2015) studied the influence of changing the blade setting angle and different fan tip configurations for the B2-fan. Hence, their empirical model for tip clearance was utilised to normalise the results obtained on the MSACC to the results obtained in the BS 848 test facility. Figure 6-2 displays the empirical curve for the effect of fan tip clearance on the value for pressure and volumetric flow rate above $6 \text{ m}^3/\text{s}$.

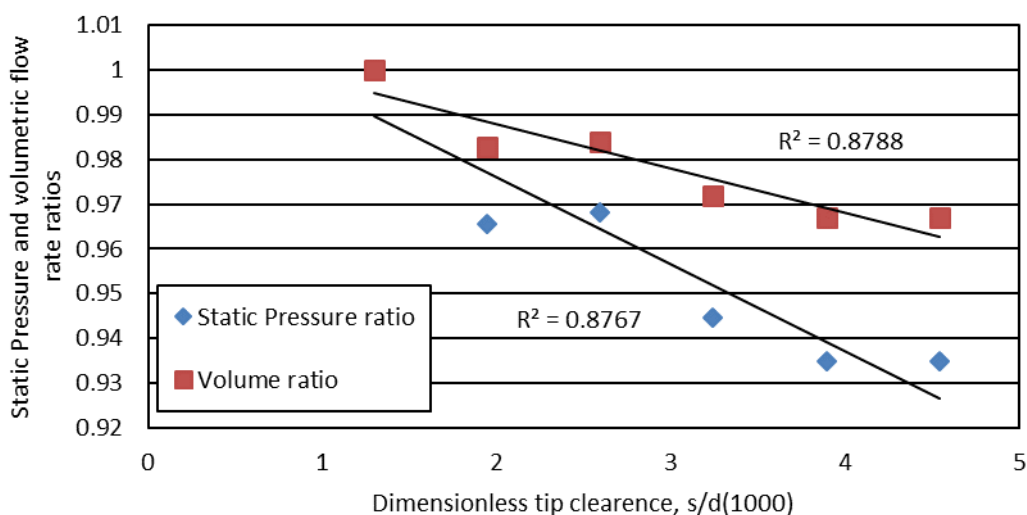


Figure 6-2: Empirical model for the influence of tip clearance (Wilkinson & van der Spuy, 2015)

6.4. MSACC Operating Point

The shaft torque, inlet and outlet air velocity distribution and B2-fan static pressure in the A-frame of the MSACC and B2-fan for all operating points were measured. The results were used to determine the inlet velocity characteristic and volumetric flow rate of the B2-fan in the MSACC. Changing the operating points had an influence on the heat exchanger's performance, which could be observed in the

static A-frame pressure readings and the outlet velocity distribution of the A-frame heat exchangers.

6.4.1. Inlet velocity distribution and anemometer tests

Two tests were conducted to measure the influence of the amount of inlet anemometers has in determining the inlet volumetric flow rate at the bell mouth of the MSACC, one with four anemometers and the other with six anemometers.

The placement of four anemometers in the bell mouth is depicted in Figure 6-3 for the 750 rpm and six anemometers in Figure 6-5 for the 750 and 660 rpm tests. The six-anemometer test was conducted to show the repeatability, the influence of the number of anemometers and external influences, and that the fan laws affinity laws are applicable for ACC fan systems. For both speed cases, the anemometers are positioned at the mid-radius of the fan rotor.

6.4.1.1. 750 rpm test (four anemometers)

Figure 6-3 below shows the anemometer position of the four-anemometer inlet test. The safety screens are indicated in yellow. The anemometers were placed in quarter bell mouth positions below the fan's blade midpoint. Figure 6-4 indicates the velocity distribution of eight individual test results for each throttle position performed at 750 rpm speed. The anemometer numbering in Figure 6-3 corresponds with that of Figure 6-4.

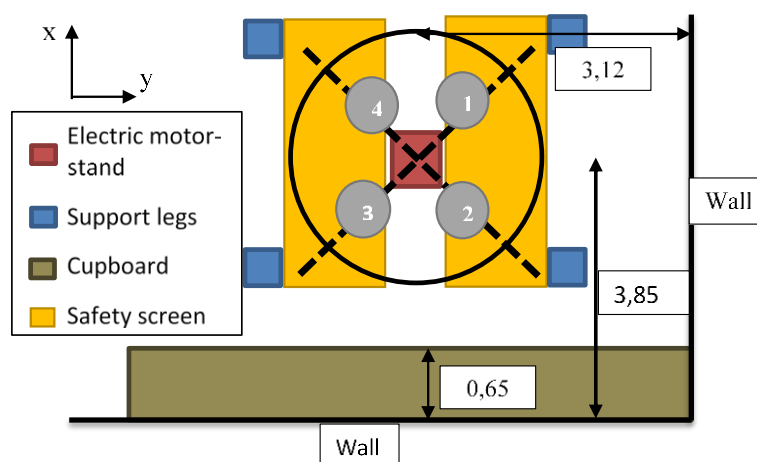


Figure 6-3: (750 rpm test) Anemometer placement in bell mouth and influencing components

Figure 6-4 shows that the throttling of the perforated plate influences the inlet velocity reading (hence the inlet volumetric flow rate) and that distribution of the inlet air flow is affected by the throttle position and placement of the anemometers. The aspects which might influence velocity readings are the distance of the walls

from the MSACC structure, the structure's support legs and the electrical motor stand.

The velocity distribution shown in Figure 6-4, indicates the influence that the presence of the walls and the cupboards have on the inlet velocity readings. Anemometers 2 and 3 displayed a marked lower velocity when compared to anemometers 1 and 4. For referral, the layout to the MSACC in laboratory is given in Appendix A. The cupboard has a larger influence on the inlet air speed than the walls. The effect of the electric motor in the middle of the bell mouth on the airflow cannot be determined from the above results. These external influences around the MSACC in the laboratory conditions need to be investigated further in future studies.

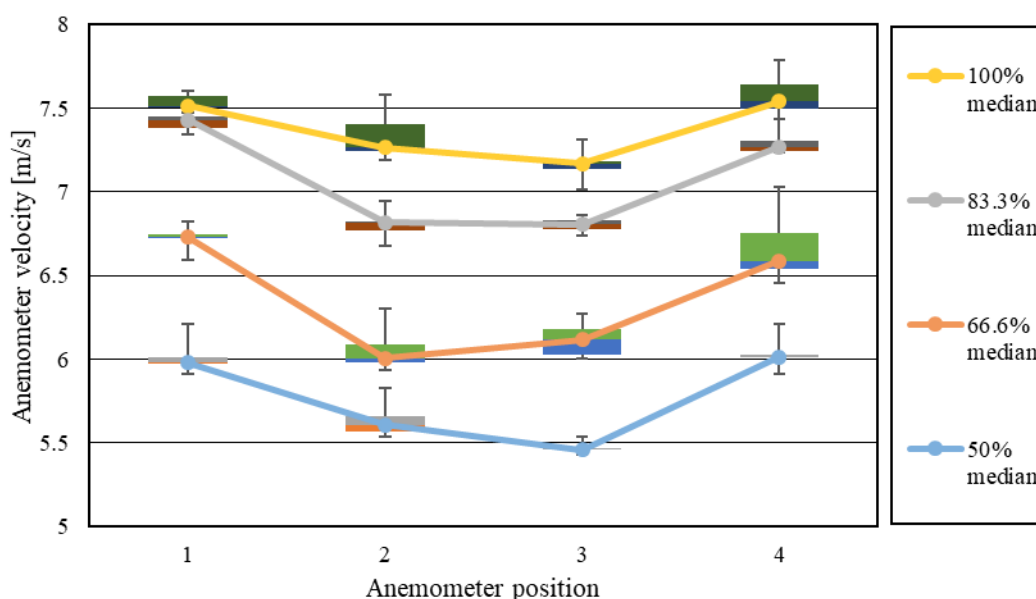


Figure 6-4: (750 rpm) Inlet air speed variation six-anemometer test results

6.4.1.2. 750 and 660 rpm test (six-anemometers)

For the six anemometer tests, two individual test were executed at 750 and 660 rpm speeds to establish whether that the two speeds for comparison with the previous test and to compare velocity distribution readings at different speeds. The test setup is portrayed in Figure 6-5. In comparison to Figure 6-3, the anemometer numbers differ in Figure 6-5 to accommodate two anemometers. The bell mouth's area was divided into six section and the anemometers were placed in each section. The anemometers were placed in Anemometers 3 and 6 are located at the points where the safety screens do not overlap the bell mouth and effect of the screen to reduce the air velocity can be seen in the figure below:

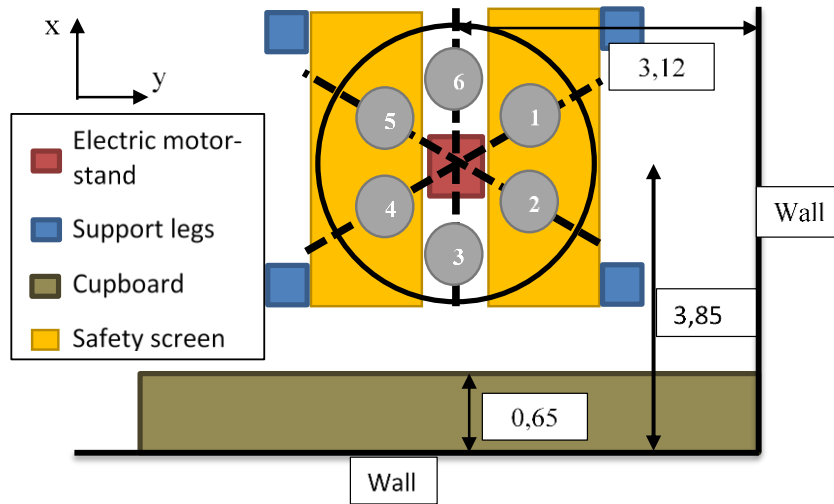


Figure 6-5: (750 and 660 rpm test) Anemometer placement for in bell mouth and influencing component

To compare with the four-anemometer inlet arrangement and improve the volumetric flow rate calculations, six anemometers and same throttle positions were used at fan speed of 750rpm, the comparison of the volumetric flow rates is given in the next sub-section. Figure 6-6 shows the test results for the test conducted. Anemometers 1, 2, 4, and 5 display the close to the same inlet variation as given in Figure 6-4.

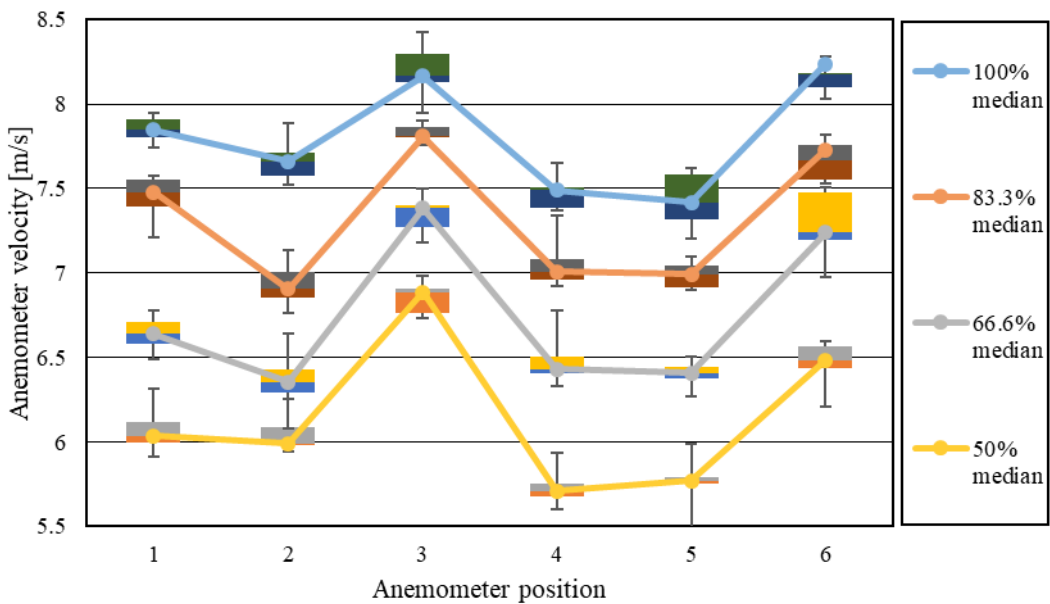


Figure 6-6: (750 rpm) Inlet air speed variation six-anemometer test

The same test was repeated at a speed of 660 rpm which yielded the near the same results as the 750 rpm. The 660 anemometer inlet variation results are shown in the following figure below:

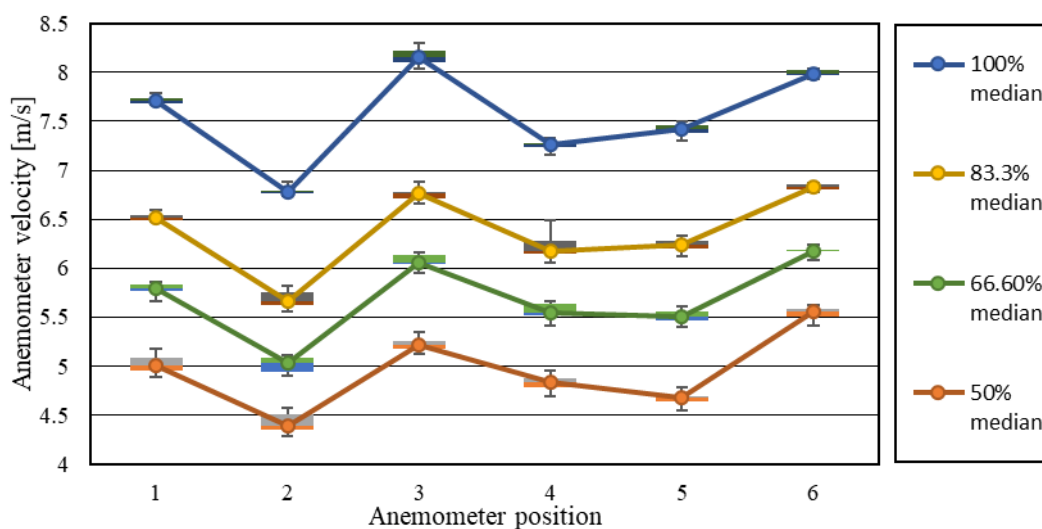


Figure 6-7: (660 rpm) six-anemometer test results inlet air speed variation

The 660 rpm test results confirm the velocity distribution results of the previous test. To keep comparisons with the previous 4 anemometer tests, the figure above does not display the velocity variation for 91.6%, 75% and 58.3% throttle positions. The three plots show that the air turbulence or reading variance is less with the fan speed. Figure 6-4, Figure 6-6 and Figure 6-7 and shows the result of one test run which comprises of 16 individual test for each throttle positions results.

6.4.2. Inlet velocity comparison

The two sets of test results of 6 and 4 anemometers were used to determine whether the inlet volumetric flow rate can be determined more accurately (when compared to the BS 848 test result) with the two anemometer arrangements. The table below compares the calculated volumetric flow rate for both 4 and 6 bell mouth inlet anemometer arrangement.

Table 6-1: (4 and 6 anemometer) Inlet volumetric flow rate comparison

Inlet anemometer / data point	1	2	3	4	5	6	Calculated inlet volumetric flow rate
Propeller diameter	0.2	0.2	0.2	0.2			
Units	[m/s]	[m/s]	[m/s]	[m/s]			[m³/s]
100% 750 (1.1)	7.986	7.128	7.033	7.559			13.319
100% 750 (1.2)	7.677	7.516	7.050	7.387			13.284
100% 750 (1.3)	7.893	7.121	6.949	7.546			13.231
100% 750 (1.4)	7.674	7.520	6.957	7.464			13.278
Propeller diameter	0.2	0.2	0.22	0.22	0.2	0.22	
Units	[m/s]	[m/s]	[m/s]	[m/s]	[m/s]	[m/s]	[m³/s]
100% 750 (1.1)	7.365	7.707	8.112	7.782	7.741	8.244	14.033
100% 750 (1.2)	7.483	7.577	8.136	7.933	7.425	8.360	14.022
100% 750 (1.3)	7.306	7.541	8.175	7.817	7.359	8.218	13.874
100% 750 (1.4)	7.546	7.574	8.156	7.718	7.412	8.235	13.941

The table shows that the placement and the quantity of the anemometers influences the volumetric flow rate calculations. The gap between the two safety screens contributes a higher velocity reading and influences the inlet volumetric flow rate. There is an average of 4.937% increase in the calculated volumetric flow rate between the two arrangements. For this reason, the four-anemometer test will not be considered for B2-fan operating point calculations in section 6.7.

6.4.3. Outlet velocity distribution

The cooling capability of an ACC is proportional to the rate of airflow through the HEBs and the temperature difference between the heat exchanger and the air entering it (Muiyser, et al., 2014). The fan's exit swirl can contribute the maldistribution of air into the heat exchanger. Therefore, the variations in exit air velocity were examined for the various throttle positions; this is plotted in Figure 6-5 and Figure 6-6. Muiyser points out that an investigation by Zapke (1997) made use of propeller anemometers attached to a cross beam to measure the velocity profile at the outlet of an ACC HEBs. The MSACC tests were conducted in the same manner by starting at the top and proceeding to the bottom of the A-frame's heat exchanger to obtain a complete outlet airflow velocity profile. Since the

resistance of the perforated plates are equal across the plenum, an assumption can be made to infer the outlet velocity distribution from these results.

The velocity through all 32 heat exchanger boxes of the A-frame were measured using the four anemometers on a crossbeam bracket as described earlier in Chapter 5.3.2 (Figure 5-11). Only the 20 cm carbon fibre type propellers were used to measure the outlet velocity. Figure 6-8 shows the eastern and western views of the MSACC's A-frame heat exchanger model, where rows (A-D) and columns (7-14) are labelled.

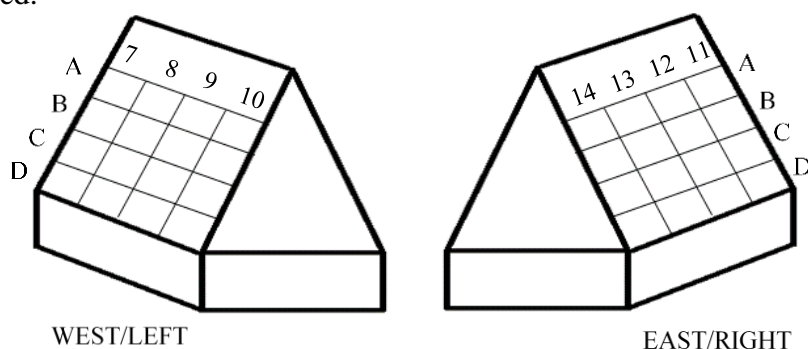


Figure 6-8: Anemometer measuring

Two crossbeam brackets were mounted across perforated plates 7-10 and 11-14 respectively. The anemometer crossbeam brackets are positioned lengthwise across the heat exchangers, in ascending order from the northern wall to the steps of the MSACC. With each throttle position, the crossbeam bracket was moved from row A to D. Each anemometer was placed 200 mm perpendicular from the centre of the heat exchanger perforated plates. The anemometers' average air speed distributions for the four row positions (and for 4 data points) on the right and left sides can be found in Figure 6-9, Figure 6-10, Figure 6-11 and Figure 6-12. Note, the figures show the velocity position-averaged results.

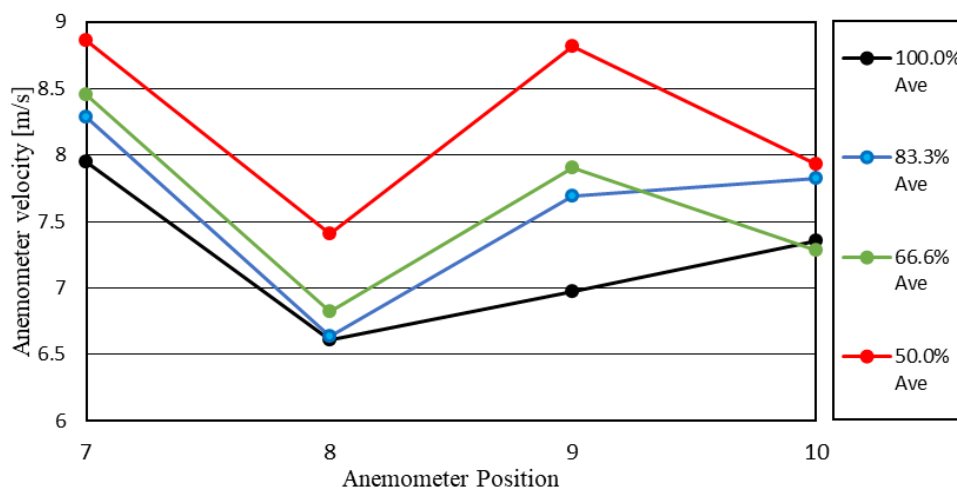


Figure 6-9: (750 rpm) Outlet air speed variation with throttling (Left side)

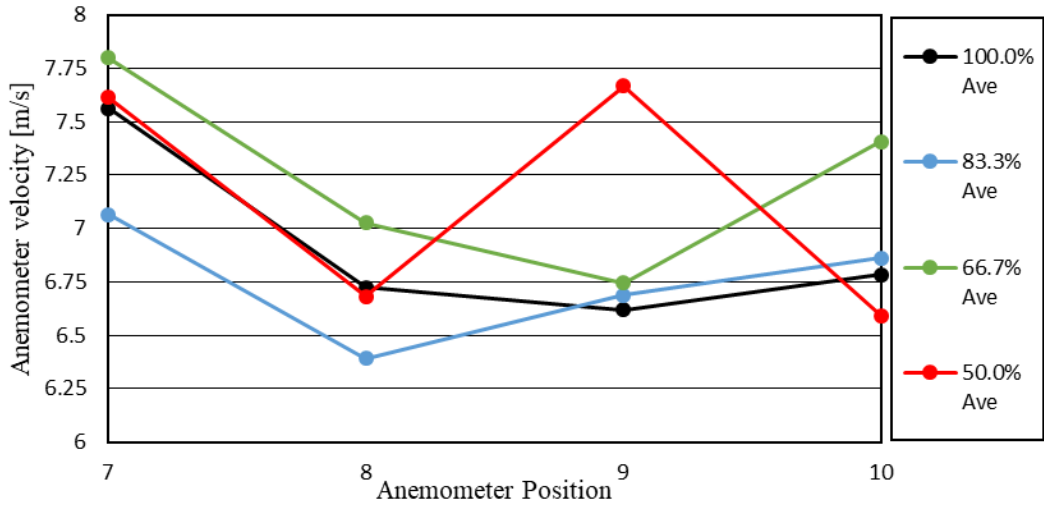


Figure 6-10: (660 rpm) Outlet air speed variation with throttling (Left side)

Figure 6-9 and Figure 6-10 shows that the outlet velocity distribution for perforated plates 7 and 10 does not as vary dramatically as the inner perforated plates. The effect of the outlet swirl distribution of the fan becomes more dominant when the heat exchangers' resistance is increased with each subsequent throttle position. The differences can be noted with anemometer 8 and 9.

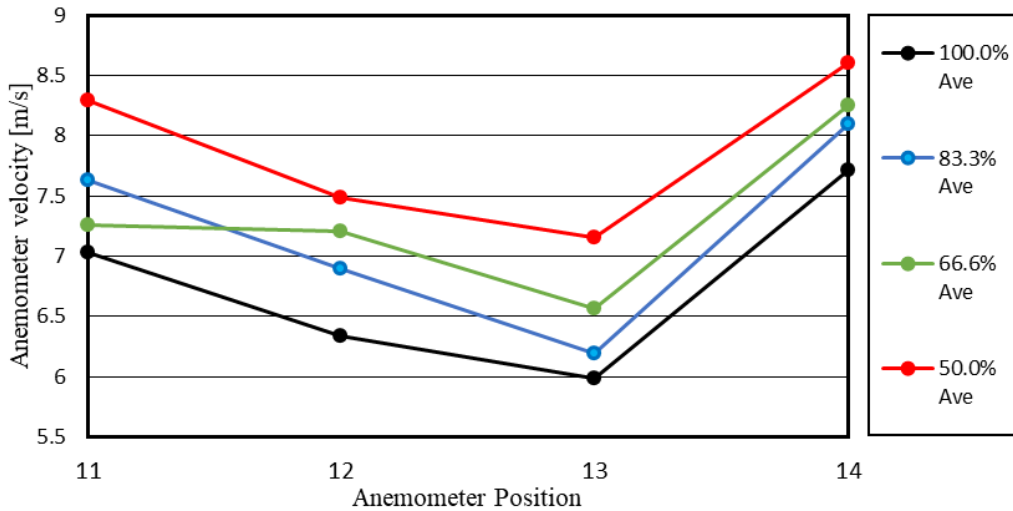


Figure 6-11: (750 rpm) Anemometer-positioned-averaged outlet air speed variation with throttling (Right side)

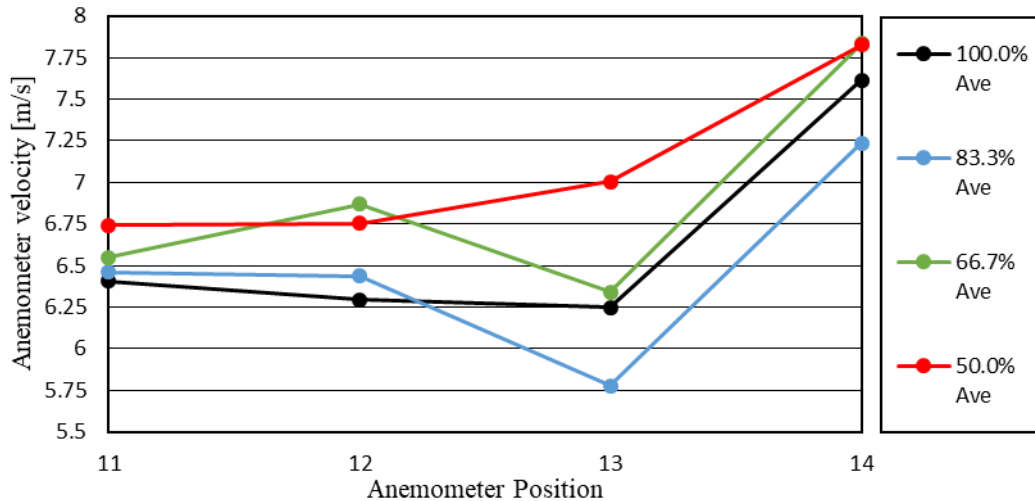


Figure 6-12: (660 rpm) Anemometer-positioned-averaged outlet air speed variation with throttling (Right side)

Just like the previous two figures, the eastern side also exhibits the same effects at the edge anemometers (11 and 14). However, Figure 6-11 and Figure 6-12's anemometer 11 does not show the same relative changes between the throttle positions. It can also be noted that the relative swirl distribution changes with each throttle position. It shows that the matching point between the different speeds is not scaled exactly.

The velocity distribution is affected by the outlet swirl component of the fan which is present in the airflow. The above is confirmed by studies undertaken by Beiler and Kröger (1996), Zhang and Yang (2015) and Rabas (1987). They studied the effect of non-uniform inlet air velocity distribution on an ACC and found that it decreases the effectiveness of the heat exchanger. An even inlet airflow distribution to the heat exchanger is vital when considering AAC performance; it ensures that the entire heat exchanger receives equally adequate airflow and that there are no cold or hot spots in the heat exchanger itself.

6.4.4. Outlet velocity comparison

To prove whether the fan's speed has an influence on the outlet velocity distribution of the ACC, the following two tables (Table 6-2 and Table 6-3) shows the anemometer's exit velocity for 750 and 660 rpm. Two colour scales (blue-white-red and green-yellow-red) were used in the tables to easily identify the varying outlet anemometer velocity readings. A lower outlet velocity is indicated in red and a higher value is given in blue/green.

The two tables show that for the particular throttle position the outlet velocity distributions (left and right) is approximately the same for the two fan speeds. Appendix D portrays the outlet velocity results for the other throttle positions.

Table 6-2: Typical outlet anemometer velocity readings for 750 rpm at 100% throttle

Anemometers /data set (Row)	Anemometer column number							
	7	8	9	10	11	12	13	14
Units	[m/s]	[m/s]	[m/s]	[m/s]	[m/s]	[m/s]	[m/s]	[m/s]
100% Test 1(A)	8.257	7.319	5.721	7.535	7.131	6.992	4.671	7.670
100% Test 1(B)	7.629	5.768	7.325	7.428	7.609	6.139	5.638	8.191
100% Test 1(C)	8.367	5.677	7.261	7.485	7.366	6.082	6.323	8.216
100% Test 1(D)	7.533	7.685	7.595	6.960	6.014	6.147	7.307	6.769

Table 6-3: Typical outlet anemometer velocity readings for 660 rpm at 100% throttle

Anemometers /data set (Row)	Anemometer column number							
	7	8	9	10	11	12	13	14
Units	[m/s]	[m/s]	[m/s]	[m/s]	[m/s]	[m/s]	[m/s]	[m/s]
100% Test 1(A)	7.457	6.955	5.097	6.836	6.320	6.300	4.906	7.215
100% Test 1(B)	7.190	5.630	6.412	6.668	6.525	5.745	5.345	7.664
100% Test 1(C)	7.236	5.686	6.529	6.616	6.481	5.751	5.833	7.934
100% Test 1(D)	6.246	6.980	6.798	5.712	5.505	5.801	6.956	5.673

6.4.5. The effect of adjacent perforated plates

To determine whether adjacent jet streams of the surrounding perforated plates has an influence on the anemometer velocity readings, a box was constructed to isolate an individual perforated plate. Table 6-4 below indicates the result of the tests conducted and what effect the adjacent perforated plate's jet streams has on an individual anemometer. Two different throttle positions were chosen to measure the effect (50% and 75%). For the two tests conducted all anemometer velocity readings were taken with the box at the designated position. The first boxed test was conducted with the box around anemometer position (Western side) B3-row2 at 50% throttle and for the second test, the box was round (Eastern side) C2-row2 at 75% throttle. The anemometer with the boundary box is indicated with a hatched boarder around it.

Table 6-4: Throttle exit anemometer influence test

		Outlet anemometers							
Test		50% test (A-frame Left side)				75% test (A-frame Right side)			
Anemometer position	Row	7	8	9	10	11	12	13	14
Units		[m/s]	[m/s]	[m/s]	[m/s]	[m/s]	[m/s]	[m/s]	[m/s]
Boxed test	A	8.132	8.120	6.791	7.291	5.474	6.658	5.193	7.265
	B	7.283	6.821	7.093	7.345	7.010	6.072	6.575	8.163
	C	7.362	6.634	8.003	6.331	6.901	6.073	6.469	8.082
	D	7.756	7.965	8.165	7.256	5.601	6.042	6.552	6.401
Unboxed test	A	8.147	5.489	7.218	6.419	5.968	6.803	5.400	7.422
	B	7.219	6.653	7.530	6.340	7.623	6.698	5.563	7.653
	C	7.456	6.583	7.955	4.554	6.931	6.073	6.529	8.160
	D	7.687	7.835	7.875	7.249	5.760	6.133	6.699	6.452

The velocity reading of the boxed anemometer registers a lower reading than when it was open to the atmosphere. Both tests (50% and 75%) show this same result. Neither, the induced wind tunnel nor the forced wind tunnel takes into account the interaction between the other perforated plates' exit jet streams. Thus, the outlet volumetric flow rate and pressure distribution calculation are regarded as estimations.

6.5. Volumetric flow rate comparison

The velocity results of the six anemometers positioned in the bell mouth were used to calculate the inlet volumetric flow rate, this was compared with exit volumetric flow rate in Table 6-5 below.

Table 6-5: Inlet and outlet volumetric flow rate comparison 750 rpm

Data point	Fan speed	Average inlet volumetric flow rate	Total volumetric flow rate (Right side)	Total volumetric flow rate (Left side)	Total outlet volumetric flow rate	Volumetric flow rate loss
	[rpm]	[m ³ /s]	[m ³ /s]	[m ³ /s]	[m ³ /s]	[m ³ /s]
100%	750	13.967	5.798	5.413	11.212	2.756
	750	14.001	5.816	5.406	11.222	2.779
83.3%	750	13.241	5.448	5.116	10.563	2.678
	750	13.059	5.434	5.066	10.500	2.559
66.6%	750	12.035	4.471	4.253	8.723	3.312
	750	12.255	4.493	4.252	8.745	3.510
50%	750	11.039	3.964	3.742	7.706	3.333
	750	11.083	3.964	3.740	7.705	3.379

Table 6-6: Inlet and outlet volumetric flow rate comparison 660 rpm

Data point	Fan speed	Average inlet volumetric flow rate	Total volumetric flow rate (Right side)	Total volumetric flow rate (Left side)	Total outlet volumetric flow rate	Volumetric flow rate loss
	[rpm]	[m ³ /s]	[m ³ /s]	[m ³ /s]	[m ³ /s]	[m ³ /s]
100%	660	13.566	5.537	5.291	10.828	2.738
	660	13.505	5.554	5.295	10.849	2.656
83.3%	660	11.436	4.751	4.508	9.259	2.177
	660	11.431	4.742	4.501	9.244	2.188
66.6%	660	10.236	4.182	3.935	8.118	2.118
	660	10.197	4.257	3.929	8.185	2.012
50%	660	8.891	3.324	3.245	6.568	2.323
	660	8.853	3.338	3.177	6.515	2.338

The exit volumetric flow rate was calculated using the forced wind tunnel anemometer and perforated plate calibration data (shown in Appendix C). Although, the A-frame was air tightened, airflow loss is also possibility due the inter-anemometer influence and air flow that passes around the anemometer. The anemometer propeller's area is 2.188 times smaller than the area between the perforated plate's outside hole perimeter. Furthermore, the forced wind tunnel results show that although the anemometer-perforated plate distance and throttle test shows favourable comparison with the volumetric flow rate, a converging-diverging nozzle, with the anemometer mounted within this nozzle would serve as a better tool to measure the airflow. The outlet volumetric flow rate can be improved if all the tests are conducted with bounding boxes to limit the jetting interaction between the adjacent perforated plates.

6.6. Outlet pressure distribution

Using the anemometer distance test in the forced wind tunnel as presented in Appendix C, the pressure distribution across the A-frame was calculated. In Appendix C, a sample of all the A-frame pressure distributions at throttle positions for both speeds are given. The following two tables below show the results for 750 rpm at the open throttle position:

Table 6-7: A-frame static pressure distribution at 100% throttle (750 rpm)

Row	East/right side anemometers				West/left side anemometers			
	7	8	9	10	11	12	13	14
Units	[Pa]	[Pa]	[Pa]	[Pa]	[Pa]	[Pa]	[Pa]	[Pa]
Row 1	120.155	93.301	58.011	98.438	86.405	84.849	35.312	102.182
Row 2	103.245	57.333	91.561	99.443	99.696	63.747	54.925	121.500
Row 3	127.660	53.607	94.402	101.633	99.826	61.667	68.330	124.061
Row 4	102.381	105.096	101.911	82.794	68.553	65.429	95.877	79.102

Row 1 and 4 correspond to the top and bottom rows respectively. The average static pressure for the A-frame left and right sides are 93.186 Pa and 81.966 Pa respectively. For all the tests, the left side of the A-frame produced a higher outlet pressure. Appendix D.5 shows that with different perforated throttle positions, closing the perforated plate increases the pressure distribution across the A-frame.

6.7. MSACC B2-Fan Performance Comparison

Test results for the static pressure, power consumption and static efficiency versus volumetric flow rate for the B2-fan in the BS 848 Type-A test facility were obtained at the test facility at University of Stellenbosch (Wilkinson & van der Spuy, 2015). A comparison between the MSACC and the BS 848 Type-A test facility test results are depicted in Figure 6-13, Figure 6-14 and Figure 6-16. The typical individual results are described in Appendix D. All pressure, volumetric flow rate and torque readings of the four-anemometer tests were discarded due to the volumetric flow rate loss being higher as a result of lower inlet volumetric flow rate readings. Due to the contamination of the adjacent jets the outlet volumetric flow rate readings will also not be used, the inlet volumetric flow rate was used.

6.7.1. Static pressure versus volumetric flow rate

The correlation between the pressure versus airflow rate for the two test facilities are depicted Figure 6-13. The differences in the bell mouth diameter of 11 mm (the MSACC bell mouth was manufactured with a smaller diameter) and the tip clearance was taken into account with the normalisation. The fan blade tip clearance is exactly the same for both sets of test results (4 mm). The two speed results both closely resemble the results of the BS 848 test facility. (The 660 rpm results were determined using the fan affinity laws.)

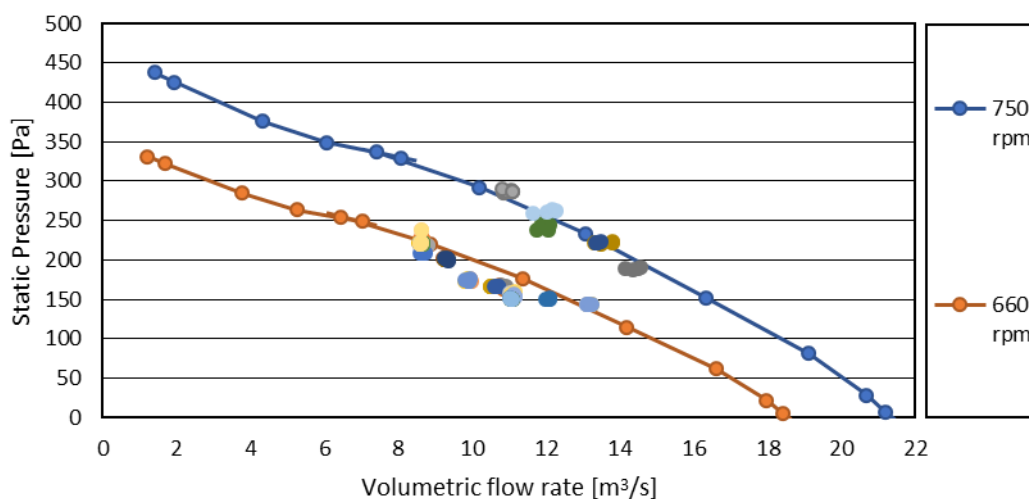


Figure 6-13: Comparison of the BS 848 and MSACC test facilities of B2-fan static pressure vs volumetric flow rate curve performance

6.7.2. Fan power consumption versus volumetric flow rate

Figure 6-14 depicts the fan power consumption versus the volumetric flow rate of the B2-fan in the two test facilities for the two speeds. The fan power consumption curve also follows that of the BS 848 test facility test results.

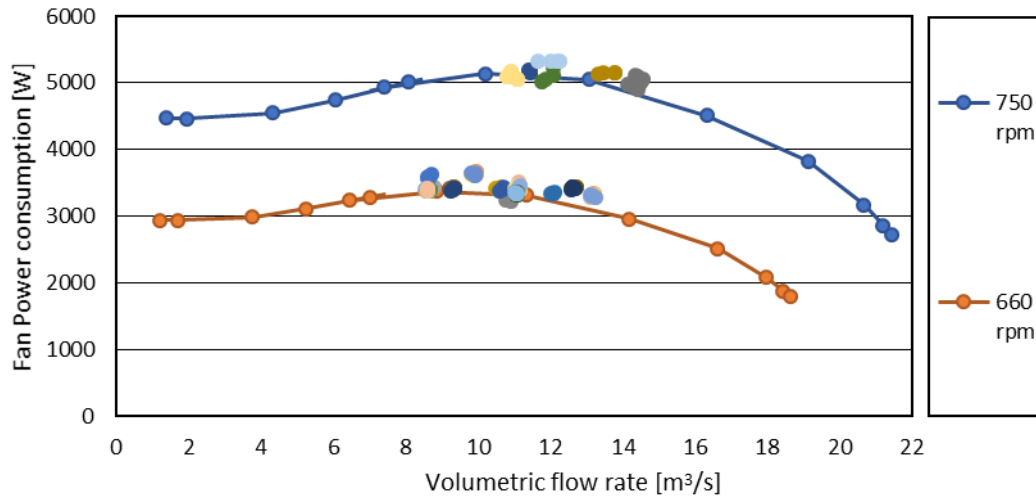


Figure 6-14: Comparison of the BS 848 and MSACC test facilities of B2-fan power vs volumetric flow rate curve performance

6.7.3. Fan static efficiency versus volumetric flow rate

Figure 6-16 demonstrates the fan static efficiency versus the volumetric of the B2-fan in the two test facilities. Indeed, the volumetric flow rate measurement influenced the efficiency calculation. The two figures closely follow the B2-fan results of the BS848 test facility.

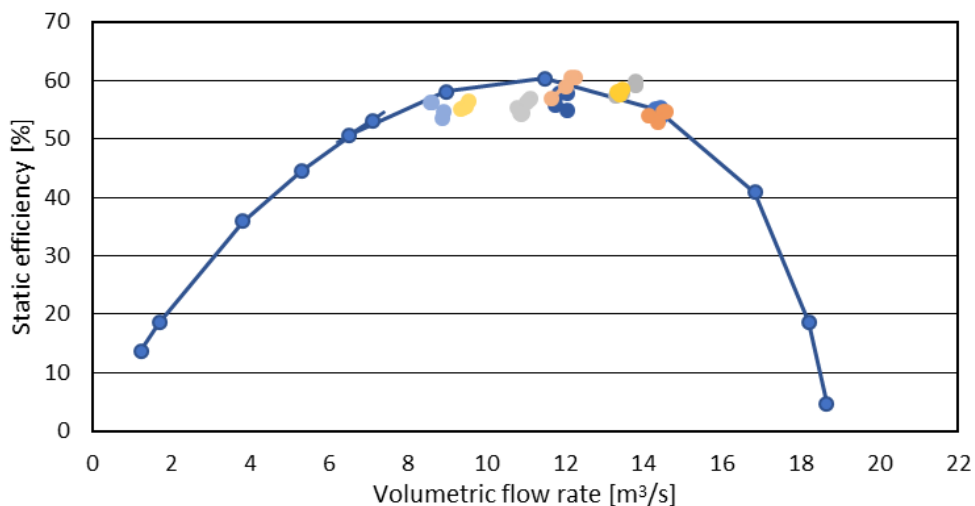


Figure 6-15: Comparison of the BS 848 and MSACC test facilities of B2-fan static efficiency vs volumetric flow rate curve performance (750 rpm)

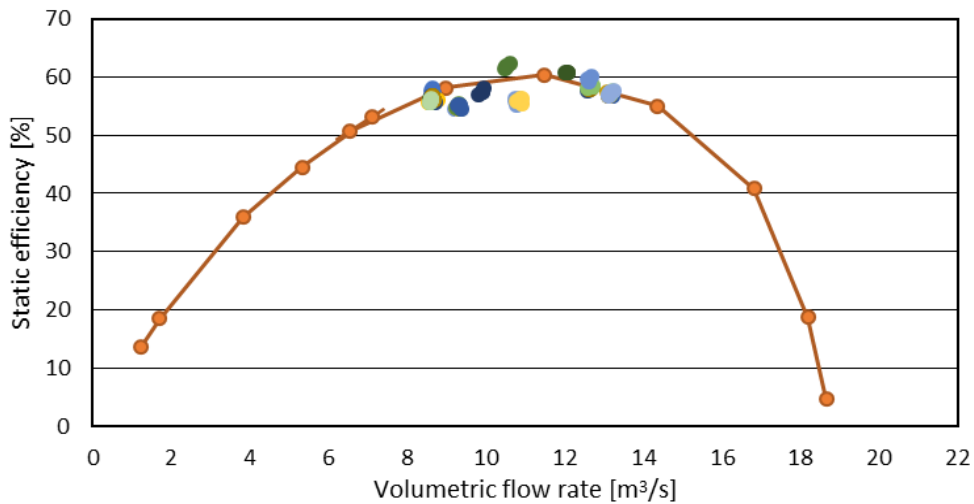


Figure 6-16: Comparison of the BS 848 and MSACC test facilities of B2-fan static efficiency vs volumetric flow rate curve performance (660 rpm)

6.8. Performance measurement

The following figure shows the predicted and measured result:

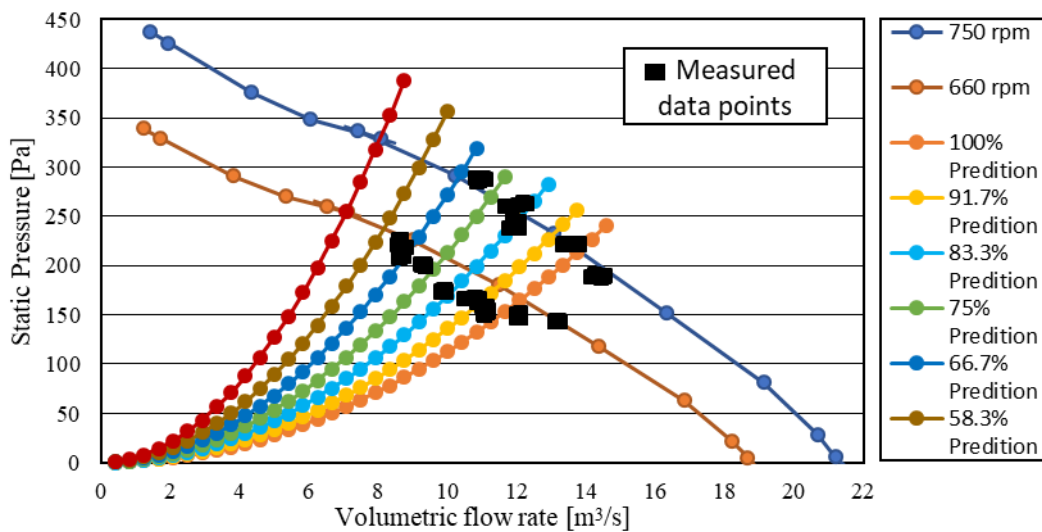


Figure 6-17: Predicted and measured results comparison

The MSACC results do not resemble the predicted values. This can be due to a pressure recovery in the plenum, which is not taken into account in the predictive results. To establish the plenum recovery coefficient, experimental data is required and this is out the scope of this research. The draft equation, that is presented in Chapter 3 and Appendix B, and was used to predict the operating range of axial

flow fan in an ACC design. This can be improved with testing in a smaller scale, which is able to fit in a wind tunnel environment, and testing individual components' pressure loss coefficients and using these results to predicted the operating point.

6.9. Conclusion

The MSACC registers a variation in the inlet and outlet velocity distribution and proves the effect it has on the performance of the fan. The inlet velocity distribution indicates how external factors influence it. The distribution that was measured in smaller increments yielded improved results. The increased number of data points provided graphs that closely resembles the BS 848 results. However, due to the fact that there is a difference between the inlet and outlet volumetric flow rate, a better method of measuring the MSACC volumetric flow needs to be established. Furthermore, the exit air velocity is influenced by the fan's exit swirl distribution and the shape of the A-frame. Indeed, it was further found that the static pressure differential across the A-frame was also an influence on the fan exit velocity.

The inlet air velocity reading in conjunction with the B2-fan static pressure was successfully used to determine the B2-fan performance for comparison to results obtained on the BS 848 Type-A fan test facility. Similarities were found in the B2-fan performance characteristic curves for the two test facilities. The results showed that the axial fan's performance can be calculated using pressure loss coefficients that were either calculated or measured. In addition, the MSACC simulates fouling of the HEBs of A-frame. The closing of the perforated plate shows the effect that fouling has on the operating point of the fan. In comparison to a full-scale ACC, with inadequate cleaning, the heat exchanger can decrease the flow rate supplied by the fan.

The MSACC test bench demonstrates that the fan's exit velocity swirl factor influences the maldistribution of airflow across the heat exchanger. The predicted results of Appendix B show that the results confirm the concept and the design choices made in the MSACC. The MSACC also shows the need to experimentally determine the pressure loss coefficients, which are not taken into account in the draft equation and indicates that possible pressure recovery in the plenum must be studied in further detail.

7. CONCLUSION AND RECOMMENDATIONS

7.1. Introduction

The axial flow fan is a dynamic machine, performs at a relatively low pressure for high flow rates, is suitable for a ventilation system and is used in many industrial HVAC applications. Using the matching principle, fan selection is undertaken to ensure that the appropriate fan is used with the installed system. The research focused its application on an ACC, the latter being the most water-efficient condenser used in arid climates, such as found in Southern Africa. The studied forced draft configuration utilises axial flow fans placed beneath the finned tube heat exchangers in an A-frame. The power station's process fluid is condensed by the differential in temperature between the HEBs and the ambient temperature. The ambient air is moved through the heat exchanger with the aid of the axial flow fan.

The fan curve is regarded as an independent parameter; the performance of the axial flow fan is matched to the airflow and pressure required for the heat exchanger. The operating point of the fan is not determined but predicted; only after experimental testing, can the results be determined.

7.2. Motivation for the Study

The rationale for this study was to improve the design of forced draft ACCs to provide results to increase the power delivered to the power station as well as achieve a reduction in operational cost. To state it differently: the aim of this research was to improve the relationship between the axial flow fan and that of the ACC system. For a direct comparison with test results conducted to establish the performance characteristics at the BS 848 Type-A test facility at the University of Stellenbosch, a modular, scaled ACC was designed, manufactured and assembled.

7.3. Research Findings

The inlet and exit air velocity, shaft torque and speed and A-frame plenum fan static pressure was used to characterise the performance of the A-frame and the B2-fan in the MSACC. The two speeds indicated a good correlation between the BS484 and the MSACC. The B2-fan operates close to the predicted range for the two speeds and the method used to define this operating range as given by Kröger (1998) is proven in this study.

The fins and the perforated plate design influence operating point of the MSACC and this range can be manipulated by increasing the pressure loss coefficient of the MSACC's heat exchanger. The MSACC test study shows the impact which the choice of HEBs and fouling can have on the operating point of the given ACC design. With increased wind tunnel testing of individual components, the operating range can be projected more closely.

The research also finds that experimental testing is required to determine the pressure recovery in the plenum and that this must be used to predict the operating point of an axial flow fan.

7.4. Future Developments

7.4.1. Aerodynamics

The location of the facility is ideal to study the effect of wind on the performance of an ACC fan. The wind could be artificially introduced by using arrays of fans on two adjacent sides. The fans with variable flow patterns can produce distorted inlet flow and could be sequenced in an algorithmic pattern to simulate the random motion of wind and, with the aid of CFD, correlations can be drawn. Conversely, wind skirts (striped curtains) might be used to produce turbulent inlet conditions.

Additionally, the aero-elastic properties of the fan could be studied and directly compared to the two facilities and the influence of gravity on the dynamics of the fan could be researched. This can improve understanding of whether the aerodynamics of the fan or the bridge can interact with one another. Coupled to one of the previous adaptations, a control environment could be established to study the influence of the simulated wind direction and magnitude on the fan's dynamics. The reaction time between the wind and the components could also be investigated.

The outlet heat exchanger's velocity results also suggest that there should be research undertaken to measure the airflow rate before and after the heat exchanger. This is to determine whether the guide fins are effective in changing the airflow direction as predicted (Meyer & Kröger, 2001). This research also suggests that there should be an investigation into placing exit guide vanes downstream of the fan

7.4.2. Structural mechanics

Gear dynamics, coupled with shaft dynamics, could be investigated on the facility. The electric motor stand, which is completely modular, could be replaced with a magnetic or regular gear drive with various speed selections. However, care needs to be taken so as not to influence the air passage into the bell-mouth.

The fans mentioned in the previous section will produce the effect that wind has on the inlet condition of the ACC. The variable nature of the wind can be more accurately simulated if an array of axial flow fans is used.

The dynamics of the bridge are dependent on the bridge material choice, beam design and weight. The A-frame has a detachable roof that facilitates the testing of various types of fan bridge designs which could replace the designed one. A more elastic bridge with spline couplers and vibration shakers can be used to study the

bridge's dynamic response and the effect it has on fan performance (induced vibration). The height of the bridge can also be altered.

7.5. Future MSACC design improvements

No design is perfect and with iteration the current design can be improved. The following sections below discuss the various different design changes that can be implemented. This section is intended for the researcher that will be following up on the work that I have started.

7.5.1. MSACC electric motor stand

An improved electric motor stand must be designed and developed. A more rigid design must be incorporated as the current design does not take in account the two bottom beams. This will have changed the vibration characteristics of the electric motor stand.

7.5.2. Hub design

A new hub design can be implemented. A design of a cover for the electric motor stand and any entities downstream of the fan can be moulded out of fibre glass

7.5.3. Setup time reduction

To reduce the setup time between the individual tests, a rail (like those found in cupboards) can be used to move the eight anemometers to the four different rows or two sets of 16 anemometers can be placed on the A-frame to measure the exit velocity's distribution all at once.

7.6. Conclusion

In conclusion, this research proves the need to test the fan in the installed condition in order to improve the correlation between the tested results. The performance curves of the B2-fan could be reproduced in the MSACC and its operating range was limited by the heat exchanger model (perforate plate and guide fins) pressure loss characteristics in the A-frame. However, since there is a difference between the inlet and outlet volumetric flow rate, a better method of measuring the MSACC volumetric flow needs to be established. Although the performance of the B2-fan was not captured as per BS 848 Type-A, from the measurements taken, it was possible to define the operating point of the MSACC and the performance characteristics of the axial flow fan in its installed condition. The MSACC is a good research tool for the University of Stellenbosch and can be used to understand the interaction between the axial flow fan and the heat exchanger.

8. REFERENCES

Asafu-Adjaye, J., 2000. *The relationship between energy consumption, energy prices and economic growth: Time series evidence from Asian developing countries*, Brisbane: The University of Queensland.

Augustyn, O. P., 2013. *Experimental and Numerical Analysis of Axial Flow Fans*, Stellenbosch: University of Stellenbosch.

Bakirtas, T., Bildirici, M. E. & Kayikci, F., 2012. Economic growth and electricity consumption: Auto regressive distributed lag analysis. *Journal of Energy in Southern Africa*, November, 23(4), pp. 29-45.

Beiler, M. & Kröger, D. G., 1996. Thermal performance reduction in air-cooled heat exchangers due to nonuniform flow and temperature distributions. *Heat Transfer Engineering*, 17(1), pp. 82-92.

Blake, D. J., 2013. *Performance and acceptance testing of main mine ventilation fans*. Adelaide, Carlton, Victoria The Australasian Institute of Mining and Metallurgy, pp. 141-148.

Bredell, J., 2005. *Numerical investigation of fan performance in a forced draft air-cooled steam condenser*, Stellenbosch: s.n.

Bruneau, P., 1994. *The design of a single rotor axial flow fan for cooling tower application*. Stellenbosch(Westen Cape): University of Stellenbosch.

Cengel, Y. A. & Boles, M. A., 2011. *Thermodynamics: An engineering approach*. Singapore: McGraw-Hill.

Cengel, Y. A. & Cimbala, J. M., 2010. *Fluid mechanics: Fundamentals and applications*. 2nd ed. London: McGraw-Hill education.

Cory, W., 2012. *Fans and Ventilation - A Practical Guide*. 3rd Edition ed. New York: Elsevier.

Dixon, S. L., 1978. *Fluid Mechanics, Thermodynamics of Turbomachinery*. 3rd ed. Liverpool: Pergamon Press.

Dwyer, T., 2012. *Module 37: The performance of fans in ducted air systems*. [Online]

Available at: <https://www.cibsejournal.com/cpd/modules/2012-02/>
[Accessed 7 November 2017].

Hamon Group, 2016. *Natural draft cooling towers*. [Online] Available at: <http://www.hamon.com/en/cooling-systems/wet-cooling-systems/natural-draft-cooling-towers/natural-draft/> [Accessed 15 November 2016].

Hottinger Baldwin Messtechnik, 2016. *HBM instruments*. [Online] Available at: <https://www.hbm.com> [Accessed 3 September 2016].

Kraft, A. & Kraft, J., 1978. On the relationship between energy and GNP. *Journal of Energy and Development*, 3(2), p. 401–403.

Kröger, D. G., 1998. *Air-cooled Heat Exchangers and Cooling Towers: Thermal-flow, performance, evaluation and design*. Stellenbosch: Department of Mechanical Engineering of University of Stellenbosch.

Langenhoven, P., 2016. *Problems experienced of the Air-Cooled Condensers at Van Eck power station* [Interview] (15 September 2016).

Lawrence Berkeley National Laboratory, 2003. *Improving Fan System Performance, a sourcebook for industry*, Washington: Air Movement and Control Association International, Inc..

Le Roux, F. N., 2010. *The CFD simulation of an axial flow fan*, Stellenbosch: s.n.

Leedy, P., 2005. *Practical research*. 8th ed. New York: Peason.

Louw, F. G., 2011. *Performance Trends of a Large Air-Cooled Steam Condenser during Windy Conditions*, Stellenbosch: University of Stellenbosch.

Lownie, K. J., 2008. *Understanding fan test standards and ventilation system performance*. Howden, <https://www.researchgate.net/>.

Mann, M., 2006. *HOW TO USE SYSTEM-HEAD CURVES*. [Online] Available at: http://www.peerlessxnet.com/documents/tibs/TIB-7_How-to-use-head-curves.pdf [Accessed 10 May 2017].

Melo, C., Pottkerk, G. & Pereira, R. H., 2006. *Aerodynamic Performance of Air Cooled Condensing Units*. Purdue, Purdue University Libraries, pp. R095, Page 1 - 8.

Meyer, C., 2000. *A numerical investigation of the plenum chamber aerodynamic behaviour of mechanical draught air-cooled heat exchangers*, Stellenbosch: s.n.

- Meyer, C. & Kröger, D., 2001. Air-cooled heat exchanger inlet flow losses. *Applied Thermal Engineering*, 1(21), pp. 771-786.
- Miketa, A. & Merven, B., 2013. *Southern African Power Pool: Planning and Prospects for Renewable Energy*, Abu Dhabi: IRENA.
- Mohandes, M. A., Jones, T. V. & Russell, C., 1984. *Pressure loss mechanism in resistances inclined to air flow with application to fintubes*. Leeds, The Institution of Chemical Engineers Symposium Series, pp. 1175-1185.
- Mortensen, K., 2011. *Improved Performance of an Air Cooled Condenser (ACC) Using SPX Wind Guide Technology at Coal-Based Thermoelectric Power Plants*, Overland Park: s.n.
- Muiyser, J., 2012. *Simultaneous measurement of airflow conditions and the resultant blade and gearbox loading at large-scale cooling system fans*, Stellenbosch: University of Stellenbosch.
- Muiyser, J., Els, D. N., Spuy, S. J. v. d. & Zapke, A., 2014. Measurement of airflow and blade loading at a large-scale cooling system fan. *South African Institution of Mechanical Engineering R & D Journal*, XXX(1), pp. 30-38.
- Powermag, 2016. *Air-cooled condensers eliminate plant water use*. [Online] Available at: <http://www.powermag.com/air-cooled-condensers-eliminate-plant-water-use/> [Accessed 18 November 2016].
- Putman, R. E. & Jaresch, D., 2002. *The impact of air cooled condensers on plant design and operations*, Bochum: Conco Consulting Corp.
- Rabas, T., 1987. Effect of non-uniform inlet flow and temperature distributions on the thermal performance of air-cooled condensers. *ASME Heat Transfer Division*, 75(1), pp. 29-35.
- Ray, M. S., 1988. *Engineering Experimentation*. London: McGraw-Hill.
- Singh, R., 2013. *Air Cooled Condensers - A Dry Cooling Tower*. [Online] Available at: <http://powertechview.blogspot.com> [Accessed 16 August 2016].
- SPX Cooling Technologies, 2015. *ModuleAir™ air cooled condenser*, BRUSSELS: SPX Cooling Technologies, Inc..
- Thiart, G. D., 1991. *A numerical procedure for predicting the effects of distorted inflow conditions on the performance of axial flow fans*, Stellenbosch: s.n.

van Aarde, D. J. & Kröger, D. G., 1993. Flow Losses through an array of A-frame heat exchangers. *Heat transfer engineering*, 14(1), pp. 43-51.

van der Spuy, S. J., von Backström, T. W. & Kröger, D. G., 2010. An Evaluation of Simplified Methods to Model the Performance of Axial Flow Fan Arrays. *South African Institution of Mechanical Engineering R&D Journal*, XXVI(1), pp. 12-20.

Vemco Inc., 2016. *Vemco Technical Library*. [Online] Available at: <http://www.vemcoinc.com/vemco-technical-library> [Accessed 13 August 2016].

Venter, S. J., 1990. *The effectiveness of Axial flow fans in A-frame Plenums*, Stellenbosch: University of Stellenbosch.

Venter, S. & Kröger, D., 1991. An evaluation of methods to predict the system effect present in air-cooled heat exchangers. *Heat Recovery Systems & CHP*, 11(5).

Wallis, R., 1983. *Axial flow fans and ducts*. New York: John Willey & Sons.

Weber, L., Cherian, M., Allen, M. & Muste, M., 2000. *Headloss characteristics for perforated plates and flat nar screens*, Iowa city: The University of Iowa.

White, F. M., 2003. *Fluid Mechanics*. 5th Edition ed. London: McGraw-Hill.

Wilkinson, M. B. & van der Spuy, S. J., 2015. The effect of fan tip configuration on air-cooled condenser axial flow fan performance. *Fan 2015*, (1)((1)), pp. 1-12.

Zapke, A., 1997. *Vapor-condensate interactions during counterflow in inclined reflux condensers*. Baltimore, ASME National Heat Transfer Conference, pp. 157-162.

Zhang, Z. & Yang, J., 2015. The effect of face-air velocity distribution on heat transfer performance of air-cooled condensers. *International journal of heat and technology*, 33(1), pp. 55-62.

APPENDIX A: THE DIMENSIONS OF THE MSACC

1.	Introduction	1
1.1.	Overview	1
1.2.	Background.....	2
1.3.	Problem Statement.....	3
1.4.	Scope and Limitations of the Study.....	3
1.5.	Objectives of the Study.....	4
1.6.	Methodology.....	4
1.7.	Significance of this Study and its Implications	4
1.8.	Thesis Overview	5
2.	Literature review	6
2.1.	Introduction	6
2.2.	Turbomachines	6
2.2.1.	Application of axial flow fans	6
2.2.2.	Ventilation system and fan selection.....	6
2.2.3.	Fan specifications	8
2.3.	Power Plants	9
2.4.	The Air-cooled Condenser.....	11
2.4.1.	Types of forced draft air-cooled condensers	12
2.4.2.	ACC performance	13
2.5.	Standardisation of Fan Performance Testing.....	15
2.5.1.	Fan performance testing	15
2.5.2.	The types of BS 848 standard test arrangements.....	16
2.5.3.	Limitations of ISO 5801 / BS 848 part 1 standard	16
2.6.	Performance measurement of ACCs.....	18
3.	Theoretical analysis	19
3.1.	Introduction	19
3.2.	Air-cooled condenser draft equation	20
3.2.1.	Upstream and Downstream Obstacles Affecting the Fan.....	21
3.2.2.	Mean flow incidence angle.....	21
3.2.3.	Inlet pressure loss coefficient	21
3.2.4.	Jetting loss coefficients	22
3.2.5.	Outlet loss coefficients	23
3.2.6.	Heat exchanger pressure loss coefficient	24
3.3.	MSACC Theoretical analysis	25
3.3.1.	Perforated Plates and Guide Fins	25
3.3.2.	Safety Screen.....	26
4.	Design of small scale air-cooled condenser test bench	27
4.1.	Introduction	27
4.2.	Design Limitations and Requirements.....	28
4.3.	The Design Concepts Considered.....	29
4.3.1.	Scaled unit	29
4.3.2.	ACC plenum design	29
4.3.3.	Inlet bell mouth	29
4.3.4.	Arrangement of the electric motor	29

4.4. Technical Review of the MSACC Design.....	30
4.4.1. Support structure, platform and A-frame structure floor.....	31
4.4.2. The bell mouth	31
4.4.3. Electric motor and stand.....	32
4.4.4. Fan bearing housing and fan bridge	32
4.4.5. A-frame plenum	33
4.4.6. Perforated plate and guide fins.....	34
4.4.7. Anemometer cross beam bracket	35
4.5. Manufacturing, Construction and Assembly	35
4.5.1. Support structure	35
4.5.2. Bell mouth.....	36
4.5.3. MSACC A-frame	36
4.5.4. Plenum sealing	36
4.5.5. Fan bearing housing	36
4.5.6. Electric motor stand	37
4.5.7. Variable speed drive and safety screen	37
4.5.8. MSACC B2 axial flow fan installation	38
5. Instrumentation Calibration, MSACC Test setup and MSACC testing procedure	39
5.1. Introduction	39
5.2. Measurement Equipment.....	39
5.2.1. Torque transducer.....	40
5.2.2. Propeller anemometer calibration	42
5.2.3. Laser Tachometer, barometer and thermometer.....	45
5.2.4. Pressure transducers	46
5.2.5. MSACC AutoTran pressure transducer calibration	47
5.3. MSACC Test Setup	48
5.3.1. Data logging equipment	49
5.3.2. Instrumentation installation.....	50
5.4. Pre-tests	51
5.4.1. Determining of the porosity of the perforated plate	51
5.4.2. Perforated plate porosity test.....	52
5.4.3. The Anemometer Distance Test.....	55
5.5. MSACC Test Procedures.....	56
6. Data Processing, Analysis and Results	58
6.1. Introduction	58
6.2. Data Processing	58
6.2.1. Data averaging and deviation.....	58
6.2.2. Instrument signal frequency analysis	59
6.3. Data Calculations.....	60
6.4. MSACC Operating Point.....	62
6.4.1. Inlet velocity distribution and anemometer tests.....	63
6.4.2. Inlet velocity comparison	66
6.4.3. Outlet velocity distribution.....	67
6.4.4. Outlet velocity comparison	70
6.4.5. The effect of adjacent perforated plates	71
6.5. Volumetric flow rate comparison	72
6.6. Outlet pressure distribution.....	73
6.7. MSACC B2-Fan Performance Comparison	74

6.7.1.	Static pressure versus volumetric flow rate.....	74
6.7.2.	Fan power consumption versus volumetric flow rate.....	75
6.7.3.	Fan static efficiency versus volumetric flow rate.....	75
6.8.	Performance measurement.....	76
6.9.	Conclusion.....	77
7.	Conclusion and Recommendations	78
7.1.	Introduction	78
7.2.	Motivation for the Study.....	78
7.3.	Research Findings.....	78
7.4.	Future Developments.....	79
7.4.1.	Aerodynamics.....	79
7.4.2.	Structural mechanics	79
7.5.	Future MSACC design improvements.....	80
7.5.1.	MSACC electric motor stand	80
7.5.2.	Hub design.....	80
7.5.3.	Setup time reduction.....	80
7.6.	Conclusion	80
8.	References	81
Appendix A: The dimensions of the MSACC		A.1
A.1	Laboratory Layout	A.4
A.2	General Dimensions of MSACC.....	A.4
A.3	B2-fan Axial Flow Fan Specification and Performance	A.5
Appendix B: MSACC Draft equation Calculations.....		B.1
B.1	Air-cooled heat exchanger draft equation	B.1
B.2	MSACC draft equation	B.2
B.3	MSACC parameters	B.3
B.3.1.	The thermo-physical properties of air:	B.3
B.3.2.	Upstream obstacles.....	B.3
B.3.3.	MSACC B2-fan dimensions.....	B.3
B.3.4.	Downstream obstacles.....	B.3
B.4	Determining the MSACC operating conditions	B.4
B.4.1.	heat exchanger supports pressure loss coefficient.....	B.4
B.4.2.	Up- and down-stream pressure loss coefficient.....	B.4
B.4.3.	Contraction loss coefficient.....	B.5
B.4.4.	Outlet loss coefficient.....	B.5
B.4.5.	Heat exchanger pressure loss coefficient	B.5
B.5	MSACC Duty Point Sample Calculations	B.6
Appendix C: Induced draft wind tunnel layout, experiment description and conducted test results		C.1
C.1	Induced wind Tunnel Setup and calculation	C.1
C.2	Air Properties calculations	C.3
C.3	Induced wind tunnel pressure transducers calibration	C.4
C.4	Induced wind tunnel leakage test	C.6
C.5	Perforated plate porosity test.....	C.7
C.6	Induced wind tunnel distance Anemometer calibration.....	C.11
C.7	Forced wind tunnel distance Anemometer calibration.....	C.13
C.8	Chosen Perforated Plate Throttle Test Results.....	C.17

Appendix D: MSACC Test dataD.1
 D.1 Inlet velocity distribution D.1
 D.2 Outlet velocity distribution D.3
 D.3 A-frame outlet pressure distribution 660 rpm..... D.7
 D.4 A-frame outlet pressure distribution 750 rpm..... D.9
 D.1 MSACC B2-fan Performance Sample Calculations D.10

A.1 Laboratory Layout

The general layout of the MSACC before construction is depicted in the following drawing. The selected placement of the MSACC is marked in red.

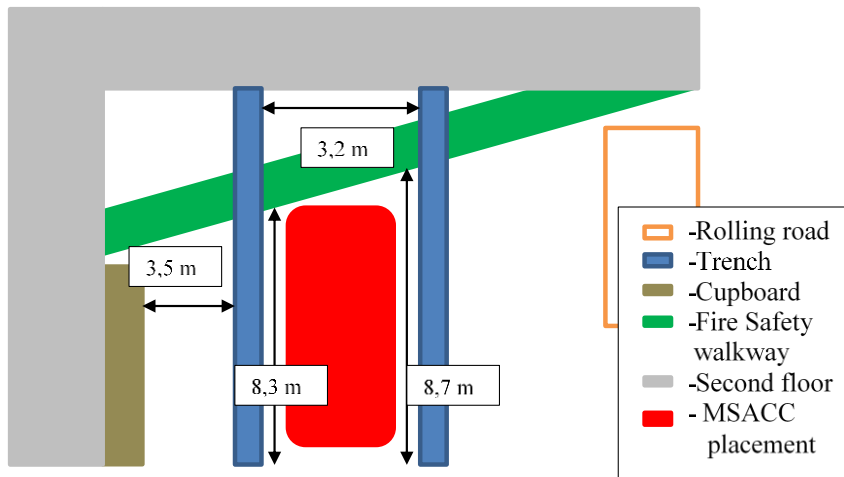


Figure A-1: Laboratory layout before MSACC construction

A.2 General Dimensions of MSACC

The following two-dimensional CAD drawing indicates the general appearance of the MSACC as seen from the side and front with its general dimensions.

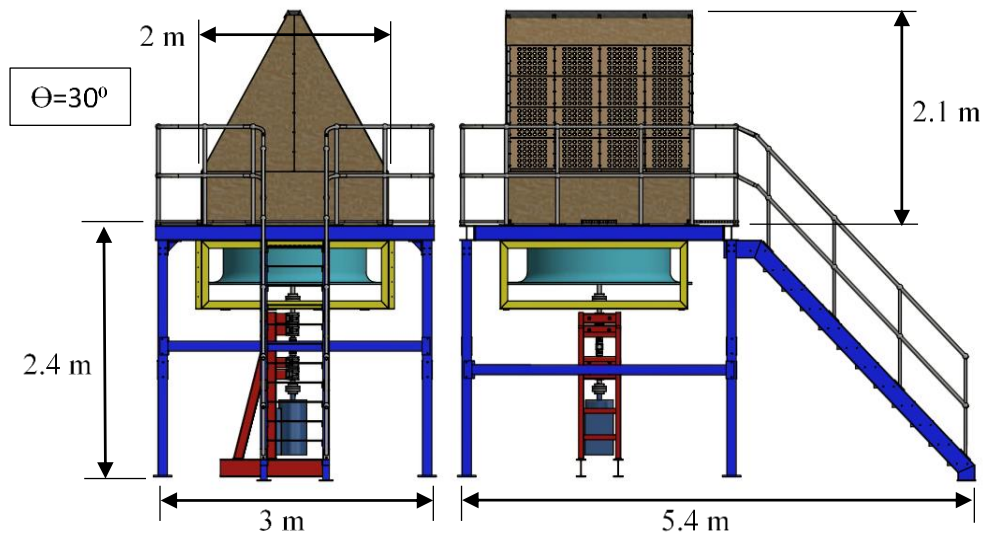


Figure A-2: CAD drawing layout front and left view of MSACC design

A.3 B2-fan Axial Flow Fan Specification and Performance

The general geometric specifications of the B-2 axial flow fan as test per BS 848 Type-A can be found in Table A-1 below:

Table A-1: B2-fan specifications as tested in BS 848 test facility (Wilkinson & van der Spuy, 2015)

Shroud diameter [m]	1.542
Blade number	8
Chord hub [m]	0.184
Chord tip [m]	0.153
Fan diameter [m]	1.536
Hub/tip ratio	0.4
Hub diameter [m]	0.6144

The results were obtained by Wilkinson & van der Spuy (2015) by testing the B2-fan in the BS 848 Type-A at the University of Stellenbosch. The operational range of the B2-fan range is from 1.3 to 21.2 m³/s. The 660 rpm characteristic was determined using the fan affinity laws. The fan static pressure, power consumption and static efficiency verses volumetric flow rate is depicted in Figure A-2, A-3 and A-4.

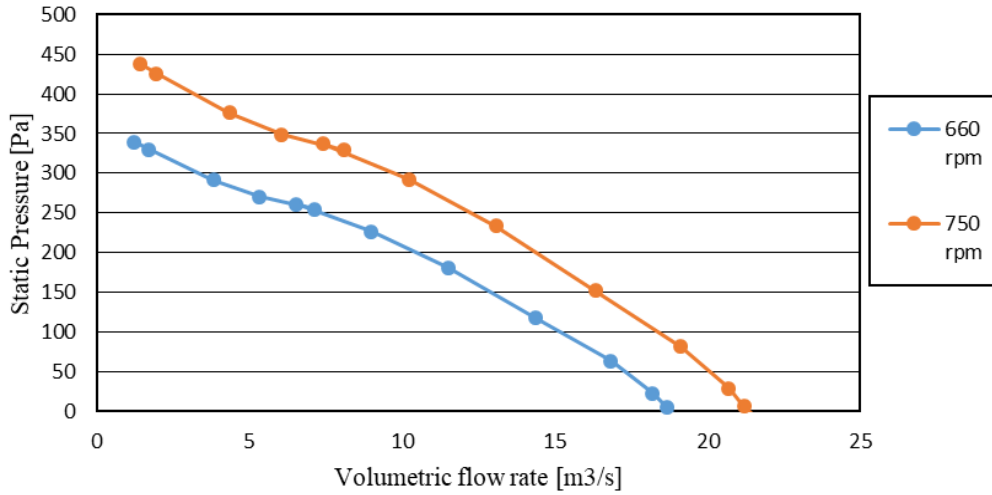


Figure A-3: B2-axial flow fan BS-848 test results static pressure vs flow rate at 31degrees (Wilkinson & van der Spuy, 2015)

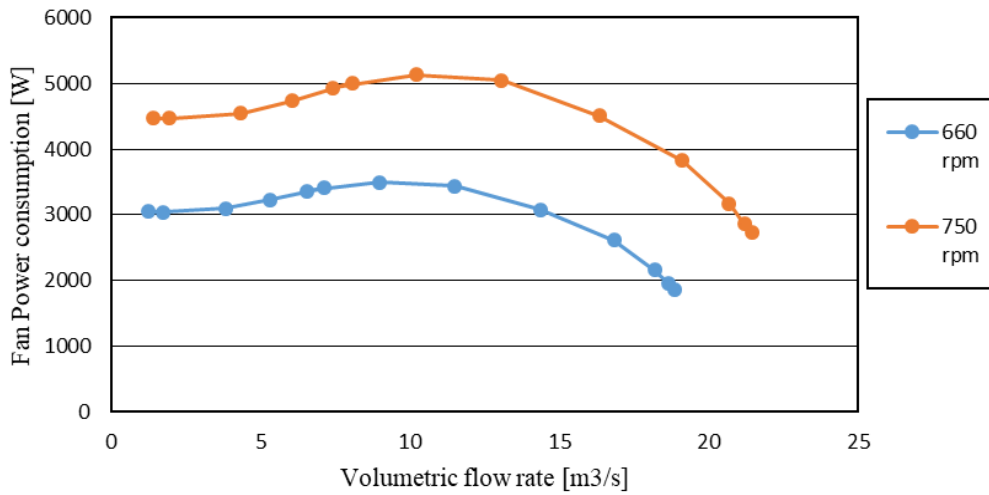


Figure A-4: B2-axial flow fan BS-848 test results power vs flow rate at 31degrees (Wilkinson & van der Spuy, 2015)

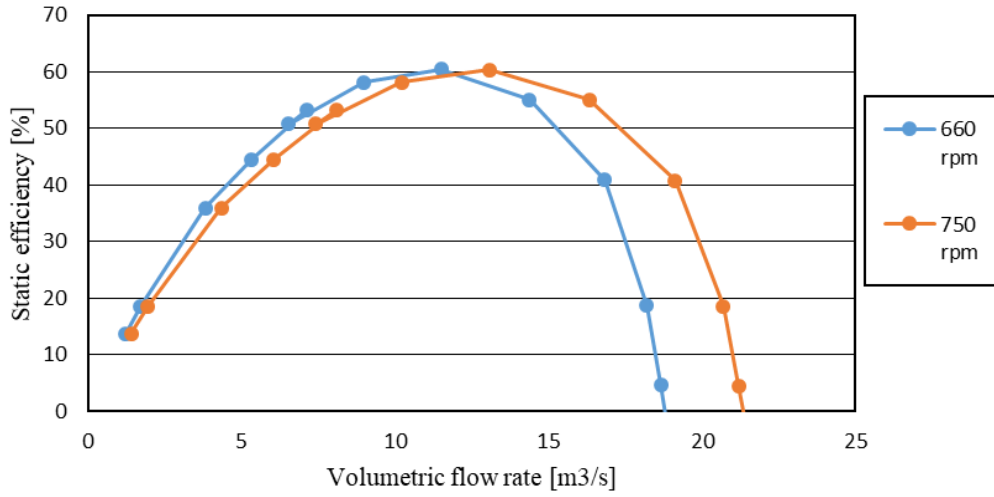


Figure A-5: B2-axial flow fan BS-848 test results static efficiency vs flow rate at 31degrees (Wilkinson & van der Spuy, 2015)

APPENDIX B: MSACC DRAFT EQUATION CALCULATIONS

B.1 Air-cooled heat exchanger draft equation

The figure below shows an air-cooled heat exchanger schematic diagram, with seven sections. The heat exchanger consists of rows of finned tubes that are located horizontally above the axial flow fan. The height of the fan and the plenum is indicated by the symbols H_3 and H_{pl} . H_w indicates the height of a wind wall that is installed to reduce air recirculation (Kröger, 1998).

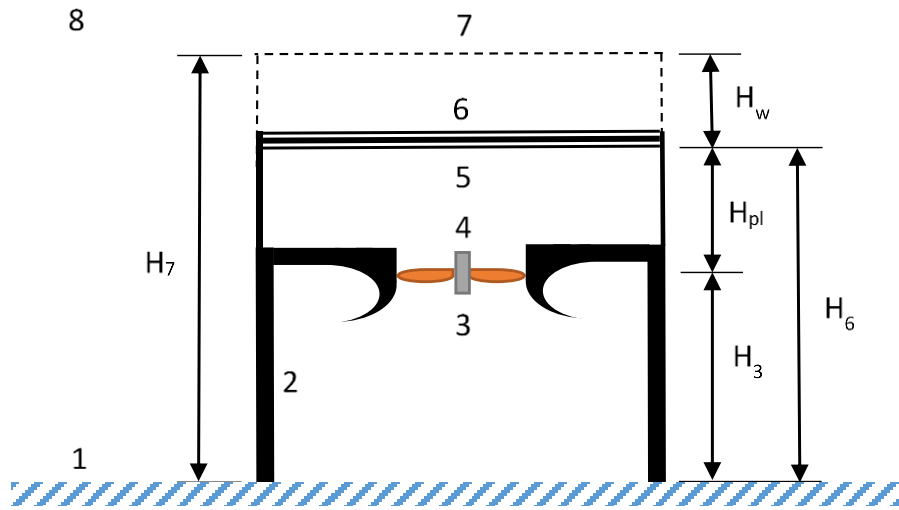


Figure B-1: Forced draft air-cooled heat exchanger (Kröger, 1998)

Applying the pressure loss expression (Equation (2.1)) on each section of an air-cooled heat exchanger results in the equation below: (equation 8.1.9 in (Kröger, 1998))

$$\begin{aligned}
 \rho_{a_1} \left\{ \left[1 - \left(1 - 0.00975 \frac{H_6}{T_{a_1}} \right)^{3.5} \right] - \left[1 - \left(1 - 0.00975 \frac{H_7 - H_6}{T_{a_6}} \right)^{3.5} \right] \right\} &\approx \left(\frac{K_{ts}}{2 * \rho_{a_1}} * \left(\frac{m_a}{A_2} \right)^2 \right) \\
 + \left(\frac{K_{Fsi}}{2 * \rho_{a_3}} * \left(\frac{m_a}{A_c} \right)^2 \right) + \left(\frac{K_{up}}{2 * \rho_{a_3}} * \left(\frac{m_a}{A_e} \right)^2 \right) & \\
 - \left[\left(\frac{K_{Fs} + K_{rec}}{2 * \rho_{a_4}} * \left(\frac{m_a}{A_c} \right)^2 \right) \right] + \left(\frac{K_{do}}{2 * \rho_{a_3}} * \left(\frac{m_a}{A_e} \right)^2 \right) & \\
 + \left(\frac{K_{he}}{2 * \rho_{a_{56}}} * \left(\frac{m_a}{n_b * A_{fr}} \right)^2 \right) + \left(\frac{\alpha_{e6}}{2 * \rho_{a_4}} * \left(\frac{m_a}{A_c} \right)^2 \right) &
 \end{aligned} \tag{B-1}$$

Where K_{ts} , K_{Fsi} , K_{up} , K_{FS} , K_{FS} , K_{rec} , K_{do} , K_{he} and α_{e6} is the heat exchanger supports loss coefficient, fan inlet shroud/bell mouth loss coefficient, up-stream obstacle loss coefficient, fan static pressure rise coefficient, plenum recovery coefficient, down-stream obstacle loss coefficient, heat exchanger loss coefficient and outlet kinetic energy factor.

K_{rec} is the plenum recovery coefficient, and is given by Kröger (1998) as: $K_{rec} = \alpha_{eF} - K_{pl}$, where α_{eF} is the kinetic energy velocity distribution correction factor at the outlet of the fan and K_{pl} is the plenum loss coefficient. For an A-frame setup these parameters are not normally known but using experimental data, Kröger proves that $\alpha_{eF} = K_{pl}$. The recovery coefficient is therefor ignored further.

For the above equation, the following assumptions hold true: $\rho_{a1} \approx \rho_{a6} \approx \rho_{a2}$, $\rho_{a4} \approx \rho_{a3}$ and $\rho_{a6} \approx \rho_{a7}$, the frictional losses 6 and 7 are negligible and height at point 7 and 8 is the same, the kinetic energy factor α_{e6} and the heat exchanger loss coefficient K_{he} is reduced to $K_{he\theta}$.

B.2 MSACC draft equation

Adapting the above equation for the MSACC scheme in Figure B-2 below results in the following equation:

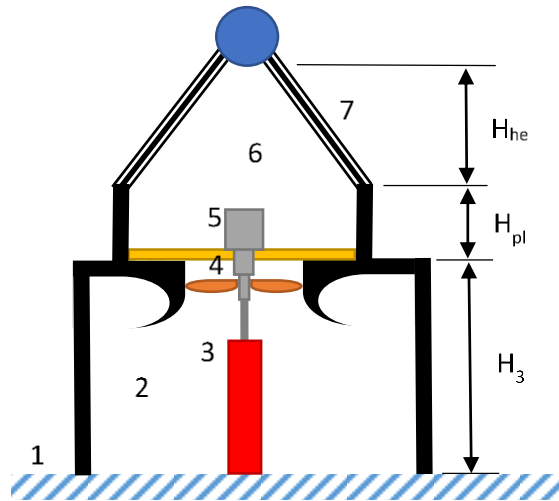


Figure B-2: MSACC control volume points (Adapted from Kröger, 1998)

$$\begin{aligned}
 0 \approx & \left(\frac{K_{ts}}{2 * \rho_{a1}} * \left(\frac{m_a}{A_2} \right)^2 \right) + \left(\frac{K_{Fsi}}{2 * \rho_{a3}} * \left(\frac{m_a}{A_c} \right)^2 \right) \\
 & + \left(\frac{K_{up}}{2 * \rho_{a3}} * \left(\frac{m_a}{A_e} \right)^2 \right) - \left[\left(\frac{K_{FS}}{2 * \rho_{a4}} * \left(\frac{m_a}{A_c} \right)^2 \right) \right] \\
 & + \left(\frac{K_{do}}{2 * \rho_{a4}} * \left(\frac{m_a}{A_e} \right)^2 \right) + \left(\frac{K_{\theta t}}{2 * \rho_{a67}} * \left(\frac{m_a}{A_{fr}} \right)^2 \right)
 \end{aligned} \tag{B-2}$$

The following simplifications are assumed for the equation above: there is no change in temperature ($T_{a_1} = T_{a_6}$, right-hand side is zero). The highest-pressure differential is less than 400 Pa , thus the air density can be assumed to be equal through the MSACC. $K_{\theta t}$ includes the losses across the heat exchanger and kinetic energy losses at the outlet elevation 7

B.3 MSACC parameters

B.3.1. The thermo-physical properties of air:

Air temperature	$T_a = 20 \text{ }^\circ\text{C}$
Density	$\rho_a = 1.2 \text{ kg/s}$
Ambient pressure	$P_a = 100 \text{ kPa}$

B.3.2. Upstream obstacles

MSACC supports dimensions (200x200x6 mm)	$d_{ts} = 0.2 \text{ m}$
MSACC number of supports	$n_{ts} = 4$
MSACC supports area	$A_2 = 9 \text{ m}^2$
MSACC supports drag coefficient (2D square)	$Cd_{ts} = 2.05$
Heat exchanger supports height	$H_{ts} = 2.4 \text{ m}$
Inlet screen distance from fan blade	$X_{ss} = 0.53 \text{ m}$
Total bottom safety screen area	$A_{ss} = 3.2 \text{ m}^2$
Ratio of inlet screen area to fan casing area (Taking the open area in account)	$\sigma_{si} = 0.7496$

B.3.3. MSACC B2-fan dimensions

Bell mouth casing diameter	$D_c = 1.526 \text{ m}$
Bell mouth casing area	$A_c = 1.829 \text{ m}^2$
Fan blade tip clearance	$t_F = 0.004 \text{ m}$
Fan hub diameter	$D_h = 0.628 \text{ m}$

B.3.4. Downstream obstacles

Support beam distance from fan blade	$X_{sb} = 0.32 \text{ m}$
Ratio of fan support area to fan casing area	$\sigma_{sb} = 0.246$
Plenum dimensions	
Semi-apex angle	$\theta = 30^\circ$
Plenum box dimensions	$1.9 \times 1.9 \times 0.5 \text{ m}$
Plenum height	1.83 m
Perforated plates area	$440 \times 350 \text{ mm}^2$

Mean perforated plate hole diameter	34.7 mm
Fin area	48x48 mm ²
Fin thickness	6 mm
Length of perforated plates (4 * (0.44 + 10 mm gap))	$L_{HEB} = 1.8$ m
Total frontal area of A-frame	$A_{fr} = 4.787$ m ²
Hypotenuse plenum length	$L_r = 2$ m

B.4 Determining the MSACC operating conditions

B.4.1. heat exchanger supports pressure loss coefficient

The loss coefficient due to the heat exchanger supports can be expressed as:

$$K_{ts} = Cd_{ts} * L_{ts} * d_{ts} * \frac{n_{ts}}{A_2} = 2.05 * 2 * 0.2 * 4 / = 0.364 \quad (B-3)$$

B.4.2. Up- and down-stream pressure loss coefficient

Using the following two diagrams (shown in Figure C-1) as portrayed by Kröger (1998), the obstacles pressure loss coefficient can be determined using the geometrical parameters. The parameters on the figures are defined as: A_c is bell mouth casing area, d_c is bell mouth casing diameter, x is the obstacles distance from the fan and A_{ob} is the obstacles area.

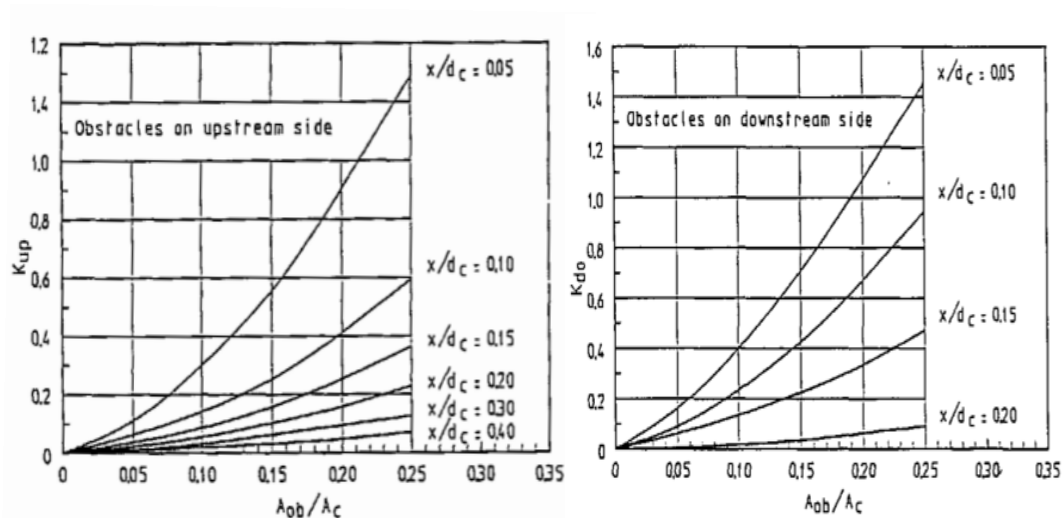


Figure B-3: Upstream and downstream obstacles loss coefficient (Kröger, 1998)

The following table shows the results of the up- and down-stream pressure loss coefficients:

Table B-1: Up- and down-stream pressure loss coefficients

Unit	Support beams		Safety screen		Fan bridge	
[-]	X_{ts}/D_c	0.347	X_{ss}/D_c	0.347	X_b/D_c	0.209
[m ²]	$A_{ob_{ts}}$	0.302	$A_{ob_{ss}}$	0.302	$A_{ob_{sb}}$	0.382
[-]			$A_{ob_{ss}}/A_c$	0.165	$A_{ob_{sb}}/A_c$	0.209
[-]	$K_{up_{ts}}$	0.3644	$K_{up_{ts}}$	0.080	$K_{down_{sb}}$	0.050

B.4.3. Contraction loss coefficient

The loss coefficient, K_θ is defined as the loss in total pressure divided by the inlet dynamic head.

$$K_\theta = \left[\left(\frac{1}{\sin(\theta_m)} - 1 \right) \left(\frac{1}{\sin(\theta_m)} - 1 \right) + 2K_{ci}^{0.5} \right] = 0.769 \quad (B-4)$$

B.4.4. Outlet loss coefficient

From equations and A-frame section view given in Chapter 3.2.4 and the geometrical parameters given, the outlet loss coefficient can be determined to be:

$$K_o = \left(\frac{A_{fr}}{A_{open}} \right)^2 \quad (B-5)$$

Table B-2: Outlet pressure loss coefficient

Throttle	100%	91.70%	83.3%	75.0%	66.70%	58.30%	50.0%
A_{open}	1.108	1.016	0.924	0.831	0.739	0.647	0.554
K_o	18.655	22.202	26.864	33.165	41.975	54.824	74.622

B.4.5. Heat exchanger pressure loss coefficient

By neglecting the entrance losses at an angle of θ , an approximate equation for total pressure loss of a perforated plate at an incidence angle of θ , the total inclined heat exchanger pressure loss is defined by the following equation:

$$K_{\theta t} = K_{he} + \left[\left(\frac{1}{\sin(\theta_m)} - 1 \right) \left(\frac{1}{\sin(\theta_m)} - 1 \right) + 2K_{ci}^{0.5} \right] + K_o + K_{dj} \quad (B-6)$$

Where, K_{he} is the total loss with airflow normal to the perforated plate with the guide fins. It should be noted that $K_{dj} = 0$ for the MSACC test setup.

B.5 MSACC Duty Point Sample Calculations

The following table is obtained from using the perforated static pressure tests conducted in the succeeding appendix with Equation B-9 to yield the heat exchanger inclined pressure loss coefficient.

Table B-3: Total heat exchanger pressure loss coefficient

Throttle	100%	91.70%	83.3%	75.0%	66.70%	58.30%	50.0%
K_{he}	24.416	29.632	37.855	48.230	61.909	81.467	119.019
$K_{\theta t}$	43.840	52.602	65.488	82.164	104.653	137.060	194.410

Using the MSACC draft equation and plotting it with the BS848 test results the operating point for the MSACC at the two speeds can be determined. This is plotted in the following figure below:

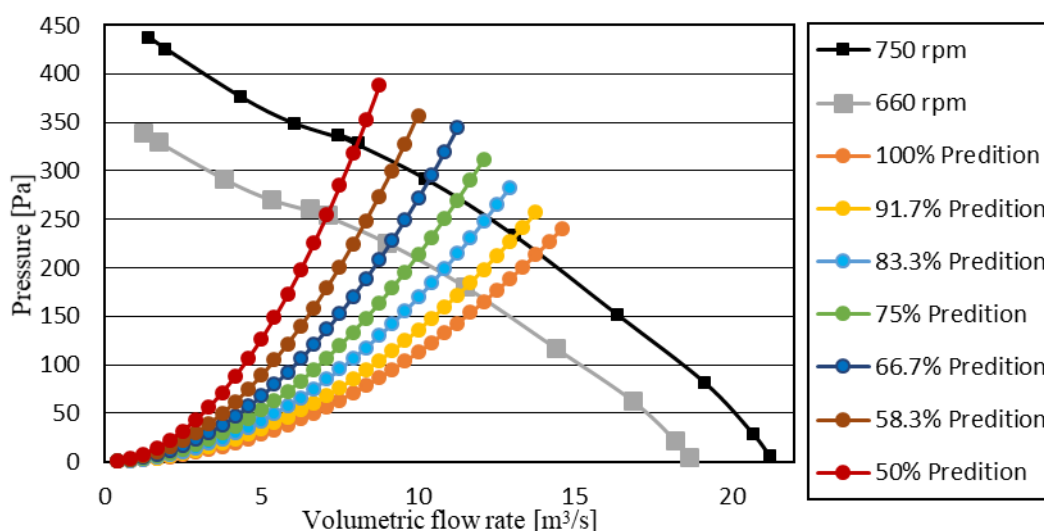


Figure B-4: MSACC predicted results for 7 throttle positions

APPENDIX C: INDUCED DRAFT WIND TUNNEL LAYOUT, EXPERIMENT DESCRIPTION AND CONDUCTED TEST RESULTS

C.1 Induced wind Tunnel Setup and calculation

Figure C-1 shows the induced draft wind tunnel used for heat exchanger guide fins and perforate plate tests and anemometer calibration.



Figure C-1: Atmospheric open loop induced wind tunnel

The induced wind tunnel test facility was used to determine the pressure differential of the perforated plates and to calibrate the anemometers. The layout of the wind tunnel is as follows.

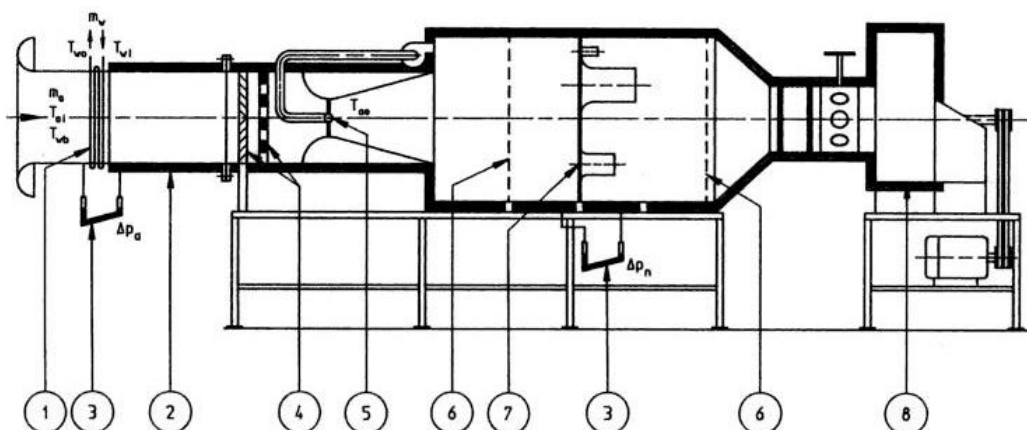


Figure C-2: Test wind tunnel layout (Kröger, 1998)

A radial fan (8) draws in air in the insulated wind tunnel. The static pressure difference over the heat exchanger is measured at points located at the duct wall (3) and the wet- and dry-bulb temperature is measured at (1). Sections 4 and 5 house air mixers and a venturi respectively. The airflow is determined by measuring the pressure drop across 5 elliptical nozzles mounted in a plate (7) located between two perforated plates (6). The property of the air entering the bell mouths are determined by measuring the static pressure (P_{up}) and temperature at section 6. The airflow is determined by measuring the pressure drop across the mounted nozzles (ΔP_n). The area of the bell mouth is given by A_n . Neglecting thermal expansion or contraction of the elliptical nozzles, mass flow rate is given by the following expression:

$$\dot{m} = C_n \phi_g Y A_n * (2 \rho_n \Delta P_n)^{0.5} \quad (C-1)$$

Where air expansion factor, approach velocity factor and nozzle coefficient of discharge is displayed by the symbol ϕ_g , Y and C_n respectively. C_n is a function of the Reynolds number and is determined by the following equations below:

For $30\,000 < Re_n < 100\,000$

$$C_n = 0.954803 + (6.37817 \cdot 10^{-7} Re_n) - (4.65394 \cdot 10^{-12} Re_n^2) + (1.33514 \cdot 10^{-17} Re_n^3) \quad (C-2)$$

For $100\,000 < Re_n < 350\,000$

$$C_n = 0.9758 + (1.08 \cdot 10^{-7} Re_n) - (1.6 \cdot 10^{-13} Re_n^2) \quad (C-3)$$

And if Re_n exceeds 350 000

$$C_n = 0.994 \quad (C-4)$$

In expression C-1, the air expansion factor (ϕ_g) is estimated by the following expression:

$$\phi_g = 1 - \frac{3 \Delta P_n}{4 P_{up} k_{air}} \quad (C-5)$$

Where $k_{air} = \left(\frac{c_p}{c_v}\right)_{air}$ is the specific heat of the fluid (air).

The approach velocity factor (Y) is described by the following equation:

$$Y = 1 + \left[0.5 \left(\frac{A_n}{A_{tus}}\right)^2\right] + \left[2 \left(\frac{A_n}{A_{tus}}\right)^2 \frac{\Delta P_n}{P_{up} k_{air}}\right] \quad (C-6)$$

From the mass flow rate, the volumetric flow rate can be determined using the following expression:

$$\dot{v} = \dot{m}/\rho \quad (C-7)$$

C.2 Air Properties calculations

The following calculations were used to determine the air properties for both wind tunnels (forced and induced) and MSACC test results.

Specific humidity is calculated by the following expression:

$$\begin{aligned} c_p = & (1.045356 \cdot 10^3) - (0.3161783 T_d) \\ & + (7.083814 \cdot 10^{-4} T_d^2) \\ & - (2.705209 \cdot 10^{-7} T_d^3) [kJ/kg K] \end{aligned} \quad (C-8)$$

Saturated vapour pressure (P_{sat}) is calculated at dry-bulb temp for temp between 0 and 30 °C is calculated using:

$$P_{sat} = \exp\left(\frac{17.438 T_w}{239.78 + T_w} + 6.4147\right) [Pa] \quad (C-9)$$

Enthalpy of water vapour at dry bulb temp is determined using:

$$hg = 2500,9 + 1,82 (T_d - 273.15) [kJ/kg] \quad (C-10)$$

The following equation gives the expression for enthalpy of saturated liquid water at dry bulb temp:

$$hf = \left(\left(\frac{T_w - 5}{30 - 5} \right) (125,74 - 21,2) \right) + 21,02 [kJ/kg] \quad (C-11)$$

Air Specific humidity is calculated using the following expression:

$$\omega_2 = \frac{0.622 p_{g2}}{p_2 - p_{g2}} \left[\frac{kg H_2O}{kg kg dry air} \right] \quad (C-12)$$

$$\omega_1 = \frac{c_p (T_d - T_{wb}) + (\omega_2 hg)}{hg - hf} \left[\frac{kg H_2O}{kg kg dry air} \right] \quad (C-13)$$

And air humidity ratio is determined using:

$$\phi = \frac{\omega_1 p_{sat}}{p_{g1} (0.622 + \omega_1)} \quad (C-14)$$

The Specific heat of water vapour is defined by the wet-bulb air temperature as:

$$hf = \left(\left(\frac{T_w - 5}{30 - 5} \right) (125,74 - 21,2) \right) + 21,02 \text{ [kJ/kg]} \quad (C-15)$$

Taking in account the air humidity, the air density is defined as:

$$\rho_{amb} = \frac{p_{atm}}{(R T_d (1 + 1,607858 * \omega_1))} \left[\frac{kg}{m^3} \right] \quad (C-16)$$

Where the gas constant is defined by:

$$R = 0,287042 \left[\frac{kJ}{kgK} \right] \quad (C-17)$$

C.3 Induced wind tunnel pressure transducers calibration

Calibration was required to standardised all sensors used in the induced wind tunnel test setup. It was completed to provide a reference point from which the readings could be taken. Four pressure transducers were used in the wind tunnel. The first pressure transducer was already calibrated to measure the difference between sea-level pressure (101,325 kPa) and the atmospheric pressure at the wind tunnel. Only the three pressure transducers in the wind tunnel required calibration.

During the calibration, piping was used to connect all three transducers to a single pressure point, which was read by a Betz Manometer. The pressure transducers were connected to either one of the positive or negative pressure inputs while the other was open to the atmosphere. Pressure was then applied inside the tube and slowly bled off. Measurements were taken at intervals until the pressure returned to atmospheric pressure. Most of results are reported in the following table:

Table C-1: Pressure transducer calibration values

Reading	Betz Manometer	Pressure Transducer 1 (Ch117 = Δp_a)	Pressure Transducer 2 (Ch118 = p_{up})	Pressure Transducer 3 (Ch119 = Δp_n)
Units	[Pa]	[V]	[V]	[V]
1	551.3	6.897	6.886	6.408
2	451.3	6.009	6.001	5.610
3	351.5	5.123	5.109	4.806
4	251.4	4.232	4.221	4.007
5	200.7	3.780	3.771	3.601
6	150.5	3.335	3.330	3.203
7	100.6	2.891	2.888	2.805
8	80.4	2.711	2.707	2.643
9	70.5	2.623	2.612	2.558

Plotting the values of Table 5-1 results in

. It depicts a linear relationship between pressure and voltage for all three transducers.

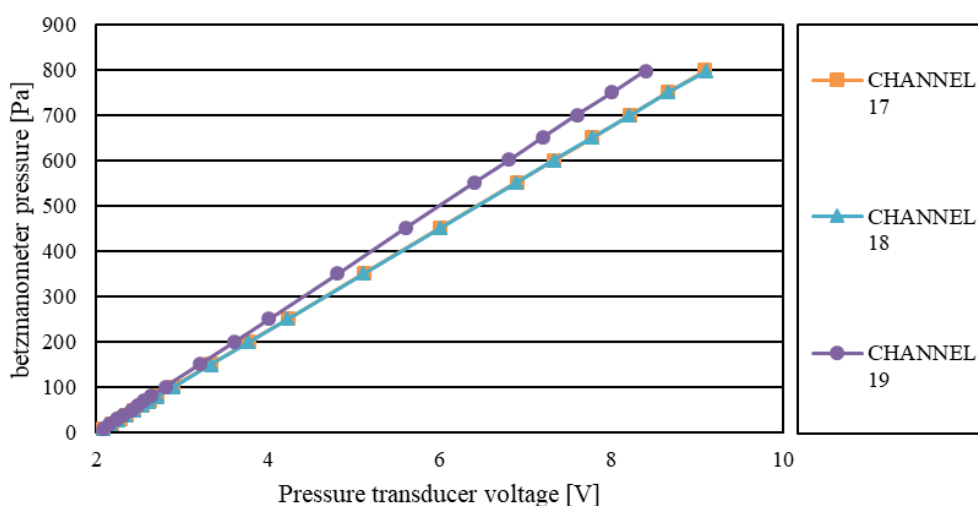


Figure C-3: Calibration curve for induced wind tunnel pressure transducers

From all the pressure reading values it is evident that these present a straight line; the calibration curve equation was calculated from this. The slope and the intercept values is tabulated in following table:

Table C-2: Pressure transducer calibration curve values

Transducer	(Ch17)	(Ch18) [V]	(Ch19)
Parameters	ΔP_a	P_{up}	ΔP_n
Slope	112.497	112.446	124.872

Intercept	-224.652	-224.576	-249.623
------------------	-----------------	----------	----------

The values in the table are used to convert the voltage reading into pressure by the following relation:

$$p = \text{Slope}_j V_j + \text{intercept}_j \text{ [Pa]} \quad (C-18)$$

Where V_j is the voltage reading of a particular pressure transducer (j) with its corresponding calibration slope and intercept.

C.4 Induced wind tunnel leakage test

A leakage test was conducted on the Induced wind tunnel. The test results and calculations are shown in the tables below: The pressure readings were taken using the AutoTran pressure transducers and using the calculation given in Appendix C.2, the air mass flow loss can be determined. The test and calculation results are tabulated below:

Table C-3: Leakage test results (test 2)

Data point/ measurement	P_{up}	ΔP_n	P_{atm}	Air density	Volumetric flow rate	Mass flow rate
Unit	[Pa]	[Pa]	[kPa]	[kg/m ³]	[m ³ /s] x 10 ⁻³	[kg/s] x 10 ⁻³
1	0	0	101.740	1.172	0	0
2	19.1	0.6	101.740	1.172	1.90	2.228
3	70	3.1	101.740	1.172	4.333	5.076
4	14.8	8.4	101.740	1.172	7.152	8.379
5	294.5	14	101.740	1.172	9.250	10.837
6	465.7	18.5	101.740	1.172	10.645	12.472
7	672.6	25.7	101.740	1.172	12.566	14.722
8	907.9	34.5	101.740	1.172	14.582	17.083

The mass flow rate loss can be expressed as a function of the static pressure (P_{up}) This is shown graphically below

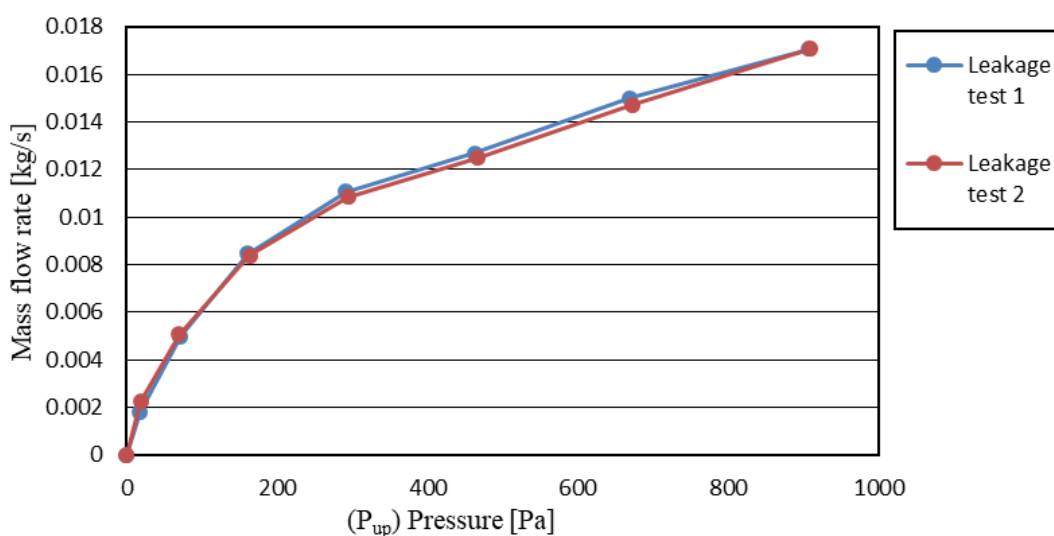


Figure C-4: Leakage test

By taking the average reading of the two tests conducted, poly-nominal curve can be used to describe the leakage as a function of P_{up} as given below:

$$\dot{m}_{loss} = (2 * 10^{-16} * P_{up}^5) - (5 * 10^{-13} P_{up}^4) + (5 * 10^{-10} * P_{up}^3) - (3 * 10^{-7} * P_{up}^2) + (9 * 10^{-5} * P_{up}) + 0.0002$$

C.5 Perforated plate porosity test

The following section shows the typical test results of the induced wind tunnel for the porosity test for sample perforated plates

Table C-4: 9 holes (35 mm diameter) Induced wind tunnel test results

Motor speed	Volumetric flow rate	Mass flow	ΔP_n	P_{up}	ΔP_a
Units	$[m^3/s]$	$[kg/s]$	$[Pa]$	$[Pa]$	$[Pa]$
3	0.0404	0.0462	0.2021	-0.7732	3.1724
6	0.0666	0.0762	0.5443	19.7617	17.4620
9	0.0917	0.1049	1.0248	53.5062	51.2435
12	0.1272	0.1455	1.9567	102.2859	99.2030
15	0.1612	0.1843	3.1206	163.3870	158.5870
20	0.2127	0.2432	5.3917	295.8551	295.6955
25	0.2678	0.3062	8.4943	461.7021	485.0391
30	0.3204	0.3663	12.1057	512.8379	525.8211
35	0.3675	0.4201	15.8786	512.8350	525.8206

Table C-5: 13 holes (35 mm diameter) Induced wind tunnel test results

Motor speed	Volumetric flow rate	Mass flow	ΔP_n	P_{up}	ΔP_a
Units	$[m^3/s]$	$[kg/s]$	$[Pa]$	$[Pa]$	$[Pa]$
3	0.0460	0.0525	0.2442	-2.0829	-3.7320
6	0.0713	0.0815	0.5864	18.4521	16.9024
9	0.0961	0.1099	1.0668	52.1966	50.6838
12	0.1315	0.1504	1.9988	100.9763	98.6434
15	0.1655	0.1892	3.1627	162.0773	158.0274
20	0.2169	0.2480	5.4338	294.5455	295.1359
25	0.2718	0.3108	8.5364	460.3924	484.4795
30	0.2988	0.3708	12.1478	511.5282	582.7258
35	0.3491	0.3942	11.5046	552.9639	673.7653

Table C-6: 17 holes (35 mm diameter) Induced wind tunnel test results

Motor speed	Volumetric flow rate	Mass flow	ΔP_n	P_{up}	ΔP_a
Units	$[m^3/s]$	$[kg/s]$	$[Pa]$	$[Pa]$	$[Pa]$
3	0.0700	0.0800	0.4338	1.0955	1.2884
6	0.1157	0.1323	1.1782	21.8101	21.5087
9	0.1740	0.1990	2.6378	56.7702	55.9191
12	0.1740	0.1990	2.6379	56.7703	55.9189
15	0.2940	0.3362	7.4244	168.0513	165.6339
20	0.3875	0.4431	12.8128	299.9918	298.1822
25	0.4852	0.5548	20.0317	475.8353	473.4732
30	0.5830	0.6666	27.2505	651.6788	648.7641
35	0.5821	0.6655	28.7353	689.4391	687.6019

Table C-7: 25 holes (35 mm diameter) Induced wind tunnel test results

Motor speed	Volumetric flow rate	Mass flow	ΔP_n	P_{up}	ΔP_a
Units	$[m^3/s]$	$[kg/s]$	$[Pa]$	$[Pa]$	$[Pa]$
3	0.1179	0.1349	1.2192	2.5621	1.7846
6	0.1757	0.2010	2.6871	21.8628	19.3921
9	0.2525	0.2888	5.4959	54.7281	49.4343
12	0.3282	0.3754	9.2256	101.1862	92.3929
15	0.4030	0.4610	13.8485	160.7233	147.4538
20	0.5338	0.6105	24.2028	292.7994	268.3772
25	0.6628	0.7580	37.1706	460.0474	424.1697
30	0.7945	0.9087	53.2516	664.8419	613.5794
35	0.8420	0.9630	50.3906	627.0207	578.0556

Table C-8: 33 holes (35 mm diameter) Induced wind tunnel test results

Motor speed	Volumetric flow rate	Mass flow	ΔP_n	P_{up}	ΔP_a
Units	$[m^3/s]$	$[kg/s]$	$[Pa]$	$[Pa]$	$[Pa]$
3	0.1235	0.1413	1.3291	1.2735	0.2411
6	0.2085	0.2385	3.7642	19.7202	14.7934
9	0.2996	0.3426	7.6975	51.6429	39.8391
12	0.3959	0.4528	13.3617	95.1875	74.2965
15	0.4960	0.5673	20.9125	153.3878	120.4636
20	0.6556	0.7498	36.3596	277.0018	217.9811
25	0.8135	0.9304	55.7818	436.4978	344.6363
30	0.9762	1.1164	80.0921	630.7647	496.0420
35	1.0857	1.2980	97.5268	772.3197	608.1284

Table C-9: 41 holes (35 mm diameter) Induced wind tunnel test results

Motor speed	Volumetric flow rate	Mass flow	ΔP_n	P_{up}	ΔP_a
Units	$[m^3/s]$	$[kg/s]$	$[Pa]$	$[Pa]$	$[Pa]$
3	0.1245	0.1424	1.3602	4.9299	2.5909
6	0.2231	0.2551	4.2993	21.7166	13.5244
9	0.3329	0.3807	9.4769	50.9019	32.6582
12	0.4422	0.5057	16.6419	93.5255	60.5937
15	0.5526	0.6320	25.8948	147.8358	96.4547
20	0.7326	0.8379	45.2947	265.9486	173.8952
25	0.9169	1.0487	70.7030	418.9068	274.3842
30	1.1016	1.2599	101.8170	604.7554	394.6458
35	1.2863	1.4711	132.9310	790.6039	514.9074

Table C-10: 49 holes (35 mm diameter) Induced wind tunnel test results

Motor speed	Volumetric flow rate	Mass flow	ΔP_n	P_{up}	ΔP_a
Units	$[m^3/s]$	$[kg/s]$	$[Pa]$	$[Pa]$	$[Pa]$
3	0.1218	0.1394	1.3018	3.7965	1.5227
6	0.2418	0.2766	5.0399	21.9311	11.8786
9	0.3535	0.4043	10.6689	48.6460	26.9093
12	0.4793	0.5481	19.5193	91.1283	50.7319
15	0.5988	0.6849	30.3566	142.8379	80.3044
20	0.7982	0.9129	53.6721	256.6695	144.9878
25	0.9989	1.1425	83.7792	403.0887	227.8683
30	1.1991	1.3715	120.5221	579.8499	331.0524
35	1.3978	1.5986	163.7185	783.5326	452.1976

Table C-11: 57 holes (35 mm diameter) Induced wind tunnel test results

Motor speed	Volumetric flow rate	Mass flow	ΔP_n	P_{up}	ΔP_a
Units	$[m^3/s]$	$[kg/s]$	$[Pa]$	$[Pa]$	$[Pa]$
3	0.1483	0.1700	1.9238	5.8913	2.1261
6	0.2476	0.2839	5.2918	19.7903	8.7108
9	0.3821	0.4380	12.4704	48.5806	22.3107
12	0.5077	0.5820	21.9252	86.4978	41.1427
15	0.6416	0.7355	34.8778	139.3500	67.0200
20	0.8532	0.9780	61.3724	248.9195	120.5742
25	1.0621	1.2175	94.8273	389.3325	189.2467
30	1.2788	1.4659	137.2829	561.5209	276.0788
35	1.4897	1.7076	186.3665	762.7777	377.1763

Table C-12: 65 holes (35 mm diameter) Induced wind tunnel test results

Motor speed	Volumetric flow rate	Mass flow	ΔP_n	P_{up}	ΔP_a
Units	$[m^3/s]$	$[kg/s]$	$[Pa]$	$[Pa]$	$[Pa]$
3	0.1329	0.1520	1.5440	3.8838	0.7212
6	0.2681	0.3066	6.1722	20.1978	7.3854
9	0.4024	0.4602	13.7774	48.0998	18.7806
12	0.5293	0.6054	23.7529	84.4056	33.8103
15	0.6650	0.7605	37.3473	135.3194	54.5516
20	0.8856	1.0129	65.9301	241.1772	97.6092
25	1.1120	1.2718	103.6383	380.8921	155.1227
30	1.3343	1.5260	149.0810	546.7474	225.1105
35	1.5576	1.7815	203.2796	745.2184	308.2222

Table C-13: 73holes (35 mm diameter) Induced wind tunnel test results

Motor speed	Volumetric flow rate	Mass flow	ΔP_n	P_{up}	ΔP_a
Units	$[m^3/s]$	$[kg/s]$	$[Pa]$	$[Pa]$	$[Pa]$
3	0.1329	0.1520	1.5440	3.8838	0.7212
6	0.2681	0.3066	6.1722	20.1978	7.3854
9	0.4024	0.4602	13.7774	48.0998	18.7806
12	0.5293	0.6054	23.7529	84.4056	33.8103
15	0.6650	0.7605	37.3473	135.3194	54.5516
20	0.8856	1.0129	65.9301	241.1772	84.6092
25	1.1669	1.3346	114.0414	373.9938	133.5721
30	1.4038	1.6055	164.9877	539.7734	194.1080
35	1.6369	1.8722	224.4876	735.2087	263.3711

C.6 Induced wind tunnel distance Anemometer calibration

The ideal distance between the anemometer and the perforated plate was determined by varying the distance between them in the induced and forced wind tunnel setups as portrayed by the following Figure C-5 and Figure C-8. The heat exchanger model was the same setup as in the MSACC with the guide fins and metal frame box installed. The anemometer was placed at a determined distance (indicated by the green arrow) from the perforated plate.

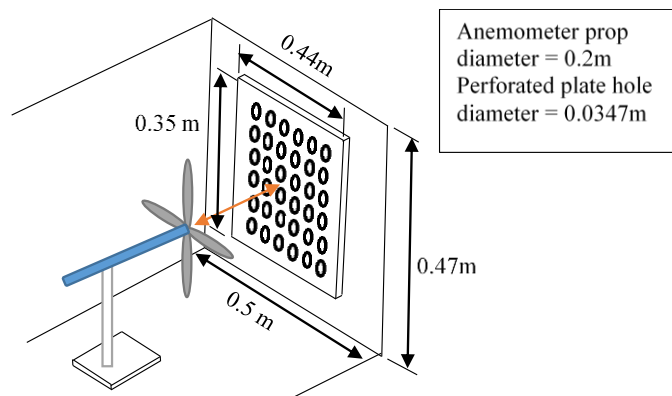


Figure C-5: Induced wind tunnel - distance Anemometer calibration test setup

The Figure above is a cutaway view of the induced wind tunnel distance test setup, which describes the diameter of the anemometer propeller, wind tunnel test chamber area and the general dimensions of the perforated plate (this is the same for both induced and forced wind tunnel distance test). The two centres of the perforated plate and anemometer was aligned before each test.

Eight predetermined distances were chosen (50, 100, 150, 200, 300, 400 mm) to make the test setup identical to the MSACC anemometer distance setup. The tabulated test results are displayed below for the Pressure data readings and anemometer voltage readings in Table C-14 and Table C-15 respectively.

Table C-14: Induced wind tunnel - Pressure data readings and calculated results (200 mm data point at open throttle position)

Data Point	\dot{V}	\dot{m}	V_n	P_a	P_{up}	ΔP_n
motor speed [Hz]/ Unit	[m³/s]	[kg/s]	[m/s]	[Pa]	[Pa]	[Pa]
3	0.031	0.037	1.851	2.379	5.214	2.593
5	0.054	0.064	3.153	6.472	13.664	6.961
10	0.114	0.134	6.416	25.512	55.823	27.623
15	0.174	0.205	9.682	57.139	126.121	62.053
20	0.234	0.276	13.008	102.281	222.268	110.363
25	0.295	0.347	16.331	160.419	347.689	173.240
30	0.355	0.418	19.592	230.112	496.801	249.012
35	0.416	0.490	22.960	315.273	676.574	340.294
40	0.476	0.561	26.299	412.886	876.438	444.250

Table C-15: Induced wind tunnel - Anemometer distance voltage readings (open throttle position)

Motor speed / distance	50 mm	100 mm	150 mm	200 mm	300 mm	400 mm
3 Hz	0.048	0.055	0.056	0.058	0.054	0.054
5 Hz	0.080	0.089	0.093	0.098	0.093	0.093
10 Hz	0.173	0.180	0.189	0.198	0.191	0.165
15 Hz	0.243	0.286	0.296	0.307	0.294	0.250
20 Hz	0.343	0.373	0.388	0.402	0.372	0.338
25 Hz	0.397	0.474	0.486	0.499	0.483	0.418
30 Hz	0.509	0.588	0.594	0.600	0.562	0.507
35 Hz	0.616	0.694	0.693	0.694	0.685	0.599
40 Hz	0.742	0.809	0.813	0.816	0.801	0.676

Plotting the distance data of the two tables results in Figure C-7. The 200 mm distance shows the highest voltage to mass flow rate ratio.

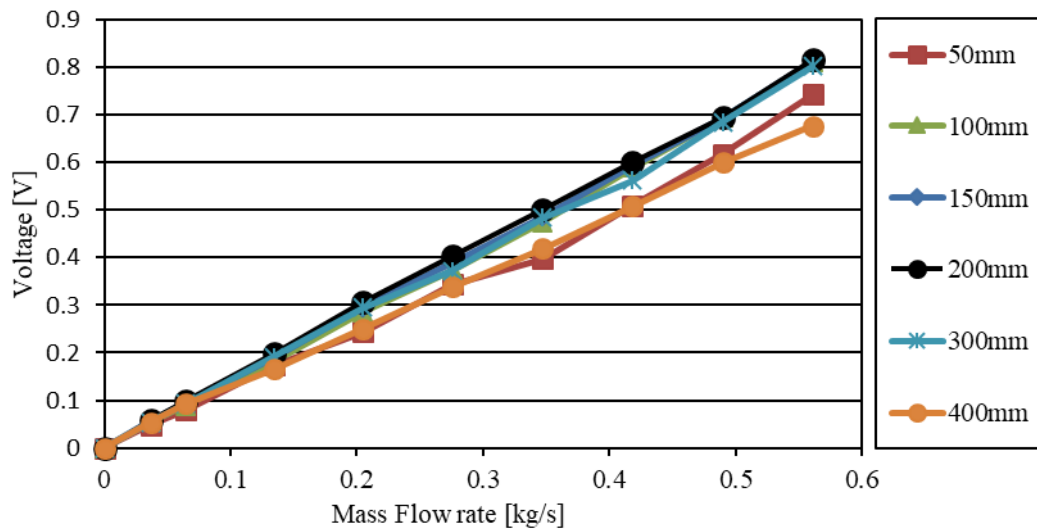


Figure C-6: Open throttle position distance anemometer measurement for induced wind tunnel

C.7 Forced wind tunnel distance Anemometer calibration

A forced wind tunnel was built to determine the relationship between the volumetric flow rate, pressure differential across the perforated plate and the anemometer voltage reading as shown in the figures below:



Figure C-7: Forced wind tunnel

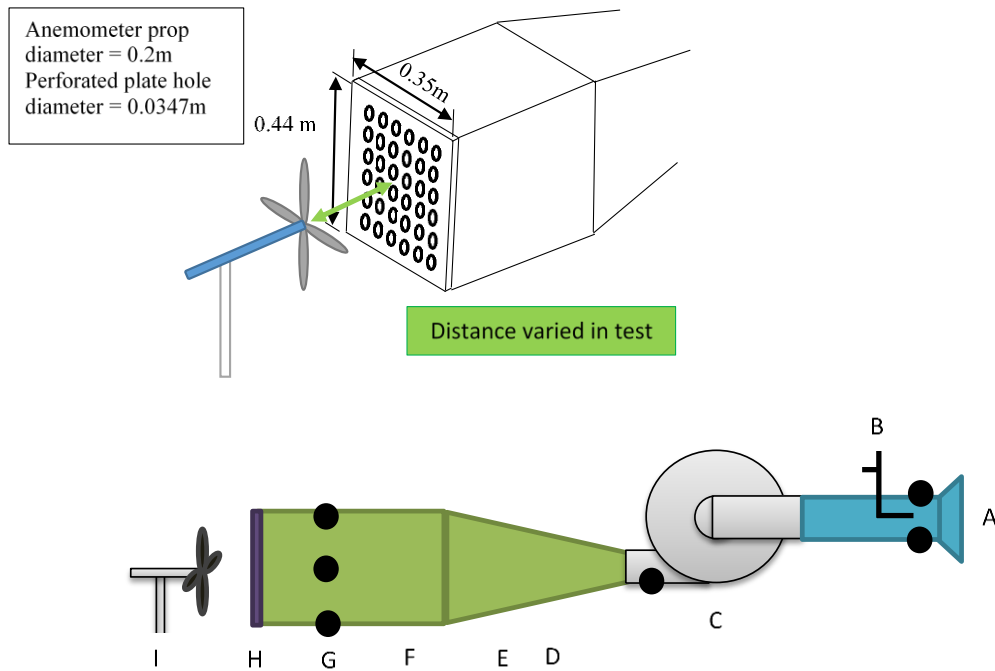


Figure C-8: Forced wind tunnel distance Anemometer calibration setup

Wind tunnel components:

- A. Bell mouth with static pressure reading points.
- B. Inlet pitot tube.
- C. Blower fan
- D. Settling chamber.
- E. Air flow development chamber.
- F. Static pressure reading points.
- G. Perforated plate.
- H. Test anemometer.

Just as the induced wind tunnel, the distance of the anemometer was varied to establish the open atmosphere conditions condition which is experienced at the MSACC test bench and to correlate the two test bench results. The 50 mm distance was discarded as it was deemed too close. The results of the tests conducted are given by the following figures below:

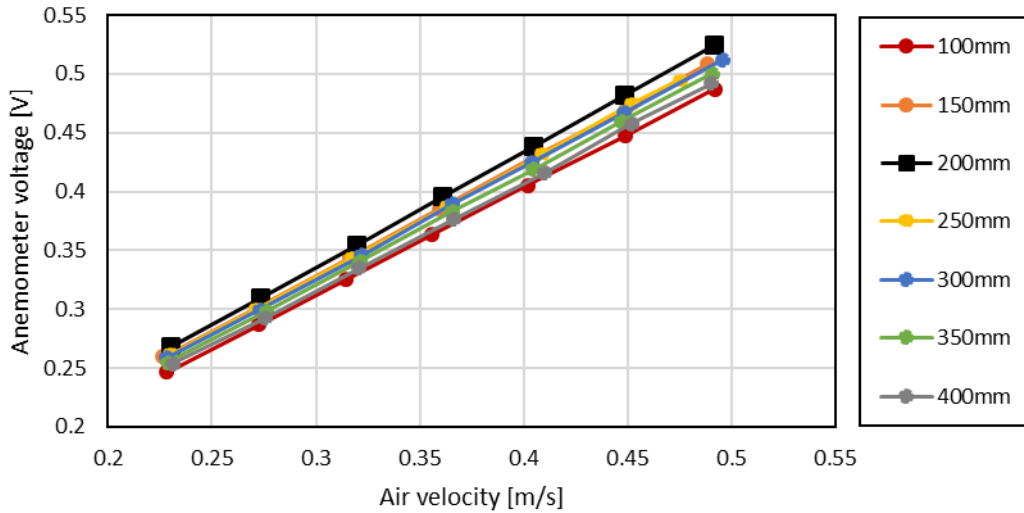


Figure C-9: Open throttle position distance anemometer measurement for forced wind tunnel

Just as the induced wind tunnel test results, the forced wind tunnel test results show that the 200 mm distance has the highest anemometer voltage readings. The difference in air velocity is due to the coalescence of the perforate plates individual jets; this can be seen between 50-200 mm. Downstream of 200 mm the coalesced jet streams kinetic energy reduces with distance due to expansion of the jet streams. The forced draft wind tunnel setup closely matched the outlet anemometer setup of the MACC. A calibration test was executed using the 200 mm distance to determine the anemometer velocity relationship with the static pressure differential over the perforated plate and the volumetric flow rate through the perforated plate. This was used to determine the outlet volumetric flow rate and static pressure distribution across the MSACC A-frame. The two figures below display the results obtained from the tests.

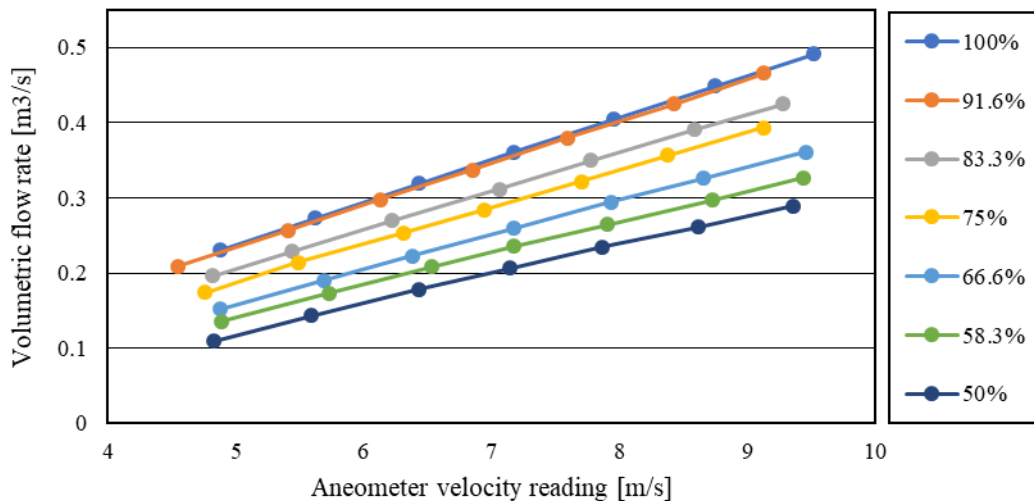


Figure C-10: Throttle position - anemometer velocity voltage vs static pressure

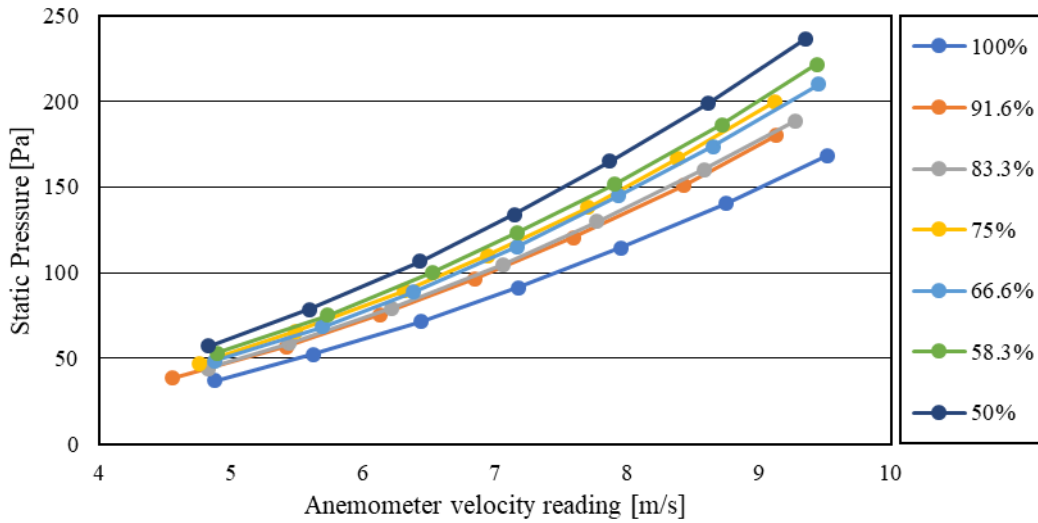


Figure C-11: Throttle position - anemometer velocity vs static pressure

The following tables are the produced from the trend-curves of the two figures above. The constants C3, C2, C1 and B are used in the following equations to determine the volumetric flow rate and pressure differential of the perforated plate (given the anemometer’s velocity and perforate plate throttle position) respectively:

$$\dot{V} = B3 \cdot V^3 + B2 \cdot V^2 + B1 \cdot V + A \left[\frac{m^3}{s} \right] \quad (C-19)$$

$$\Delta P = D3 \cdot V^3 + D2 \cdot V^2 + D1 \cdot V + C \left[\frac{m^3}{s} \right] \quad (C-20)$$

Table C-16: Outlet perforated plate anemometer velocity to volumetric flow rate trend-curve conversion constants

Anemometer velocity to Volumetric flow rate				
Throttle / constants	100%	91.6%	83.3%	75%
B3	0.00005	0.00003	-0.00004	0.00027
B2	-0.00137	-0.00074	0.00064	-0.00574
B1	0.06775	0.06128	0.04815	0.09001
A	-0.07343	-0.05818	-0.04586	-0.15270
Throttle / constants	66.6%	58.3%	50%	
B3	-0.00003	0.00017	0.00020	
B2	0.00013	-0.00436	-0.00542	
B1	0.04909	0.07714	0.08468	
A	-0.08724	-0.15770	-0.19613	

Table C-17: Outlet perforated plate anemometer velocity to static pressure trend-curve conversion constants

Anemometer velocity to perforate plate Pressure differential				
Throttle / constants	100%	91.6%	83.3%	75%
D3	0.00832	0.04724	-0.05916	0.04598
D2	1.82686	1.54984	3.63343	1.88615
D1	0.63960	2.82317	-9.71233	1.94837
C	-10.39932	-10.94605	13.35485	-9.64440
Throttle / constants	66.6%	58.3%	50%	
D3	-0.12727	0.03280	-0.09721	
D2	5.39794	2.12840	5.02487	
D1	-21.81402	1.27662	-16.53602	
C	41.25769	-7.78900	30.99118	

C.8 Chosen Perforated Plate Throttle Test Results

This final section of Appendix B presents the test results and calculated pressure loss coefficient of the various throttle positions of the chosen perforated plate.

Table C-18: 100% throttle (Right) and 91.7% throttle (Left)

Delta Pressure	Bell mouth Volumetric flow rate	Pressure loss coefficient	Delta Pressure	Bell mouth Volumetric flow rate	Pressure loss coefficient
[Pa]	[m³/s]	[-]	[Pa]	[m³/s]	[-]
37.1442	0.2302	24.4618	38.5482	0.2088	30.8544
52.3068	0.2733	24.4376	56.9055	0.2565	30.1875
71.6315	0.3195	24.4879	75.5792	0.2982	29.6627
91.2200	0.3608	24.4597	96.3417	0.3375	29.5202
114.4773	0.4045	24.4136	120.5882	0.3799	29.1660
140.2962	0.4486	24.3256	150.6967	0.4253	29.0789
168.4395	0.4916	24.3233	180.0023	0.4658	28.9532
Porosity	0.2385	24.4156	Porosity	0.2187	29.6319

Table C-19: 83.3% throttle (Right) and 75% throttle (Left)

Delta Pressure	Bell mouth Volumetric flow rate	Pressure loss coefficient	Delta Pressure	Bell mouth Volumetric flow rate	Pressure loss coefficient
[Pa]	[m³/s]	[-]	[Pa]	[m³/s]	[-]
44.2458	0.1966	39.9596	47.1673	0.1741	54.3250
58.5721	0.2288	39.0531	65.7787	0.2139	50.1943
79.1347	0.2693	38.0765	89.3103	0.2535	48.5137
104.7525	0.3114	37.7079	109.8575	0.2845	47.3597
129.8331	0.3495	37.1007	138.0622	0.3218	46.5168
160.1070	0.3904	36.6527	166.5304	0.3569	45.6169
188.6927	0.4251	36.4364	199.8394	0.3933	45.0827
Porosity	0.1988	37.8553	Porosity	0.1789	48.2299

Table C-20: 66% throttle (Right) and 58.3% throttle (Left)

Delta Pressure	Bell mouth Volumetric flow rate	Pressure loss coefficient	Delta Pressure	Bell mouth Volumetric flow rate	Pressure loss coefficient
[Pa]	[m³/s]	[-]	[Pa]	[m³/s]	[-]
48.5119	0.1514	73.8272	53.2818	0.1354	101.3615
68.3438	0.1903	65.8516	75.2937	0.1729	87.9251
88.6128	0.2226	62.4079	100.1892	0.2078	80.9772
115.3385	0.2594	59.8394	123.3367	0.2351	77.8918
144.7149	0.2946	58.1818	151.3968	0.2642	75.6872
173.6638	0.3258	57.1023	186.4742	0.2967	73.9031
209.9849	0.3613	56.1540	221.5122	0.3265	72.5197
Porosity	0.1590	61.9092	Porosity	0.1391	81.4665

Table C-21: 50% throttle

Delta Pressure	Bell mouth Volumetric flow rate	Pressure loss coefficient
[Pa]	[m³/s]	[-]
57.2790	0.1092	167.6789
78.5676	0.1433	133.5461
106.5453	0.1786	116.5537
133.7911	0.2062	109.8161
164.9075	0.2345	104.6273
198.7932	0.2608	101.9778
236.5620	0.2889	98.9338
Porosity	0.1193	119.0191

APPENDIX D: MSACC TEST DATA

The following appendix presents the recorded data of the test results of the MSACC for only one data set for the two fan speeds and from 50% till 91.6% throttle.

D.1 Inlet velocity distribution

This section shows typical readings of inlet anemometers for the (six anemometers only) and all values are in m/s .

Table D-1: 660 rpm at 50% throttle

Anemometers /data set	Units	1	2	3	4	5	6
1	[m/s]	4.931	4.413	5.334	5.038	4.604	5.476
2	[m/s]	5.017	4.460	5.216	4.867	4.576	5.466
3	[m/s]	4.950	4.474	5.255	4.966	4.572	5.575
4	[m/s]	4.891	4.602	5.318	4.870	4.613	5.502

Table D-2: 750 rpm at 50% throttle

Anemometers /data set	Units	1	2	3	4	5	6
1	[m/s]	6.117	5.792	6.431	5.668	6.063	6.697
2	[m/s]	6.046	5.634	6.361	5.757	6.112	6.759
3	[m/s]	6.140	5.749	6.578	5.687	6.267	6.910
4	[m/s]	6.119	5.801	6.629	5.749	6.362	6.900

Table D-3: 660 rpm at 58.3% throttle

Anemometers /data set	Units	1	2	3	4	5	6
1	[m/s]	5.459	4.656	5.720	5.193	5.176	5.908
2	[m/s]	5.189	4.681	5.654	5.405	4.994	5.770
3	[m/s]	5.461	4.685	5.601	5.219	5.171	5.874
4	[m/s]	5.465	4.586	5.648	5.183	5.098	5.902

Table D-4: 660 rpm at 66% throttle

Anemometers /data set	Units	1	2	3	4	5	6
1	[m/s]	5.835	5.124	6.049	5.509	5.458	6.176
2	[m/s]	5.769	4.949	6.130	5.673	5.559	6.171
3	[m/s]	5.769	4.949	6.130	5.673	5.559	6.171
4	[m/s]	5.797	5.081	6.045	5.594	5.612	6.199

Table D-5: 750 rpm at 66% throttle

Anemometers /data set	Units	1	2	3	4	5	6
1	[m/s]	6.380	6.552	7.315	6.682	6.368	7.311
2	[m/s]	6.184	6.355	6.907	6.630	6.356	7.176
3	[m/s]	6.426	6.236	6.912	6.824	6.413	7.240
4	[m/s]	6.366	6.197	6.918	6.640	6.376	7.210

Table D-6: 660 rpm at 75% throttle

Anemometers /data set	Units	1	2	3	4	5	6
1	[m/s]	6.024	5.258	6.454	5.995	5.984	6.516
2	[m/s]	6.192	5.333	6.435	5.862	5.963	6.517
3	[m/s]	6.161	5.406	6.602	6.118	5.808	6.517
4	[m/s]	6.084	5.394	6.498	5.926	5.880	6.442

Table D-7: 660 rpm at 83.3% throttle

Anemometers /data set	Units	1	2	3	4	5	6
1	[m/s]	6.557	5.681	6.783	6.150	6.279	6.862
2	[m/s]	6.525	5.587	6.825	6.168	6.224	6.804
3	[m/s]	6.507	5.636	6.770	6.343	6.270	6.866
4	[m/s]	6.503	5.641	6.747	6.266	6.245	6.802

Table D-8: 750 rpm at 83.3% throttle

Anemometers /data set	Units	1	2	3	4	5	6
1	[m/s]	7.382	6.805	7.156	7.3962	7.0431	7.7507
2	[m/s]	7.644	6.799	7.729	7.3036	7.2988	7.2667
3	[m/s]	7.569	6.950	8.041	7.4761	7.1479	7.5730
4	[m/s]	7.546	6.749	7.895	7.4805	7.0423	7.3205

Table D-9: 660 rpm at 91.6% throttle

Anemometers /data set	Units	1	2	3	4	5	6
1	[m/s]	7.499	6.602	7.864	7.047	7.088	7.733
2	[m/s]	7.427	6.726	7.862	7.008	7.084	7.758
3	[m/s]	7.427	6.726	7.862	7.008	7.084	7.758
4	[m/s]	7.385	6.591	7.792	6.943	7.070	7.732

Table D-10: 750 rpm at 100% throttle

Anemometers /data set	Units	1	2	3	4	5	6
1	[m/s]	7.782	7.541	8.244	7.365	7.707	8.112
2	[m/s]	7.933	7.425	8.360	7.483	7.577	8.136
3	[m/s]	7.817	7.359	8.218	7.306	7.541	8.175
4	[m/s]	7.718	7.412	8.235	7.546	7.574	8.156

Table D-11: 660 rpm at 100% throttle

Anemometers /data set	Units	1	2	3	4	5	6
1	[m/s]	7.694	6.825	8.230	7.307	7.460	8.018
2	[m/s]	7.741	6.793	8.040	7.240	7.344	8.020
3	[m/s]	7.741	6.793	8.040	7.240	7.344	8.020
4	[m/s]	7.680	6.916	8.139	7.267	7.305	8.009

D.2 Outlet velocity distribution

This section shows typical readings of outlet anemometers and all values are in *m/s*.

Table D-12: Typical Outlet velocity readings - 660 rpm at 50% throttle

Anemometers /data set	11	12	13	14	7	8	9	10
Units	[m/s]	[m/s]	[m/s]	[m/s]	[m/s]	[m/s]	[m/s]	[m/s]
Row 1	8.147	5.489	7.218	6.419	6.438	7.846	5.648	7.822
Row 2	7.219	6.653	7.530	6.340	7.557	6.911	5.975	8.137
Row 3	7.456	6.583	7.955	4.554	6.706	5.650	7.777	8.374
Row 4	7.687	7.835	7.875	7.249	6.216	6.992	8.510	6.992

Table D-13: Typical Outlet velocity readings - 750 rpm at 50% throttle

Anemometers /data set	11	12	13	14	7	8	9	10
Units	[m/s]	[m/s]	[m/s]	[m/s]	[m/s]	[m/s]	[m/s]	[m/s]
Row 1	9.207	8.069	8.142	8.220	7.498	8.383	5.819	8.458
Row 2	8.100	6.679	9.199	8.115	9.370	7.396	6.409	8.712
Row 3	8.720	6.066	8.974	7.376	8.311	6.166	7.982	8.644
Row 4	9.423	8.802	8.941	8.018	7.996	8.003	8.397	8.585

Table D-14: Typical Outlet velocity readings - 660 rpm at 58.3% throttle

Anemometers /data set	11	12	13	14	7	8	9	10
Units	[m/s]	[m/s]	[m/s]	[m/s]	[m/s]	[m/s]	[m/s]	[m/s]
Row 1	8.374	7.985	6.634	7.222	6.437	7.860	6.280	8.526
Row 2	7.195	6.174	7.034	6.591	7.349	6.789	5.738	8.671
Row 3	7.662	6.346	7.709	6.512	6.598	6.165	7.368	8.706
Row 4	7.695	5.820	7.662	6.308	5.931	6.747	6.970	6.737

Table D-15: Typical Outlet velocity readings - 660 rpm at 66% throttle

Anemometers /data set	11	12	13	14	7	8	9	10
Units	[m/s]	[m/s]	[m/s]	[m/s]	[m/s]	[m/s]	[m/s]	[m/s]
Row 1	8.050	7.690	5.956	7.528	6.389	7.252	5.777	8.002
Row 2	6.658	6.305	7.390	7.416	8.032	7.113	6.092	8.467
Row 3	7.809	5.920	7.582	7.258	6.895	6.688	7.075	8.215
Row 4	7.547	7.118	7.334	7.502	5.868	6.381	6.841	6.442

Table D-16: Typical Outlet velocity readings - 750 rpm at 66% throttle

Anemometers /data set	11	12	13	14	7	8	9	10
Units	[m/s]	[m/s]	[m/s]	[m/s]	[m/s]	[m/s]	[m/s]	[m/s]
Row 1	8.417	7.051	7.114	8.093	7.475	7.440	4.743	7.784
Row 2	7.888	6.069	8.286	7.302	8.498	7.246	5.760	8.504
Row 3	8.850	5.862	8.289	7.093	7.081	6.759	7.207	8.922
Row 4	8.888	8.300	8.220	6.624	6.191	7.446	8.252	7.804

Table D-17: Typical Outlet velocity readings - 660 rpm at 75% throttle

Anemometers /data set	11	12	13	14	7	8	9	10
Units	[m/s]	[m/s]	[m/s]	[m/s]	[m/s]	[m/s]	[m/s]	[m/s]
Row 1	7.754	7.222	6.057	7.383	5.293	6.869	5.160	7.367
Row 2	6.882	6.121	7.319	8.922	7.405	6.843	5.741	7.848
Row 3	7.256	5.570	7.065	6.938	6.915	6.160	6.529	8.079
Row 4	6.738	6.543	6.944	6.503	5.688	6.175	6.698	6.293

Table D-18: Typical Outlet velocity readings - 660 rpm at 83.3% throttle

Anemometers /data set	11	12	13	14	7	8	9	10
Units	[m/s]	[m/s]	[m/s]	[m/s]	[m/s]	[m/s]	[m/s]	[m/s]
Row 1	7.455	7.106	5.833	7.111	6.180	6.816	4.678	6.916
Row 2	6.911	5.894	7.144	7.101	7.124	6.605	5.585	7.686
Row 3	7.250	5.741	6.947	6.919	6.783	6.103	6.366	8.200
Row 4	6.654	6.735	6.801	6.381	5.145	6.209	7.035	5.890

Table D-19: Typical Outlet velocity readings - 750 rpm at 83.3% throttle

Anemometers /data set	11	12	13	14	7	8	9	10
Units	[m/s]	[m/s]	[m/s]	[m/s]	[m/s]	[m/s]	[m/s]	[m/s]
Row 1	8.179	7.147	6.766	8.228	7.267	7.234	4.820	7.462
Row 2	7.922	6.180	8.273	8.039	8.420	7.096	5.897	8.720
Row 3	8.618	5.547	7.775	7.747	8.122	6.309	6.563	8.433
Row 4	8.220	7.595	7.894	7.339	6.627	6.763	7.171	7.389

Table D-20: Typical Outlet velocity readings - 660 rpm at 91.6% throttle

Anemometers /data set	11	12	13	14	7	8	9	10
Units	[m/s]	[m/s]	[m/s]	[m/s]	[m/s]	[m/s]	[m/s]	[m/s]
Row 1	7.593	7.206	5.612	7.368	6.632	6.800	4.791	7.169
Row 2	7.943	6.072	7.175	7.100	7.179	6.459	6.377	8.499
Row 3	7.943	6.072	7.175	7.100	7.179	6.459	6.377	8.499
Row 4	6.879	7.592	7.666	5.897	5.251	6.271	7.308	6.449

Table D-21: Typical Outlet velocity readings - 660 rpm at 100% throttle

Anemometers /data set	11	12	13	14	7	8	9	10
Units	[m/s]	[m/s]	[m/s]	[m/s]	[m/s]	[m/s]	[m/s]	[m/s]
Row 1	7.917	7.322	5.455	7.263	6.728	6.653	5.247	7.743
Row 2	7.762	6.052	6.916	7.085	6.844	6.178	6.298	8.431
Row 3	7.762	6.052	6.916	7.085	6.844	6.178	6.298	8.431
Row 4	6.616	7.394	7.244	5.936	5.109	6.211	7.335	6.030

Table D-22: Typical Outlet velocity readings - 750 rpm at 100% throttle

Anemometers /data set	11	12	13	14	7	8	9	10
Units	[m/s]	[m/s]	[m/s]	[m/s]	[m/s]	[m/s]	[m/s]	[m/s]
Row 1	8.134	7.245	5.871	7.424	6.998	6.942	4.780	7.551
Row 2	7.587	5.841	7.184	7.458	7.467	6.116	5.735	8.176
Row 3	8.365	5.676	7.284	7.533	7.471	6.028	6.305	8.255
Row 4	7.558	7.649	7.542	6.866	6.314	6.186	7.335	6.727

D.3 A-frame outlet pressure distribution 660 rpm

The following tables uses the pressure and velocity calibration data of the anemometer distance test to give a distribution of pressure

Table D-23: Exit A-frame distribution of static pressure - typical readings (Throttle 50% - 75% -at 660 rpm)

		West/Left				East/Right					
		11	12	13	14	7	8	9	10	Right	Left
Units		[Pa]	[Pa]	[Pa]	[Pa]	[Pa]	[Pa]	[Pa]	[Pa]		
50.0%	Row 1	184.326	174.726	123.622	134.198	107.070	152.886	84.666	168.609	Average Pressure [Pa]	
	Row 2	128.375	122.664	156.439	132.788	162.192	121.019	102.722	179.354	2319.236	2178.206
	Row 3	144.611	116.060	170.778	107.846	119.600	76.624	159.181	195.415	Press distribution [Pa]	
	Row 4	156.627	163.143	164.902	138.131	99.023	127.802	194.236	127.804	144.952	136.138
58.3%	Row 1	168.195	159.313	112.612	122.219	97.590	139.256	77.171	153.676	Average Pressure [Pa]	
	Row 2	116.928	111.743	142.506	120.938	147.779	110.250	93.640	163.590	2113.267	1985.712
	Row 3	131.700	105.750	155.673	98.294	108.962	69.769	145.018	178.509	Press distribution [Pa]	
	Row 4	142.678	148.652	150.267	125.797	90.277	116.408	177.408	116.410	132.079	124.107
66.7%	Row 1	159.301	150.785	105.424	114.803	90.776	131.395	71.067	145.356	Average Pressure [Pa]	
	Row 2	109.638	104.575	134.550	113.553	139.658	103.118	86.938	154.892	1989.722	1865.247
	Row 3	124.047	98.726	147.280	91.461	101.860	64.048	136.985	169.130	Press distribution [Pa]	
	Row 4	134.717	140.502	142.064	118.294	83.677	109.130	168.085	109.132	124.358	116.578
75.0%	Row 1	162.761	154.013	108.199	117.597	93.530	134.297	73.645	148.466	Average Pressure [Pa]	
	Row 2	112.420	107.349	137.489	116.343	142.669	105.890	89.679	158.224	2036.596	1912.444
	Row 3	126.886	101.494	150.430	94.217	104.631	66.453	139.956	172.933	Press distribution [Pa]	
	Row 4	137.658	143.526	145.114	121.101	86.401	111.910	171.847	111.912	127.287	119.528

Table D-24: Exit A-frame distribution of static pressure - typical readings (Throttle 83% - 100% -at 660 rpm)

		West/Left				East/Right					
		11	12	13	14	7	8	9	10	Right	Left
Units		[Pa]	[Pa]	[Pa]	[Pa]	[Pa]	[Pa]	[Pa]	[Pa]		
83.3%	Row 1	116.411	110.142	67.767	106.938	76.233	93.193	46.823	103.296	Average Pressure [Pa]	
	Row 2	96.579	74.344	105.720	102.441	108.036	89.816	63.696	126.689	1532.738	1415.375
	Row 3	116.551	73.335	98.876	95.540	101.955	76.903	81.540	140.108	Press distribution [Pa]	
	Row 4	96.059	90.279	99.291	82.466	56.280	79.130	105.553	66.125	95.796	88.461
91.7%	Row 1	113.894	107.786	66.838	104.672	75.007	91.363	46.428	101.138	Average Pressure [Pa]	
	Row 2	94.635	73.186	103.489	100.309	105.738	88.103	62.901	123.957	1502.495	1389.527
	Row 3	114.031	72.212	96.857	93.631	99.838	75.652	80.122	137.199	Press distribution [Pa]	
	Row 4	94.132	88.549	97.258	81.015	55.702	77.799	103.328	65.251	93.906	86.845
100.0%	Row 1	112.722	94.493	48.165	92.271	79.546	75.920	45.553	107.289	Average Pressure [Pa]	
	Row 2	108.951	62.432	85.320	87.767	82.581	64.043	67.247	129.407	1358.973	1256.510
	Row 3	108.951	62.432	85.320	87.767	82.581	64.043	67.247	129.407	Press distribution [Pa]	
	Row 4	75.851	97.366	92.015	57.150	39.753	65.458	94.400	62.037	84.936	78.532

D.4 A-frame outlet pressure distribution 750 rpm

Appendix B The following tables uses the pressure and velocity calibration data of the anemometer distance test to give a distribution of pressure

Table D-25: Exit A-frame distribution of static pressure - typical readings (750 rpm)

		West/Left				East/Right					
		11	12	13	14	7	8	9	10	Right	Left
Units		[Pa]	[Pa]	[Pa]	[Pa]	[Pa]	[Pa]	[Pa]	[Pa]		
50.00%	Row 1	228.187	174.815	175.463	181.455	153.293	191.704	85.894	194.062	Average Pressure [Pa]	
	Row 2	168.935	111.798	223.312	179.486	235.495	145.662	102.812	197.830	2946.516	2683.766
	Row 3	203.367	97.995	215.525	145.192	177.838	106.236	170.191	205.039	Press distribution [Pa]	
	Row 4	241.046	208.074	210.216	181.650	173.238	168.385	177.309	198.777	184.157	167.735
66.70%	Row 1	164.174	111.204	113.454	150.785	126.652	125.343	45.653	138.497	Average Pressure [Pa]	
	Row 2	142.605	79.252	158.701	120.236	167.614	118.195	70.380	167.842	2164.274	1981.296
	Row 3	182.774	73.229	158.823	112.690	112.268	101.125	116.778	185.915	Press distribution [Pa]	
	Row 4	184.433	159.317	155.988	96.611	82.898	125.582	157.289	139.263	135.267	123.831
83.30%	Row 1	147.954	108.178	95.294	146.997	113.268	111.539	44.189	123.410	Average Pressure [Pa]	
	Row 2	138.260	76.054	149.277	139.652	155.586	107.236	75.550	170.315	2003.735	1794.801
	Row 3	163.626	64.719	134.527	130.143	145.836	83.711	90.827	154.240	Press distribution	
	Row 4	145.891	123.195	129.985	109.983	89.164	98.219	111.038	120.674	125.233	112.175
100.00%	Row 1	120.155	93.301	58.011	98.438	86.405	84.849	35.312	102.182	Average Pressure [Pa]	
	Row 2	103.245	57.333	91.561	99.443	99.696	63.747	54.925	121.500	1490.970	1311.461
	Row 3	127.660	53.607	94.402	101.633	99.826	61.667	68.330	124.061	Press distribution [Pa]	
	Row 4	102.381	105.096	101.911	82.794	68.553	65.429	95.877	79.102	93.186	81.966

D.1 MSACC B2-fan Performance Sample Calculations

The B2-axial flow fan performance curves were compiled from the test data results obtained in the MSACC. The static pressure in the bell mouth was measured as well as the inlet and exit air speed, torque, rotational speed and certain pressure points in the A-frame plenum. The atmospheric pressure and temperature was also measured at every test.

Setting up the B2-fan in MSACC, a specially designed jig and a levelling table was used to set the B2-fan root stagger angle to angle of 31° . The fan blade length was adjusted to produce a fan tip clearance of 4mm. The B2-fan was installed 450 mm from the entrance of the bell mouth, this was the maximum distance allowed by the fan bearing housing and electric motor stand.

All readings for the one test per throttle position related to the B2-fan in the MSACC are listed in the following table below:

Table D-26: Experimental readings for 660 rpm

Data Set No.	p_{fs}	T_f	V_1	V_2	V_3	V_4	V_5	V_6
units	[Pa]	[Nm]	[m/s]	[m/s]	[m/s]	[m/s]	[m/s]	[m/s]
100%	147.213	60.610	7.683	6.731	8.246	7.290	7.495	8.020
	147.212	60.338	7.672	6.773	8.307	7.232	7.456	7.977
	146.953	59.639	7.672	6.773	8.307	7.232	7.456	7.977
	146.398	60.150	7.709	6.802	8.166	7.212	7.384	7.983
91.7%	162.145	62.280	7.377	6.388	7.871	7.096	7.143	7.701
	161.927	62.423	7.414	6.491	7.849	7.013	7.145	7.724
	161.927	62.423	7.414	6.491	7.849	7.013	7.145	7.724
	161.787	62.369	7.384	6.628	7.827	6.843	7.079	7.707
83.3%	152.296	54.566	6.557	5.681	6.783	6.150	6.278	6.862
	154.027	53.568	6.525	5.587	6.825	6.168	6.224	6.804
	156.824	53.528	6.507	5.636	6.770	6.343	6.270	6.866
	157.835	53.458	6.503	5.641	6.747	6.265	6.245	6.802
75%	167.343	54.041	6.251	5.532	6.489	5.811	5.887	6.574
	166.992	54.326	6.183	5.409	6.452	5.969	5.919	6.481
	162.555	53.466	6.231	5.399	6.397	5.934	5.953	6.625
	166.540	53.811	6.224	5.450	6.359	5.789	5.855	6.493
66.7%	185.297	53.746	5.835	5.124	6.049	5.509	5.458	6.176
	183.104	53.727	5.769	4.949	6.130	5.673	5.559	6.171
	183.104	53.727	5.769	4.949	6.130	5.673	5.559	6.171
	182.008	53.126	5.797	5.081	6.045	5.594	5.612	6.199
58.3%	201.864	53.625	5.459	4.656	5.720	5.193	5.176	5.908
	201.859	53.347	5.189	4.680	5.654	5.405	4.994	5.769
	200.845	53.095	5.461	4.685	5.601	5.219	5.171	5.874
	201.124	53.091	5.465	4.586	5.648	5.183	5.098	5.902

50%	218.968	53.619	5.281	4.378	5.273	4.825	4.887	5.600
	220.844	52.952	4.916	4.360	5.219	4.820	4.674	5.412
	222.319	52.987	4.998	4.671	5.136	4.764	4.691	5.428
	221.840	53.145	5.007	4.461	5.208	4.783	4.639	5.607

Table D-27: Experimental readings for 750 rpm

Data Set No.	p_{fs}	T_f	V_1	V_2	V_3	V_4	V_5	V_6
units	[Pa]	[Nm]	[m/s]	[m/s]	[m/s]	[m/s]	[m/s]	[m/s]
100%	178.998	70.186	7.365	7.707	8.112	7.782	7.741	8.244
	181.141	72.957	7.483	7.577	8.136	7.933	7.425	8.360
	182.424	71.693	7.306	7.541	8.175	7.817	7.359	8.218
	181.111	70.650	7.546	7.574	8.156	7.718	7.412	8.235
83.3%	211.668	73.121	7.157	6.891	7.962	7.382	6.805	7.156
	211.080	73.340	6.997	7.398	8.329	7.644	6.799	7.729
	212.688	73.202	7.075	7.030	8.329	7.569	6.950	8.041
	210.641	73.275	6.969	7.219	7.582	7.546	6.749	7.895
66.7%	241.592	75.223	6.438	6.552	7.315	6.682	6.368	7.311
	241.593	72.564	6.184	6.355	6.907	6.630	6.356	7.175
	248.419	74.210	6.426	6.236	6.912	6.824	6.413	7.240
	247.293	74.929	6.275	6.910	7.190	6.764	6.417	7.183
50%	290.491	73.577	5.668	6.063	6.697	6.116	5.792	6.431
	290.858	73.267	5.757	6.112	6.759	6.046	5.634	6.361
	291.885	73.971	5.687	6.267	6.910	6.140	5.749	6.578
	290.110	73.211	5.749	6.362	6.899	6.119	5.801	6.629

Using the first data set presented in the tables above as the input values for the sample calculations, produced the following was the inlet volumetric flow rate, power consumption of the fan and the static efficiency results:

Table D-28: Normalised 660 rpm B2-fan results

Data Set No.	\dot{V}_f	p_{fs}	P_f	η_{fs}
units	[m ³ /s]	[Pa]	[W]	[%]
100%	13.222	143.482	3312.506	57.274
	13.209	143.708	3342.001	56.798
	13.186	143.708	3342.001	56.702
	13.140	143.707	3322.282	56.837
91.7%	12.636	162.145	3416.101	58.198
	12.653	161.927	3426.617	58.021
	12.632	161.927	3426.617	57.924
	12.583	161.788	3422.611	57.719
83.3%	11.137	152.498	3474.011	48.887
	11.175	154.083	3400.751	50.633
	11.133	156.966	3414.145	51.183
	11.010	158.510	3417.939	51.060

75%	10.763	167.343	3200.487	55.793
	10.784	166.992	3241.713	55.077
	10.858	162.555	3097.305	56.305
	10.742	166.540	3141.518	56.270
66.7%	9.933	176.090	3675.524	47.586
	9.961	174.006	3674.156	47.176
	9.944	173.420	3674.156	46.938
	9.967	172.382	3630.546	47.323
58.3%	9.339	201.864	3435.425	54.877
	9.217	201.859	3415.282	54.478
	9.294	200.845	3396.937	54.953
	9.256	201.124	3396.656	54.809
50%	8.666	224.351	3399.986	57.181
	8.609	226.334	3380.195	57.647
	8.650	225.979	3368.239	58.034
	8.651	226.927	3404.558	57.663

Table D-29: Normalised 750 rpm B2-fan results

Data Set No.	\dot{V}_f	p_{fs}	P_f	η_{fs}
units	[m ³ /s]	[Pa]	[W]	[%]
100%	14.440	187.397	4896.736	55.262
	14.428	189.640	5095.314	53.699
	14.248	190.984	5004.681	54.372
	14.319	189.609	4929.958	55.070
83.3%	13.310	221.600	5137.015	57.415
	13.794	220.984	5152.733	59.160
	13.802	222.668	5142.828	59.760
	13.477	220.525	5148.073	57.732
66.7%	12.081	237.578	5226.755	54.913
	11.759	237.642	5007.69	55.802
	11.874	246.097	5056.361	57.791
	12.083	244.851	5120.225	57.780
50%	10.894	285.664	5363.057	57.834
	10.864	286.100	5334.732	58.099
	10.917	289.156	5307.165	60.171
	10.908	287.246	5252.568	60.574